University of Puerto-Rico

Doctoral Thesis in Chemical Physics

Multifunctional oxide materials for memory applications

Sita Dugu

A thesis submitted in partial fulfillment of the requirement of the degree of doctor of philosophy in chemical physics

Supervised by
Prof. Ram S. Katiyar
Department of Physics
University of Puerto Rico
San Juan, Puerto Rico, USA
07/19/2021

UNIVERSITY OF PUERTO-RICO, RIO-PIEDRAS

We hereby recommend that the research work presented by **Sita Dugu** in this thesis entitled **"Multifunctional oxide materials for memory applications"** has been accepted for partial fulfillment of the requirements for the degree of **Doctor of Philosophy in Chemical Physics**.

Prof. Dr. Ram S. Katiyar
Thesis advisor
Department of Physics

Prof. Gerardo Morell
Thesis committee member
Department of Physics

Prof. Brad Weigner
Thesis committee member
Department of Chemistry

Dedicated to my dear parents

Abstract

Non-volatile memory technology in Si-based electronics dates back to 1990s. It is radically new storage technology that combines the performance and byte addressability of DRAM with the persistence of traditional storage devices like SSD. Emerging memory technologies promise new memories to store more data at less cost than the expensive-to-build silicon chips used by popular consumer gadgets. Emerging non-volatile memory technologies such as magnetic random-access memory (MRAM), spin-transfer torque random-access memory (STT-RAM), ferroelectric random-access memory (FeRAM), phase-change memory (PCM), and resistive random-access memory (RRAM) combine the speed of static random-access memory (SRAM), the density of dynamic random-access memory (DRAM), and the nonvolatility of Flash memory and so become very attractive as another possibility for future memory hierarchies.

Multiferroics (MF) magnetoelectric (ME), generally a combining properties of MRAM and FeRAM are another exciting NVM which are

getting intensive scientific attraction recently. Most existing MF-ME have some drawbacks; (i) They have either very low or too high transition temperature, (ii) They possess very low FE and/or FM responses and (iii) have low ME coupling coefficient, that hinder the practical applications. MF-ME materials with ferroelectric and magnetic transition temperatures near room temperature are of current interest of research due to their technological importance and potential applications.

This work provides the detail study of single phase compounds gallium ferrite (GFO) along with some dopants at its various compositions. Polycrystalline samples with modifying Fe and Mn contents on GFO, $Ga_{2-x}(Fe_{1-y}Mn_y)_xO_3$, $0 \leq y \leq 0.02$ and $1 \leq x \leq 1.4$ were prepared by solid state reaction method, stabilizes in orthorhombic phase (space group C_{2v}^9). Temperature dependent magnetization behavior studied in a wide temperature range of 5 - 395 K at both field-cooled (FC) and zero-field-cooled (ZFC) conditions using different static magnetic fields shows the lower magnetic transition temperature (T_C) for pure $GaFeO_3$ (GFO), i.e., 220 K, which increases to 345 K above room temperature (RT)) for 2% Mn-doped $Ga_{0.6}Fe_{1.4}O_3$ (GFMO3). Higher remanant magnetization ($\sim$ 16 emu/g) with a lower coercive field ($\sim$ 4 kOe) is obtained for Mn-doped $Ga_{0.6}Fe_{1.4}O_3$. Evidence of spin-glass like magnetic ordering is observed at low temperature. Temperature dependent

Raman spectroscopic studies on pure GFO down to 82 K showed 31 Raman active modes in the spectral range 90 – 900 cm^{-1}. Some of the phonon mode frequencies exhibit anomalies close to T_C. At elevated temperatures no significant changes in Raman spectra were observed that can be attributed to the absence of any structural phase transition. Instead of expected anharmonic behavior, several librational and stretching modes of rigid BO6 units were found to be hardening below T_C, in the low temperature ferrimagnetic phase, suggesting the significant magnetoelastic coupling contributions to phonon frequencies. Magnetic excitation induced phonon renormalization is evident in the low temperature magnetic phase. The asymmetric stretching mode at 753 cm^{-1} is found to have larger spin-phonon coupling contribution ($\lambda \sim 2.93$) while the lattice mode at 153 cm^{-1} and external librational mode at 240 cm^{-1} had the lowest effect ($\lambda \sim 0.88$). On Mn-doping, we observed exciting results with reduced leakage current. Current density has been reduced on doping Mn. The observation of multiferroicity in these single-phase materials at RT make them potential candidates for memory, multifunctional, and spintronics device applications.

Highly oriented thin films of $Ga_{2-x}(Fe_{1-y}Mn_y)_xO_3$, $0 \leq y \leq 0.02$ and $1 \leq x \leq 1.4$ were prepared by pulse laser deposition method on $SrRuO_3$ (SRO) buffered $SrTiO_3$ (111) substrates. The magnetic tran-

sition temperature (T_C) of thin films were found to be higher than corresponding ceramics. Ferroelectric properties were studied by PFM and P-E loops. Remnant polarization (P_r) of $\sim$ 35 $\mu C/cm^2$ on pure GFO were observed which decreased on Mn and Fe substitution. The clear and reversible out-of-plane phase-contrast seen in the Piezoresponse Force Microscopy (PFM) phase and amplitude images measured within positive and negative poling confirms the polarization reorientation and hence piezoelectric nature of the compound. The temperature and frequency dependence of permittivity studies demonstrate the relaxor behavior of these thin films. The observed near room temperature (RT) magnetic phase transition with RT piezoelectric nature of these thin films elucidates the possible potential candidates for a multiferroic world with spintronics device applications. To study the optical properties of the compound, thin films were deposited on fused silica. Both direct bandgap and indirect bandgap were present and reduction in band-gap with increase in Fe concentration were observed. These observations of reduction in E_g with Fe addition and also observation of indirect band gap shows the potential application of the material in optical devices.

We demonstrate the hybrid fabrication process of a graphene integrated highly transparent resistive random access memory (TRRAM)

device. The indium tin oxide (ITO)/Al_2O_3/graphene nonvolatile memory device possesses a high transmittance of > 82 % in the visible region (370 - 700 nm) and exhibits stable and non-symmetrical bipolar switching characteristics with considerably low set and reset voltages ($\pm$ 1 V). The vertical two-terminal device shows an excellent resistive switching behavior with a high on-off ratio of $\sim 5 \times 10^3$. We also fabricated ITO/Al_2O_3/Pt device and studied its switching characteristics for comparison and a better understanding of the ITO/Al_2O_3/graphene device characteristics. The conduction mechanisms in high and low resistance states were analyzed and the observed polarity dependent resistive switching is explained based on electro-migration of oxygen ions.

Acknowledgement

It is a genuine pleasure to express my deep sense of gratitude to my supervisor Prof. Ram S. Katiyar, for providing me the opportunity to carry out research in his group. His excellent guidance, scholarly advice, unparallel inspiration and constant support throughout the investigation made a journey fruitful and successful on completing this work.

I am extremely grateful to my thesis committee members Prof. Gerardo Morell and Prof. Brad Weigner for their valuable time to review my thesis and providing valuable comments, suggestions and advice.

I owe a deep sense of gratitude to Dr. Shojan P. Pavvunny for his invaluable guidance, discussion and experimental approaches on my investigation.

I would like to express my heartfelt gratitude and regards to Prof. James F. Scott for his guidance, fruitful discussions and motivation to accomplish this task.

It is my pleasure to acknowledge US Department of Defense (DOD),

Department of graduate Student and Investigation (DEGI) for providing me doctoral fellowship and financial support during this work. I would like to thank Prof. Jose Nieves and Ileana Desiderio and all administrative staff of Physics Department for their assistance and support. I also want to thank the staff of Material Characterization Center (MCC) at UPRRP for allowing me to use their facilities to carry out part of my research.

I express my special thanks to Mr. William Perez for providing technical help, valuable advice and information during my research period.

I would like to thank all the past and present members of our SPECLAB group for their kind cooperation and friendship. My deep regards goes to Anand Gaur, Adriana Rivera, Dhiren K. Pradhan, Shalini Kumari, Danilo, Alvaro Instan, Mohan K Bhattarai, Yamile Rosas, Claudia Zuluaga, Nischal Oli and Monica Lopez, for their help and support in investigation as well as sharing friendly moments during stay at SPECLAB.

I am thankful to Ashok Sharma, Satya Prakahs Sahoo, Nora Patricia, Jamie Scott, Ricardo Martinez, Dilsom Sanchez, Loraine Torres, Jifi Shojan, Yogesh Sharma, Radhe Aggrawal, Nitu Kumar, Geetika Khurana, Rajesh Katiyar, Karunakara Mishra and Ivan Castillo.

I am grateful to Mrs Sudha Katiyar (Aunty) for her love, affection

and personal care during this time.

My deepest gratitude to my parents whose unconditional love has been my greatest strength and devotion. I am heartily thankful to my family members, who have contributed a lot to shape me, who I am today. I express my special thanks to my dear daughter Rita Matina, who have been my source of motivation and inspiration since after the birth. I am very proud to have her and present this document to her today.

Abbreviations and Symbols

DRAM	=	Dynamic Random Access Memory
SSD	=	Solid State Drive
NVM	=	Non volatile memory
MRAM	=	Magnetic Random Access Memory
RRAM	=	Resistive Random Access Memory
MF	=	Multiferroic
T_c	=	Transition Temperature
T_m	=	Maximun Temperature
C	=	Curie temperature
ME	=	Magnetoelectric
GFO	=	Gallium Ferrite
SRO	=	Strontium Ruthenite
STO	=	Strontium Titanate
RT	=	Room Temperature
FC	=	Field Cooled
ZFC	=	Zero field Cooled
M-H	=	Magnetization versus Field
M-T	=	Magnetization versus Temperature
M_R	=	Remnant Magnetization
H_C	=	Applied Magnetic Field
P_r	=	Remnant Polarization
ϵ_r	=	Permittivity
ϵ_m	=	Maximum permittivity
α	=	absorbtion coefficient
TRRAM	=	Transparent Resistive Random Access Memory
HRS	=	High Resistance State
LRS	=	Low Resistance State

Lists of Publications

1. Observation of Relaxor-Ferroelectric Behavior in Gallium Ferrite Thin Films, **S. Dugu**, M. K. Bhattarai, S. Kumari, A. Instan, D. K. Pradhan, M. Holcomb, J. F. Scott, and R. S. Katiyar, Appl. Sur. Science, 523, 146-459, (2020)

2. Tuning the magnetic phase transition above toom temperature in gallium ferrite with reduced leakae current, **S. Dugu**, S. Kumari, D. K. Pradhan, C. Zuluaga, M. Holcomb, and R. S. Katiyar, *J. Phys. D: Appl. Phys*, 53, 225001, (2020).

3. Room temperature multiferroicity and magnetodielectric coupling in 0–3 composite thin films, D. K. Pradhan, S. Kumari, R. K. Vasudevan, **S. Dugu**, P. T. Das, V. S. Puli, D. K. Pradhan, S. V. Kalinin,R. S. Katiyar, P. D. Rack, A, Kumar, *J. Appl. Physics*, 127, 194104, 2020

4. Ferroelectric ordering and energy storage density of thin film capacitor by doping La^{3+} and Sc^{3+} on Pb(Zr0.53Ti0.47)O3 using pulse laser deposition technique, M. K Bhattarai, K. K. Mishra, **S. Dugu**, A. Instan, and R. S. Katiyar. *Appl. Phys. Lett*, 114, 223902, (2019).

5. Coupled phonons and magnetic orderings in GaFeO3: Raman and magnetization studies, **S. Dugu**, K. K. Mishra, D. K. Pradhan, S. Kumari, and R.S. Katiyar, *J. Applied Physics*, 125, 064101 (2019)

6. A graphene integrated highly transparent resistive switching memory device, **S. Dugu**, S. P. Pavunny, T. B. Limbu, B. Weigner, G. Morell, R. S. Katiyar, *APL Material*, 6, 058503 (2018)

7. Si:SrTiO3-Al2O3-Si:SrTiO3 multi-dielectric architecture for metal-insulator-metal capacitor applications, **S. Dugu**, S. P. Pavunny, J. F. Scott, and R. S. Katiyar, *Appl. Phys. Lett*, 109, 212901, (2016).

8. Disorder driven structural and dielectric properties of silicon-substituted strontium titanate, **S. Dugu**, S. P. Pavunny, Y.Sharma, J. F. Scott, and R. S. Katiyar, *J. Applied Physics*, 118, 034105, (2015).

9. Holmium Hafnate: An emerging electronic device material, S. P. Pavunny, Y. Sharma, S. Kooriyattil, **S. Dugu**, R. K. Katiyar, J. Scott and R. S. Katiyar, *Appl. Phys. Letter*, 106, 11, (2015).

Presentation

Oral Presentation

1. Magnetic Behavior of Near Room temperature Multiferroic Gallium Ferrite And its Application. **S. Dugu**, K. K. Mishra, D. K. Pradhan, S. Kumari, M. K. Bhattarai, and R. S. Katiyar. Materials Challenges in Alternative and Renewable Energy (MCARE) 2018, Vancouver, BC, Canada, Aug 20-23, 2018.

2. Near Room Temperature Multiferroic Gallium Ferrite. **S. Dugu**, D. K. Pradhan, K. K. Mishra, Shalini Kumari, and R. S. Katiyar, 2018, MRS Spring Meeting and Exhibit, Apr 2-6, Phoenix, Arizona, 2018.

3. Phonon and Magento-electric ordering in Gallium Ferrite Multiferroic. **S. Dugu**, K. K. Mishra, D. K. Pradhan, S. Kumari, and R. S. Katiyar, APS March Meeting 2018 Los Angeles, California March 5-9, 2018

4. Graphene/Al2O3/ITO Transparent Resistive Memory Structures. **S. Dugu**, S. P. Pavuunny, T. B. Limbu, and R. S. Katiyar, 2016 MRS Fall Meeting Exhibit, Nov 28-Dec1, Boston, Massachusetts, 2016.

Poster Presentation

5. Lead Free Multiferroic Nano-heterostructure Film for Energy Storage Application,M. K. Bhattarai, **S. Dugu**, A. Instan, and R. S. Katiyar, 2019 MRS Fall Meeting Exhibit, Dec 1-6, 2019, Boston, Massachusetts, 2019

6. Nobel Lead Free Relaxor Multiferroic for High Energy Storage Application, M. K. Bhattarai, **S. Dugu**, A. Instan, and R. S. Katiyar, 2018 MRS Fall Meeting Exhibit, Nov 25-Nov 30, 2018, Boston, Massachusetts, 2018.

7. Dielectric and Ferroelectric Behaviors of Modified PZT Thin Films Synthesized by Pulse Laser Deposition Method, M. K. Bhattarai, A. Instan, **S. Dugu**, P. Kumar, and R. S. Katiyar, 2018 MRS Fall Meeting Exhibit, Nov 25-Nov 30, 2018, Boston, Massachusetts, 2018.

8. Studies on Magnetic and Electric Properties of Gallium Ferrite Multiferroic Thin Film. **S. Dugu**, D. K. Pradhan, S. Kumari, M. K. Bhattarai, A. I. Ballesteros, and R. S. Katiyar. 2018 MRS Fall Meeting Exhibit, Nov 25-Nov 30, 2018, Boston, Massachusetts, 2018.

9. Dielectric and Ferroelectric Behaviors of PZT Thin Films Modified by Rare Earth Metals (La3+, Sc3+) for Ferroelectric Memory Applications. M. K. Bhattarai, K. K. Mishra, A. I. Ballesteros, **S. Dugu**, and R. S. Katiyar, MRS Spring Meeting Exhibit, Apr 2-6, Phoenix, Arizona, 2018.

10. Novel Engineered Ferroelectric Thin Films for Energy Storage Applications. **S. Dugu**, A. I. Ballesteros, D. K. Pradhan, M. K. Bhattarai, and R. S. Katiyar, 2017 MRS Fall Meeting Exhibit, Nov 26-Dec1, 2017, Boston, Massachusetts, 2017.

11. Resistive Memory Structures of Nano-Layered Al2O3, **S. Dugu**, S. P. Pavunny, and R. S. Katiyar, 2017 MRS Spring Meeting Exhibit, Apr 17-21, Phoenix, Arizona, 2017.

12. Effect of Al2O3 Monolayer Inclusion in Symmetric Nanoscale Metal-Insulator-Metal. **S. Dugu**, S. P. Pavuunny, and R. S. Katiyar.

Puerto-Rico EPSCoR Annual Meeting 2016. Caguas, PR, April 22, 2016.

13. Silicon Substituted Strontium Titanate: A Promising High-k Dielectric Material. S. Dugu, S. P. Pavunny, Y. Sharma, and R. S. Katiyar, 2016 MRS Spring Meeting Exhibit, March 28-April 1, Phoenix, Arizona, 2016

14. Effect of Al2O3 Monolayer Inclusion in Symmetric Nanoscale Metal-Insulator-Metal Capacitors. **S. Dugu**, S. P. Pavuuny, and R. S. Katiyar, 2016 MRS Spring Meeting Exhibit, March 28-April 1, Phoenix, Arizona, 2016.

15. Silicon Modified Strontium Titanate for logic and memory device. **S. Dugu**, S. P. Pavuuny, Y. Sharma, and R. S. Katiyar, Workshop on Multifunctional Nanomaterials, San Juan, PR, 14-16 Jan 2015

16. Structural and Dielectric Properties of Silicon Modified Strontium Titanate. **S. Dugu**, S. P. Pavuuny, Y. Sharma and R. S. Katiyar, 35th Puerto-Rico Interdisciplinary Scientific Meeting, University of Puerto Rico, Rio-Piedras Campus. March 14, 2015.

Contents

List of Tables

List of Figures

Chapter 1

Introduction

1.1 Preamble

Semiconductor memory has always been an indispensable part of an electronic systems and also represents a significant portion of semiconductor market [1, 2]. The digital universe is undergoing relentless expansion that the number of bits generated annually is expected to reach zettabytes (i.e. 44 trillion gigabytes) in near future [3]. With these rapid developments of big data infrastructures and the Internet of Things (IoT) in recent years, the demand for bigger, faster, cheaper and more reliable non volatile memory (NVM) is ever-increasing [2]. NVM is a radically new and highly promising semiconductor technology which doesn't require a continuous power supply to retain the data. The possibility of nonvolatile memory device was first suggested by

Kahng D and Sze SM in 1967 for the first time using a floating gate device [4].

The global information era has been seeking a universal non-volatile random-access memory (NVRAM) for many years. The best-known form of NVRAM today is flash memory. The relentless scaling of NAND flash is so far being able to meet the demand of memory, even exceeding the pace of Moore's law for transistors. However, there are a few drawbacks of Flash such as low endurance, low write speed, and high voltages requirement for the program/erase operations. Difficulty to shrink tunneling-oxide and interpoly dielectric (IPD) thickness due to reliability issues is another serious downside [5]. Further scaling, i.e., a continuation in increasing the density of Flash is expected to run into physical limits in the near future [6]. Even though the 3D cross-bar structure may solve the low-density issue of Flash temporarily [7], the market demands next generation NVM that has overall advantages over Flash. Several competitive technologies are attempting to replace flash memory in certain roles. These include magnetic random access memory (MRAM) [8, 9, 10], resistive switching random access memory (RRAM) [11, 12],phase change memory (PRAM) [13, 14], ferroelectric random access memory (FeRAM) [15, 16, 17], and racetrack memory

[18]. Multiferroics that combine magnetism and ferroelectricity as well as mutual coupling between them [19, 20, 21, 22], is another NVMs that hold a promise for designing a new generation of memory devices. This thesis presents the study of two branches in NVMs (i) Multiferroics and (ii) RRAM.

1.2 Basics of Ferroics and Crystallography

The development and progress in the field of material science has being possible because of novel preparation techniques and their characteristic investigation technique by means of sophisticated instruments. Various advances in the field of material science depends on the availability of materials either in the form of bulk ceramics or in the form of single crystal, thin films or nanoparticles. Materials possess symmetry, and when environmental conditions are changed, they sometimes undergo a change of symmetry spontaneously. This spontaneous breaking of directional and other types of symmetry is widely prevalent in Nature, such as in water (ice-water-vapor) to even at the birth of the universe (at the moment of big bang) [23]. In the science of crystals, change in symmetry is the process of transfer from one phase to another. Ferroic crystals are those crystals which involve at least one phase transition that changes the directional symmetry of the crystal e.g. the sym-

metry of the cubic phase of the paraelectric $BaTiO_3$ is the prototype symmetry for its tetragonal ferroelectric ferroelastic phase occurring at room temperature. Ferroic crystals contain two or more equally stable domains in different spatial orientations. Under suitable driving force, these domain walls can be moved and the crystals switched from one orientation state to another [24]. The crystal domain distinguished by spontaneous polarization, magnetization, strain and toroidal moments are called as ferroelectric, ferromagnetic, ferroelastic and ferrotorroidal crystals [25, 26]. These four ferroics are called as Primary ferroics. In secondary ferroics, domains in the crystals are characterized by differences in the dielectric permittivity tensor or piezoelectric tensor. In primary ferroics, switching is accomplished by elelctric field whereas in secondary, it is done by a combination of an elelctric field and mechanical stress [27, 28]. Ferroic materials exhibit a hysteresis loop. These ferroics possess a large varieties of applications such as memory devices, sensors, transducers, servo motors, mechanical shifters, servo mechanisms, generators, transformers, amplifiers, acousto optic modulators, phase shifters, frequency multipliers, displays and wave filters.

According to crystallographic symmetry, crystals can be classified into 32 point groups. Out of these 32-point groups, 11-point groups possess a center of inversion and are called centrosymmetric, and 21-point

groups are with non-centrosymmetric. These 32 point groups are subdivisions of 7 basic crystal systems: tricilinic, monoclinic, orthorhombic, tetragonal, rhombohedral, hexagonal, and cubic as shown in table 1.1. Ferroelectric crystal comes under non-cetrosymmetric point groups as a subclass of piezoelectric and pyroelectric materials. Of the 32 crystallographic point groups,(in table 1.1 those highlighted in magenta possess a centre of inversion and are called centrosymmetric, while those highlighted in red possess only rotation axes and are termed enantiomorphic. A third type, highlighted in bold type, are referred to as polar.

Crystal System	32 Crystallographic Point Groups						
Triclinic	1	-1					
Monoclinic	**2**	**m**	2/m				
Orthorhombic	222	**mm2**	**2**				
Tetragonal	4	-4	4/m	422	**4mm**	-42m	4/mmm
Trigonal	**3**	-3	32	**3m**	-3m		
Hexagonal	**6**	-6	6/m	622	**6mm**	-62m	6/mmm
Cubic	23	m-3	432	-43m	m-3m		

Table 1.1: Crystallographic point groups

1.3 Ferroelectric materials

Ferroelectric materials are the dielectric materials in which polarization remains permanent even after the applied electric field is removed and the direction of dipole moment can be switched by applying electric

field [29]. The spontaneous polarization in ferroelectric materials varies with external electric field, resulting a hysteresis loop with polarization versus electric field curve as shown in figure 1.1. All ferroelectric materials are pyroelectric, which means they are also inherently piezoelectric as well. Thus, it is possible to change the magnitude or the direction of the spontaneous polarization as a function of temperature, pressure, or applied electric fields [30].

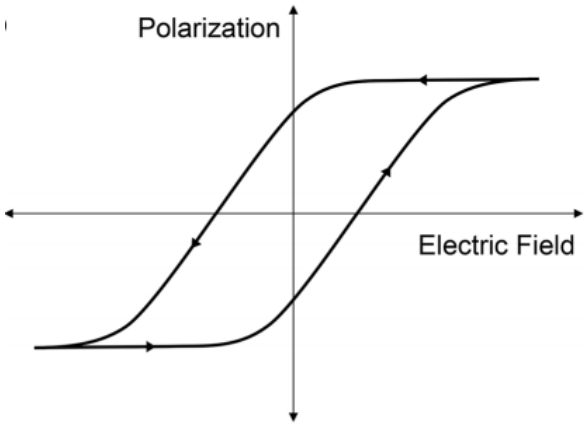

Figure 1.1: P-E hysteresis loop of ferroelectric material

Valsek in 1921 discovered ferroelectric material for the first time, while investigating dielectric properties of Rochelle salt ($NaKC_4H_4O_6.4H_2O$) [31]. However, this topic gained much attention only in 1944, when Von Hippel discovered ferroelectric in Barium Titanate ($BaTiO_3$) [32]. Since then many ferroelectric were developed on 1950-1960 such as $Cd_2Nb_2O_7$, $Sn(NH_2)_2$, $NaNo_2$ family etc. Lead Titanate is another evolutionary success of that era that possess high Curie temperature

and was proved to be exceptionally suitable for the formation of piezoelectric composition. Ferroelectricity of a given material ceases above a characteristic temperature called its Curie temperature. It is because of the heat that agitates the dipoles enough to overcome the force which helped them to align.

A crystal changes its symmetry during phase transition (a process of going from one phase to another). Two common types of phase transitions are first order and second order phase transitions. A first order transition is one which has a discontinuity in the order parameter itself, while in second phase transition, there is discontinuity in the first derivative of the order parameter.

In a perfect ferroelectric crystal, the phase transition takes place at Tc, which is called the Curie temperature. Hysteresis loop with the coordinates of voltage vs polarization determines the spontaneous polarization. The hysteresis loop observation is often complicated by effect of the traps [33]. In this case, study of temperature dependent dielectric constant is preferred to observe ferroelectric phase transition and the maximum of dielectric curve ε(T) at T= Tm is quantified as the point of the phase transition called as Curie temperature. A linear dependency can well be fitted with Curie-Wiess law, written as ε = C/(T-Tc), where C is curie constant and Tc is curie temperature,

which is equal to Tm in this case. In some ferroelectric, T doesn't follow the linear behavior as predicted by Curie-Weiss law. A broad maxima is seen at Tm and deviate from typical ferroelectric, called as a diffuse phase transition (DPT) or relaxor. In this case, this deviation from Curie-Weiss behavior is fitted by empirical power law given by

$$\frac{1}{\epsilon(\omega,T)} = (\frac{1}{\epsilon_{max}(\omega,T)})(1+\frac{(T-T_{max})^{\gamma}}{2\delta^2}) \tag{1.1}$$

where γ and δ are parameters describing the degree of relaxation and diffuseness of the transition respectively. The parameter γ varies between 1 and 2, where values closer to 1 indicate normal ferroelectric behavior whereas values close to 2 indicate good relaxor behavior [34, 35].

1.4 Ferromagnetic Material

The substances which becomes spontaneously magnetized are generally divided into three classes: ferromagnetic, antiferromagnetic and ferrimagnetic. Ferromagnetic materials exhibit strong magnetism in the direction of the applied magnetic field. Ferromagnetic material possesses several tiny regions referred to as domains in which the ionic or atomic magnetic moments are aligned parallel to one another. Weiss postu-

lated the presence of magnetic domains within the material. Domains are regions where the atomic magnetic moments are aligned. Ferromagnetic materials exhibit parallel alignment of moments, as shown in figure 1.2(a) resulting in large net magnetization even in the absence of a magnetic field. The movement of domains determines how the material responds to a magnetic field and as a consequence, the susceptible is a function of applied magnetic field. Therefore, ferromagnetic materials are usually compared in terms of saturation magnetization (magnetization when all domains are aligned) rather than susceptibility.

In ferromagnetic material, susceptibility becomes infinite at Curie temperature Tc, as shown in figure 1.2(b). Below this temperature, interactions overcome thermal agitation, and a spontaneous magnetization (Ms) appears in the absence of an applied magnetic field.

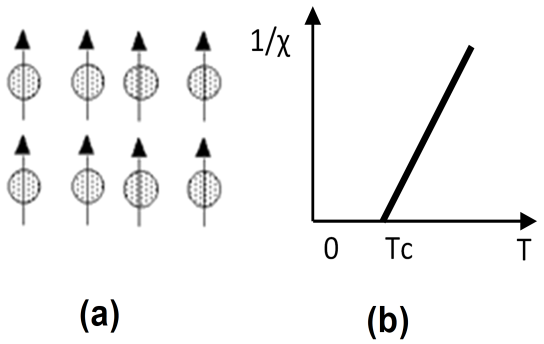

Figure 1.2: (a) Ferromagnetic spin and (b) Susceptibility versus temperature graph for ferromagnetic material

Above the critical temperature Tc, ferromagnetic compounds become paramagnetic and obey the Curie-Weiss law: $\xi = \frac{C}{T - T_C}$. In addition to the Curie temperature and saturation magnetization, ferromagnets can retain a memory of an applied field once it is removed. This behavior is called hysteresis and a plot of the variation of magnetization with magnetic field is called a hysteresis loop as shown in figure 1.3.

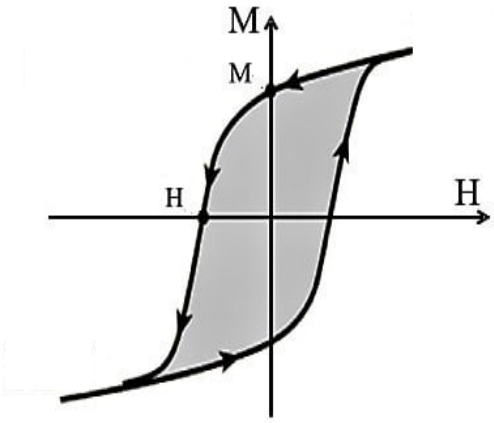

Figure 1.3: Ferromagnetic hysteresis loop

Antiferromagnetic materials are very similar to ferromagnetic materials but the exchange interaction between neighboring atoms leads to the anti-parallel alignment of the atomic magnetic moments. Like ferromagnetic materials these materials become paramagnetic above a transition temperature, known as the Neel temperature, T_N. In antiferromagnetic, the susceptibility obeys the Curie-Weiss law above T_N (paramagnets) but with negative intercept indicating negative exchange

ineractions. The spin orientation and the relation between susceptibility and temperature is shown in figure 1.4(a) and (b) respectively.

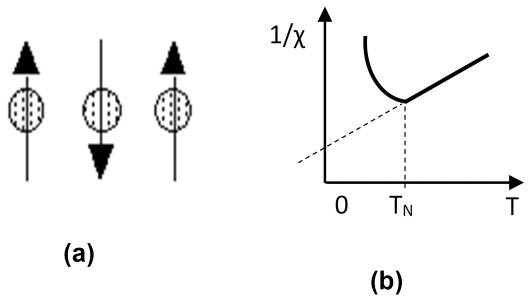

Figure 1.4: (a) Antiferromagnetic spin and (b) Susceptibility versus temperature graph for antiferromagnetic material

In 1948, Neel proposed a third type of magnetic phenomenon, called ferrimagnetism, with a special case of Mn_2Sb. Ferrimagnetic exhibits spontaneous magnetization below a certain temperature arising from a non-parallel alignment of atomic magnetic moments, where the two moments are not the same [36]. Another property of ferrimagnetic is the hyperbolic nature of $1/\chi$ vs T curve above Tc shown in figure 1.5.

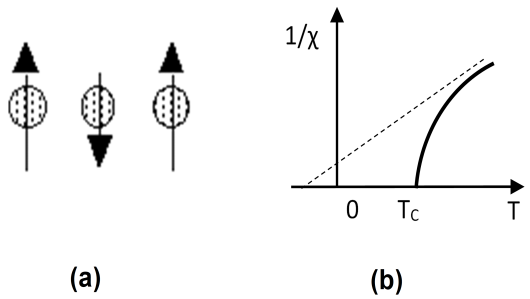

Figure 1.5: (a) Ferrimagneticspin and (b) Susceptibility versus temperature graph for ferrimagnetic material

1.5 Multiferroics

Multiferroics refers to those materials where more than one ferroic order, i.e. (anti) ferromagnetism, ferroelectricity, ferroelasticity and ferrotoroidicity, coexit in one phase [37, 19, 38]. Magnetic order is conventionally driven by exchange interactions between magnetic dipoles, originating from unfilled shells of electron orbitals. Electric order is the result of ordering of local electric dipoles. Elastic order is the result of ordering of atomic displacements due to strain [39]. A combination of these multiple ferroic orders may allow intimate coupling among them, paving the way to realize cross-control of various ordered parameters. The two fundamental concept of physics; magnetism and electricity are unified under the framework of electromagnetism via four Maxwell equations, although, magnetic moment and electric dipole are usually mutually exclusive in crystal. The discovery of multiferroicity breaks the principle of exclusion between magnetic moment and electric dipole [40]. FEs must have their space inversion symmetry broken, requiring that only crystal structures with noncentrosymmetric space groups can exhibit ferroelectricity. Often the ferroelectricity develops from a high-temperature symmetric phase via a structural phase transition in-

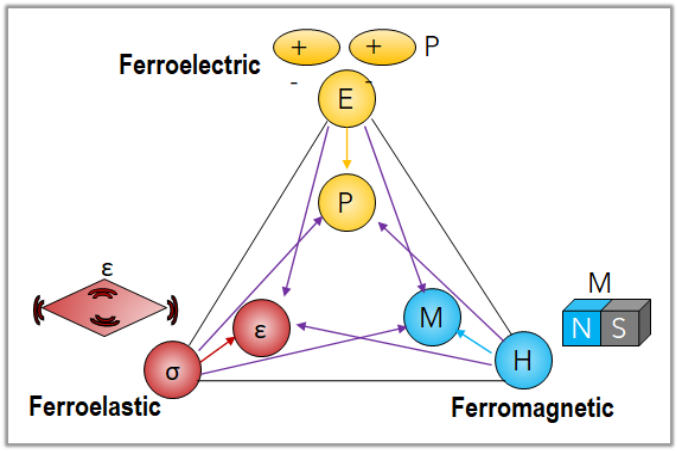

Figure 1.6: Schematics showing relationship between ferroics [42]

.

volving a soft phonon, and neutron scattering has played a pivotal role in illuminating the relation between the soft phonon, structural phase transition, and FE order. For magnetic materials, on the other hand, it is time reversal symmetry that has to be broken to allow the ionic magnetic moments to align. Hence, both symmetries must be violated for a material to be a candidate of MF, making them a rather rare but important commodity [41].

In the classical defination, multiferroic was defined in narrow sense as a material exhibiting both ferromagnetism and ferroelectricity. Nowadays, however, the term is used in a much broader context such as a material with one antiferroic-order plus another ferroic-order. Figure 1.6 illustrate the substantial expanded territories of multiferroics. Multiferroics have attracted enormous attention in the past decade, due to their fascinating physics and applicable magnetoelectric functionali-

ties including energy transformation, signal generation and processing, information storage, and so on. These materials could produce new technologies in which the low power and high speed of field-effect electronics are combined with voltage-controlled ferromagnetism [20, 43]. Such ideal multiferroic materials still remain rare because of the mutual exclusive nature of ferroelectricity of ferromagnetism under normal circumstances.

Two of most intensly investigated present-day multiferroics are $BiFeO_3$ and hexagonal (h-) manganites ($RMnO_3$, R = Sc, Y, In, Dy-Lu) have already been identified in the early 1960s. BFO has become one of the most popular and well-studied materials in the multiferroic research field at RT. It is because not only it simultaneously display ferroelectricity and antiferromagnetism at RT, but it also demonstrates intrinsic ME coupling. However, its large leakage and weak coupling hinders its application in devices. This urges to the search for promising RT, single phase multiferroic material.

Multiferroics are distinguished in two main classes.

1.5.1 Type I multiferroics:

The materials in which the ferroic orders arise independent of each other. The coupling between magnetism and ferroelectricity in these

materials is usually weak. Type I multiferroics is further divided into many subgroups. Out of them, few are mentioned below.

ABO_3 perovskite:

In this structure class BO6 octahedral share corners and the A-ion is coordinated by eight octahedral. The ferroelectric moment can be derived from a lone pair ion on A-site and in part from a small transition-metal ion, with d0 electron configuration, on the B-site. Magnetism can be generated by a transition-metal ion on the B-site with a partially filled d-electron shell, such as Mn3p or Fe3p, or by a rare-earth ion on the A-site. A judicious choice of composition can lead to multiferroicity in compounds such as $BiFeO_3$ [44], $Pb(Fe_{2/3}W_{1/3})O_3$ [45] and various other combinations. A well known material $BiFeO_3$ counts under this group in which the ferroelectric order originates from the lone electron pair of Bi^{3+}, while magnetic ordering is due to the unpaired Fe spins. The antiferromagnetic ordering is complicated by canting of the spins and the formation of a long-range spin cycloid that is incommensurate with the lattice [44]. $EuTiO_3$ is another example in which Eu^{2+} contains localized 4f spins which order antiferromagnetically at 5.5 K. Below this temperature the dielectric constant strongly decreases, resulting in large coupling effects which are explained by the coupling of

the spins to the optical phonon modes involved in the incipient ferroelectric transition [46].

Geometric ferroelectricity

Hexagonal manganites ($AMnO_3$) and hexagonal ferrites ($RMnO_3$; R=Y, Dy-Lu) are geometric ferroelectrics. In $AMnO_3$, magnetic ordering is derived from the electronic d4 configuration of Mn^{3+} on the B-site, or from a magnetic rare-earth ion on the A-site and the ferroelectric moment is largely derived from shifts of the A^{3+} in its coordinate here. On the other hand, in case of $YMnO_3$ [47][48], ferroelectricity is caused by the tilting of the practically rigid MnO_5 block. This tilting occurs just to provide closer packing, and as a result the oxygen ions move closer to the rather small Y ions.

Ferroelectricity due to charge ordering

This type is often observed in transition metal compound, especially containing transition metal ions with different valence such as in $Pr_{1/2}$-$Ca_{1/2}MnO_3$ or in nickelates $RNiO_3$. After charge ordering, if both sites and bonds turns out to be inequivalent, leads to ferroelectricity. Another similar possibility is when the bonds are inequivalent because of the structure of the material, the site-centered charge order appearing on top of that. This is the case in an organic ferroelectric (TMTTF)2X

[49] and also in the multiferroic $LuFe_2O_4$ [50] [51].

1.5.2 Type II multiferroics:

Type II multiferroics are the materials in which one ferroic order is a by-product of another driven order parameters such as ferroelectric polarization as a by-product of spin order. For example: in $LuFeO_3$ thin films, a spin reorientation transition introduces weak ferromagnetism. From mechanism of multiferroic behavior view point, type II multiferroics can be divided into two types. 1. Ferroelectricity caused by magnetic spiral and 2. Ferroelectricity appears even for collinear magnetic structures.

Spiral multiferroics:

Most of the type-II multiferroics known to date belong to this subgroup. Ferroelectricity appears in conjunction with a spiraling magnetic phase, mostly of the cycloid type. This is the case in $TbMnO_3$, $Ni_3V_2O_6$ and $MnWO_4$. In an insulators, magnetic frustration is the source of spiral magnetic ordering. Hence, type II multiferroics are usually found in frustrated systems. Katsura, Nagaosa, and Balatsky [52], using a microscopic approach, and Mostovoy [53], using a phenomenological approach, showed that in a cycloidal spiral a polarization, P, appears,

that is given by:

$$P \sim r_{ij} \times [S_i \times S_j]\ Q \times e \tag{1.2}$$

where r_{ij} is the vector connecting neighboring spins S_i and S_j, Q is the wave vector describing the spiral, and e $\sim$ [S_i $\times$ S_j] is the spin rotation axis.

Collinear magnetic structures:

The second group of magnetically driven ferroelectrics are those in which ferroelectricity appears in collinear magnetic structures—that is all magnetic moments aligned along a particular axis—without the necessary involvement of the spin-orbit interaction. Polarization can appear in these materials as a consequence of exchange striction because the magnetic coupling varies with the atomic positions. The simplest example, found in Ca_3CoMnO_6 [54].

1.6 Resistive Random Access Memory

Resistive random-access memory (ReRAM or RRAM) is a type of non-volatile random-access computer memory that works by changing the resistance across a dielectric solid-state material under electric field. The high resistance states corresponds to the logic 0 and that of low

resistance to 1, respectively. It is one of the promising candidates that fulfill the requirements of next-generation NVM. A resistive switching memory cell in a RRAM is generally composed of capacitor-like MIM structure, with an insulating or resistive material 'I' sandwiched between two electron conductors 'M' [6]. Hickmott was the first to report the the hystereisis characteristics of I-V in MIM ($Al/Al_2O_3/Al$) in 1962, indicating resistive switching occurs as a result of applied electric fields [55]. RRAM also possess a good complementary metal-oxide semiconductor (CMOS) compatibility, which are vital for its practical applications and mass productions. The insulating resistance switch layer (dielectric layer) is the key component of the memory for switching, while in some cases, the top/bottom electrodes can also be involved in the RS process [56]. The resistance of the insulating layer can be switched by applying electric field to move certain conductive species, such as oxygen vacancies in oxide-based RRAM or metal ions in the case of Conductive-Bridge RRAM (CBRAM). The migration of these conductive species either causes formation/rupture of conductive filaments (CF) or modifies the interface barrier heights, resulting in the resistance change. The breaking and forming of a CF occurs over a nanometre-scale region within very short times at the nanosecond scale [57]. By applying appropriate programming or write voltage pulses V_{wr},

a cell in its high-resistance (OFF) state can be SET to a low-resistance (ON) state or RESET back into the OFF state i.e. transition from low resistance state to high resistance state [6] . In RRAM, the as-prepared memory cell is in high resistance state (HRS). With application of certain voltages, resistance suddenly drops. This process is called forming or electroforming process. Electroforming is typically conducted by applying high voltage/current to the as fabricated switching cell. The electroforming process leads to a large decrease in the resistance. The cell now at low resistance state (LRS). This pretreatment process is necessary in order to activate resistance switching in a switching material. After forming process, the cell is switched to high-resistance state (HRS) by applying a threshold voltage. This process of transition of LRS to HRS is called reset process. The cell is again switched to LRS from HRS by applying a threshold voltage, the process is called set process, which is normally larger than the reset voltage. When a device undergoes a forming process, it can not return to a pristine state. However, the HRS and LRS can be reversibly switched to each other. In some cases, there is no distinction in resistance between the HRS and the pristine state; this is called a "forming free" device.

1.7 Basic RRAM performance parameters:

1.7.1 Write and Read operation

Operating voltages should be very smaller in the range of few hundred mV to few V, to be compatible with CMOS. Also, read voltages need to be smaller than write voltages. The read time t_{rd} must be in the order of two or preferably shorter.

1.7.2 Resistance ratio

Resistance ratio, i.e. R_{OFF}/R_{ON} ratio is required to be greater than 10 for sense amplifier to be cost competitive with Flash. Higher resistance ratio is desirable for multi-bit or multi-level storages.

1.7.3 Endurance

Endurance is number of SET/RESET cycles that can be endured before HRS and the LRS are no longer distinguishable. Endurance needs to be grater than 10^7 to show an advantage over flash.

1.7.4 Retention

The intrinsic ability of the RRAM device to retain its stored state that has been programmed is called the retention time. A data retention time aim for 10 years is required for universal NVM.

1.8 Types of resistive switching

Resistive switching can be categorized into three groups: unipolar, bipolar, and threshold switching. Unipolar and bipolar switching exhibit at least two stable states without an applied bias, and these are therefore suitable for non-volatile memory applications. Threshold switching can also have multiple states in response to an applied bias; however, there is only one stable state when the external voltage is zero. The memory function is therefore volatile. Most article explain only two types; unipolar and bipolar.

1.8.1 Unipolar switching

Unipolar switching involves only one degree of freedom; the amplitude of the applied input voltage, not on the polarity. The HRS (as prepared memory) is also metastable and remains for a long period of time with no applied bias. When external voltage, V_{ext} is applied to the sample in the HRS, an abrupt reduction in resistance occurs, called set process. Typically set voltage is larger than reset voltage. Unipolar switching may occur both at positive polarity and negative polarity. In unipolar switching, both SET and RESET process exist at same polarity. They may occur at positive or negative polarity.

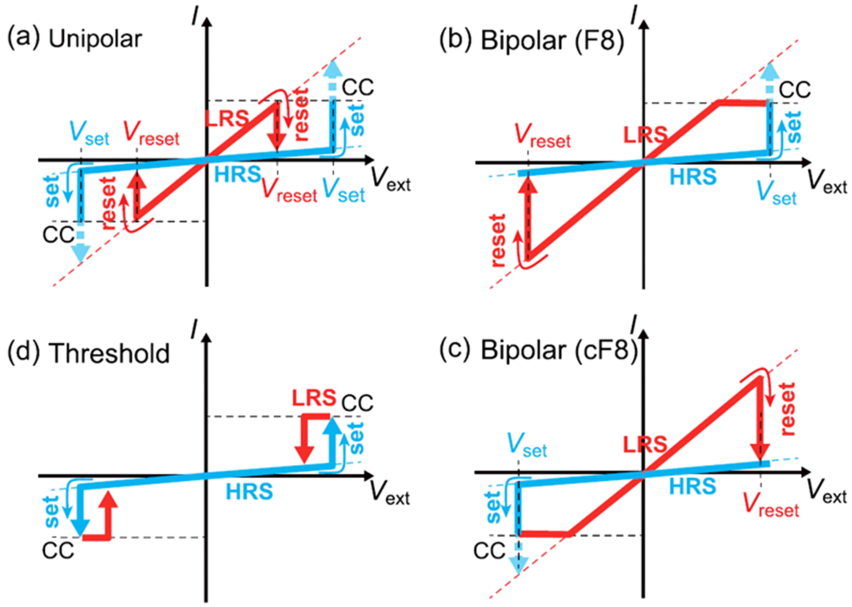

Figure 1.7: Schematics of types of switching, (a) typical unipolar I-V curve, (b) typical figure-of-eight (F8) bipolar I-V cureve, (c) counter-figure-of-eight (cF8) bipolar I-V curve, (d) typical threshold I-V curve. [58]

1.8.2 Bipolar switching

In bipolar switching, both voltage and polarity are involved. The switching from LRS-HRS is achieved in one direction (polarity), and HRS-LRS, i.e. set process occurs in another direction. There are two possible types of I-V curves of bipolar switching as shown in figure 1.7(b) and (c). Figure 1.7(b) in with the reset and set process occurs with negative and positive bias respectively, which is refer as figure of eight (F8) bipoar switching. In some bipolar switching, positive bias occur employs reset process, and negative bias employs set process as shown in Figure 1.7(c), which is referred as counter-figure-eight (cF8)

bipolar switching curve. Bipolar switching occurs in many oxide materials. Unipolar and bipolar switching behaviors are given by function of scalar and vector variable respectively.

1.8.3 Threshold switching

In threshold switching, there is only one stable state with no external bias. In threshold switching, the LRS is stable over only a certain range of applied biases, and when the applied bias falls below this range, the device reverts to HRS. The typical I-V curve for threshold switching is shown in figure 1.7(d). Although threshold switching occurs much less frequently than unipolar or bipolar, it can be a useful phenomenon, both scientifically as well as technologically. Due to the instability of some regions of CFs in LRS, threshold switching devices are not suitable for non-volatile memory applications. However, many potential technological applications using threshold switching have been proposed, including electrical switches, smart windows, terahertz nanoantennas, and memory metamaterials. In addition, it was recently proposed that threshold switching be used as a selector to solve a sneak path problem occurring in a RRAM crossbar array [57].

1.9 Literature Survey, Objectives and Material Selection

With the conventional flash memory approaching its scaling limits, NVM has attracted extensive attention. When the tunneling oxide thickness undergoes below 10 nm, the charge stored in the floating gate is lost due to direct tunneling current or defects formed in the tunneling oxide during long-term operation. Therefore, several types of NVMs such as ferroelectric random-access memory, magnetic random-access memory, multiferroics, and resistive random-access memory (RRAM) are being investigated.

Multiferroics (MF) are an important class of multifunctional materials those exhibit more than one ferroic orderings such as ferroelectric, ferromagnetic/antiferromagnetic/ferrimagnetic, ferroelastic and ferrotoroidic in the same phase [19, 38]. Magnetic random access memory (MRAM) writes data by switching magnetic states ($\pm$ M). A large magnetic field is required for switching process as the materials in MRAM possess high coercivity. In contrast, in case of Ferroelectric random access memory (FeRAM), data is written by polarization that is faster and energy efficient. However, read process in this case is slow and destructive in nature. For these reasons, the concept of ultimate memory device that performs the best functionality of MRAM with a non-

destructive magnetic read operation and FRAM with fast low power electrical write operation [59, 60, 61] could be the promising towards the fabrication of future memory device. On this concern multiferroic and/or magnetoelectric memories are gaining huge scientific attention. Interesting fundamental physics of cross coupling of order parameters as well as its potential applications in various fields, such as sensors, spintronics, logic devices [62, 63]. ME memory [64, 59, 60, 61], and voltage driven magnetic tunnel junction [65, 66] make these field much interesting. Unfortunately, very few naturally available materials exhibit multiferroicity due to the exclusive tendency of ferroelectricity and magnetism [61, 67]. A few MF are $BiFeO_3$ [44], $BiMnO_3$ [68], $TbMnO_3$ [69], $GaFeO_3$ [70], $BaMnF_4$ [71], $TbMn_2O_5$ [71] , Hexagonal Manganites $RMnO_3$ and RMn_2O_5 (R = Rare earth, Y and Bi) except $PrMn_2O_5$ [72]. Among these MF, $BiFeO_3$ is a well-known and intensely investigated RT single phase MF material with ferroelectric transitional temperature $\sim$ 1103 K and magnetic transition temperature $\sim$ 643 K exhibiting large magnetization $\sim$ 0.5 – 1.0 μB/Fe with significant spontaneous polarization (Pr $\sim$ 50 - 60 $\mu C/cm^2$) at room temperature in an epitaxial thin film [73]. Major drawbacks of BFO is its high leakage current and weak ME coupling, making the material unsuitable for application and weak ME coupling.

Most of the MF materials exhibit the magnetic and/or ferroelectric phase transition temperature either far lower or far higher than room temperature such as $BiMnO_3$ with magnetic transition temperature $\sim$105 K [74], $YbMnO_3$ with $\sim$ 80 K [75], and $BiFeO_3$ with $\sim$ 643 K [76]. Due to the large independence between the ferroelectric and magnetic ordering temperatures the ME coupling is observed to be small. The fundamental challenge is to realize both the ordering temperature above room temperature with strong ME coupling between the magnetic and electrical order parameters. So there are increasing activities in search of room temperature ME materials.

Gallium Ferrite ($GaFeO_3$/GFO) is a promising magnetoelectric material with room temperature piezoelectric and near room temperature ferrimagnetic behavior, possesses a significant ME coupling constant (10^{-11}s/m at 4.2 K) [70, 77, 78]. Single crystal of $GaFeO_3$ was first synthesized by Remeika in 1960 by flux grown method [70]. In same year,Wood [79] studied structural properties of this compound and identified the orthorhombic structure with eight formula units per unit cell having space group C^9_{2v}, $Pc2_1n$ which was later studied in detail by Abhram [80]. Large ME effect was later reported by Rado in 1964 [81]. The origin of piezoelectric effect was first studied by Abrahm in 1964 and suggests that it is originated due to oxygen-atom array in

the Ga1 oxygen tetrahedra [82]. Although earlier magnetic studies predicted ferromagnetic ordering in GFO [81, 82], the high field Mossbauer spectroscopy done by Frankel [77] proved ferrimagnetic ordering with magnetic moment directed to c-axis, which was later experimentally demonstrated by Arima through neutron diffraction pattern [78]. This study also showed that the curie temperature and the saturated magnetization increases with the increase of Fe contents, while the coercive force decreases. GFO retain its orthorhombic structure $Pc2_1n$ structure for large range of temperature 4 - 700 K which is shown by Mukherjee et al [83] using temperature dependent Raman spectroscopy. Study in GFO had been slowed down after 60's, however, extensive study arose in this field recently with advancement of preparation technique and characterization techniques.

Herein, the study of this document starts with the synthesis of GFO ceramics followed by the characterization of electric and magnetic properties. After the study of ceramics, thin films of as prepared ceramics were fabricated. The electric, magnetic and optical properties of the films were then carefully analyzed.

RRAM is another promising NVM, which is being highly investigated recently. Many different materials such as binary metal oxide, perovskite type oxides, organic materials have been successfully studied

exhibiting bistable switching of resistance, along with long time retention properties at both states. Amongst, simple binary oxdes such as NiO, TiO_2, HfO_2 ZrO_2 Nb_2O_5, and Cu_xO_{12} have been extensively investigated due to their simple compositions which are easily controlled during device fabrications. Al_2O_3 is a pioneer material in RRAM, that showed negative resistances phenomenon in anodic condition under vacuum [84]. Al_2O_3 has proven as a suitable material for RRAM due to its high energy bandgap of 8 eV and dielectric constants around 9. Atomic layer deposition AlOx based RRAM has been reported to have stable bipolar switching with 1T-1R configurations despite of large switching current and unstable switching cycling. Other reports also show a stable RS phenomenon in atmospheric conditions with promising results with a RF magnetron sputtered Al_2O_3 thick layer with a high ON/OFF ratio. The copper filament in e-beam evaporated AlOx has also been studied for RS behavior with a low average SET voltage of 1.5 V [85, 86, 87, 88, 89]. Recently, it was demonstrated that the reversible switching of local conductivity in thin Al_2O_3 film, used for magnetic tunnel junctions, was studied in situ by scanning tunneling microscopy (STM) under vacuum condition [90]. The resistive switching phenomenon in the Al_2O_3 thin film seems to be easily observed under vacuum condition, indicating that the phenomenon under vac-

uum might be more stable in comparison with that under the atmosphere condition. Kim *et al.* deposited Al_2O_3 resistive switching films by atomic layer deposition (ALD) between a Pt top electrode and a Ru bottom electrode to complete a MIM structure and performed the resistive switching behavior in a Pt/Al_2O_3/Ru device under atmosphere [91]. However, the resistive switching behavior in the Pt/Al_2O_3/Ru device showed large variations in both memory states due to more random formation and rupture of conducting filaments. Moreover, the conducting filaments inside the Pt/Al_2O_3/Ru device are more difficult to rupture, leading to a lower resistance ratio between high and low resistance states. In this document, we demonstrate the graphene integrated transparent resistive switching memory with Al_2O_3 insulating layer.

Bibliography

[1] ITRS WorkGroup. International technology roadmap for semiconductors, 2013 ed. *ITRS Technology Working Groups*, 2013.

[2] Jagan Singh Meena, Simon Min Sze, Umesh Chand, and Tseung-Yuen Tseng. Overview of emerging nonvolatile memory technologies. *Nanoscale research letters*, 9(1):526, 2014.

[3] John Gantz and David Reinsel. The digital universe in 2020: Big data, bigger digital shadows, and biggest growth in the far east. *IDC iView: IDC Analyze the future*, 2007(2012):1–16, 2012.

[4] Dawon Kahng and Simon M Sze. A floating gate and its appli-

cation to memory devices. *The Bell System Technical Journal*, 46(6):1288–1295, 1967.

[5] Hiro Akinaga and Hisashi Shima. Reram technology; challenges and prospects. *IEICE Electronics Express*, 9(8):795–807, 2012.

[6] Rainer Waser, Regina Dittmann, Georgi Staikov, and Kristof Szot. Redox-based resistive switching memories–nanoionic mechanisms, prospects, and challenges. *Advanced materials*, 21(25-26):2632–2663, 2009.

[7] Jun Yeong Seok, Seul Ji Song, Jung Ho Yoon, Kyung Jean Yoon, Tae Hyung Park, Dae Eun Kwon, Hyungkwang Lim, Gun Hwan Kim, Doo Seok Jeong, and Cheol Seong Hwang. A review of three-dimensional resistive switching cross-bar array memories from the integration and materials property points of view. *Advanced Functional Materials*, 24(34):5316–5339, 2014.

[8] Johan Åkerman. Toward a universal memory. *Science*, 308(5721):508–510, 2005.

[9] Claude Chappert, Albert Fert, and Frédéric Nguyen Van Dau. The emergence of spin electronics in data storage. *Nature Materials*, 6(11):813–823, 2007.

[10] Peter Wadley, Bryn Howells, J Železnỳ, Carl Andrews, Victoria Hills, Richard P Campion, Vit Novák, K Olejník, F Maccherozzi, SS Dhesi, et al. Electrical switching of an antiferromagnet. *Science*, 351(6273):587–590, 2016.

[11] Rainer Waser and Masakazu Aono. Nanoionics-based resistive switching memories. *Nature Materials*, 6:833–840, 2007.

[12] J Joshua Yang, Matthew D Pickett, Xuema Li, Douglas AA Ohlberg, Duncan R Stewart, and R Stanley Williams. Memristive switching mechanism for metal/oxide/metal nanodevices. *Nature nanotechnology*, 3(7):429–433, 2008.

[13] Alexander V Kolobov, Paul Fons, Anatoly I Frenkel, Alexei L Ankudinov, Junji Tominaga, and Tomoya Uruga. Understanding the phase-change mechanism of rewritable optical media. *Nature materials*, 3(10):703–708, 2004.

[14] Matthias Wuttig and Noboru Yamada. Phase-change materials for rewriteable data storage. *Nature materials*, 6(11):824–832, 2007.

[15] James F Scott and Carlos A Paz De Araujo. Ferroelectric memories. *Science*, 246(4936):1400–1405, 1989.

[16] Vincent Garcia, Stephane Fusil, Karim Bouzehouane, Shaima Enouz-Vedrenne, Neil D Mathur, Agnes Barthelemy, and Manuel Bibes. Giant tunnel electroresistance for non-destructive readout of ferroelectric states. *Nature*, 460(7251):81–84, 2009.

[17] Rui Guo, Lu You, Yang Zhou, Zhi Shiuh Lim, Xi Zou, Lang Chen, R Ramesh, and Junling Wang. Non-volatile memory based on the ferroelectric photovoltaic effect. *Nature communications*, 4(1):1–5, 2013.

[18] Stuart SP Parkin, Masamitsu Hayashi, and Luc Thomas. Magnetic domain-wall racetrack memory. *Science*, 320(5873):190–194, 2008.

[19] Manfred Fiebig. Revival of the magnetoelectric effect. *Journal of physics D: applied physics*, 38(8):R123, 2005.

[20] Wilma Eerenstein, ND Mathur, and James F Scott. Multiferroic and magnetoelectric materials. *nature*, 442(7104):759, 2006.

[21] Ce-Wen Nan, MI Bichurin, Shuxiang Dong, D Viehland, and G Srinivasan. Multiferroic magnetoelectric composites: Historical perspective, status, and future directions. *Journal of applied physics*, 103(3):1, 2008.

[22] Nicola A Spaldin, Sang-Wook Cheong, and Ramamoorthy Ramesh. Multiferroics: Past, present, and future. *Phys. Today*, 63(10):38–43, 2010.

[23] VK Wadhawan. Ferroic materials: A primer. *Resonance*, 7(7):15–24, 2002.

[24] Daniel B Litvin. Ferroic crystals and tensor distinction. *Phase Transitions*, 83(9):682–693, 2010.

[25] Kêitsiro Aizu. Possible species of ferromagnetic, ferroelectric, and ferroelastic crystals. *Physical Review B*, 2(3):754, 1970.

[26] Bas B Van Aken, Jean-Pierre Rivera, Hans Schmid, and Manfred Fiebig. Observation of ferrotoroidic domains. *Nature*, 449(7163):702, 2007.

[27] Kêitsiro Aizu. Second-order ferroic state shifts. *Journal of the Physical Society of Japan*, 34(1):121–128, 1973.

[28] RE Newnham and LE Cross. Secondary ferroics and domain-divided piezoelectrics. *Ferroelectrics*, 10(1):269–276, 1976.

[29] Tae Yun Kim, Sung Kyun Kim, and Sang-Woo Kim. Application of ferroelectric materials for improving output power of energy harvesters. *Nano convergence*, 5(1):30, 2018.

[30] Malcolm E Lines and Alastair M Glass. *Principles and applications of ferroelectrics and related materials*. Oxford university press, 2001.

[31] Joseph Valasek. The early history of ferroelectricity. *Ferroelectrics*, 2(1):239–244, 1971.

[32] Walter J Merz. Domain formation and domain wall motions in ferroelectric bati o 3 single crystals. *Physical Review*, 95(3):690, 1954.

[33] OG Vendik and SP Zubko. Ferroelectric phase transition and maximum dielectric permittivity of displacement type ferroelectrics (ba x sr 1- x tio 3). *Journal of Applied Physics*, 88(9):5343–5350, 2000.

[34] HT Martirena and JC Burfoot. Grain-size and pressure effects on the dielectric and piezoelectric properties of hot-pressed pzt-5. *Ferroelectrics*, 7(1):151–152, 1974.

[35] IA dos Santos and JA Eiras. Phenomenological description of the diffuse phase transition in ferroelectrics. *Journal of Physics: condensed matter*, 13(50):11733, 2001.

[36] J Samuel Smart. The néel theory of ferrimagnetism. *American Journal of Physics*, 23(6):356–370, 1955.

[37] Hans Schmid. Multi-ferroic magnetoelectrics. *Ferroelectrics*, 162(1):317–338, 1994.

[38] ZH Sun, BL Cheng, S Dai, LZ Cao, YL Zhou, KJ Jin, ZH Chen, and GZ Yang. Dielectric property studies of multiferroic gafeo3. *Journal of Physics D: Applied Physics*, 39(12):2481, 2006.

[39] AJC Buurma, GR Blake, TTM Palstra, and Umut Adem. Multiferroic materials: Physics and properties. 2016.

[40] Shuai Dong, Jun-Ming Liu, Sang-Wook Cheong, and Zhifeng Ren. Multiferroic materials and magnetoelectric physics: symmetry, entanglement, excitation, and topology. *Advances in Physics*, 64(5-6):519–626, 2015.

[41] Felix Fernandez Alonso and David L Price. *Neutron Scattering Magnetic and Quantum Phenomena*. 2015.

[42] Nicola A Spaldin and Manfred Fiebig. The renaissance of magnetoelectric multiferroics. *Science*, 309(5733):391–392, 2005.

[43] Ramaroorthy Ramesh and Nicola A Spaldin. Multiferroics: progress and prospects in thin films. *Nature materials*, 6(1):21, 2007.

[44] Gustau Catalan and James F Scott. Physics and applications of bismuth ferrite. *Advanced materials*, 21(24):2463–2485, 2009.

[45] VA Bokov, IE Mylnikova, and GA Smolenskii. Ferroelectric antiferromagnetics. *Soviet Physics Jetp-Ussr*, 15(2):447–449, 1962.

[46] Takuro Katsufuji and H Takagi. Coupling between magnetism and dielectric properties in quantum paraelectric eutio 3. *Physical Review B*, 64(5):054415, 2001.

[47] Bas B Van Aken, Thomas TM Palstra, Alessio Filippetti, and Nicola A Spaldin. The origin of ferroelectricity in magnetoelectric ymno 3. *Nature materials*, 3(3):164–170, 2004.

[48] Wenbin Wang, Jun Zhao, Wenbo Wang, Zheng Gai, Nina Balke, Miaofang Chi, Ho Nyung Lee, Wei Tian, Leyi Zhu, Xuemei Cheng, et al. Room-temperature multiferroic hexagonal lufeo 3 films. *Physical review letters*, 110(23):237601, 2013.

[49] Pierre Monceau, F Ya Nad, and Serguei Brazovskii. Ferroelectric mott-hubbard phase of organic (tmttf) 2 x conductors. *Physical review letters*, 86(18):4080, 2001.

[50] Naoshi Ikeda, Kay Kohn, Nobuyuki Myouga, Eri Takahashi, Hijiri Kitôh, and Shunji Takekawa. Charge frustration and dielectric dispersion in lufe2o4. *Journal of the Physical Society of Japan*, 69(5):1526–1532, 2000.

[51] Daniel Khomskii. Trend: Classifying multiferroics: Mechanisms and effects. *Physics*, 2:20, 2009.

[52] Hosho Katsura, Naoto Nagaosa, and Alexander V Balatsky. Spin current and magnetoelectric effect in noncollinear magnets. *Physical review letters*, 95(5):057205, 2005.

[53] Maxim Mostovoy. Ferroelectricity in spiral magnets. *Physical Review Letters*, 96(6):067601, 2006.

[54] YJ Choi, HT Yi, S Lee, Q Huang, Valery Kiryukhin, and S-W Cheong. Ferroelectricity in an ising chain magnet. *Physical review letters*, 100(4):047601, 2008.

[55] Akihito Sawa. Resistive switching in transition metal oxides. *Materials today*, 11(6):28–36, 2008.

[56] Linggang Zhu, Jian Zhou, Zhonglu Guo, and Zhimei Sun. An overview of materials issues in resistive random access memory. *Journal of Materiomics*, 1(4):285–295, 2015.

[57] Doo Seok Jeong, Reji Thomas, RS Katiyar, JF Scott, H Kohlstedt, A Petraru, and Cheol Seong Hwang. Emerging memories: resistive switching mechanisms and current status. *Reports on progress in physics*, 75(7):076502, 2012.

[58] Jae Sung Lee, Shinbuhm Lee, and Tae Won Noh. Resistive switching phenomena: A review of statistical physics approaches. *Applied Physics Reviews*, 2(3):031303, 2015.

[59] Shan X Wang and Alex M Taratorin. *Magnetic Information Storage Technology: A Volume in the Electromagnetism Series*. Elsevier, 1999.

[60] JF Scott. Multiferroic memories. *Nature materials*, 6(4):256–257, 2007.

[61] Amritendu Roy, Rajeev Gupta, and Ashish Garg. Multiferroic memories. *Advances in Condensed Matter Physics*, 2012, 2012.

[62] Enno Lage, Christine Kirchhof, Viktor Hrkac, Lorenz Kienle, Robert Jahns, Reinhard Knöchel, Eckhard Quandt, and Dirk Meyners. Exchange biasing of magnetoelectric composites. *Nature materials*, 11(6):523–529, 2012.

[63] Casey Israel, ND Mathur, and JF Scott. A one-cent room-temperature magnetoelectric sensor. *Nature materials*, 7(2):93–94, 2008.

[64] Xi Chen, Andreas Hochstrat, Pavel Borisov, and Wolfgang Kleemann. Magnetoelectric exchange bias systems in spintronics. *Applied physics letters*, 89(20):202508, 2006.

[65] Martin Gajek, Manuel Bibes, Stéphane Fusil, Karim Bouzehouane, Josep Fontcuberta, Agnes Barthelemy, and Albert Fert. Tunnel junctions with multiferroic barriers. *Nature materials*, 6(4):296–302, 2007.

[66] Leonard F Henrichs, Oscar Cespedes, James Bennett, Joachim Landers, Soma Salamon, Christian Heuser, Thomas Hansen, Tim

Helbig, Oliver Gutfleisch, Doru C Lupascu, et al. Multiferroic clusters: a new perspective for relaxor-type room-temperature multiferroics. *Advanced Functional Materials*, 26(13):2111–2121, 2016.

[67] Nicola A Hill. Why are there so few magnetic ferroelectrics?, 2000.

[68] Bo Wha Lee, Pil Sun Yoo, Vu Binh Nam, Kirstie Raquel Natalia Toreh, and Chang Uk Jung. Magnetic and electric properties of stoichiometric bimno 3 thin films. *Nanoscale research letters*, 10(1):1–5, 2015.

[69] S Quezel, F Tcheou, J Rossat-Mignod, G Quezel, and E Roudaut. Magnetic structure of the perovskite-like compound tbmno3. *Physica B+ C*, 86:916–918, 1977.

[70] JP Remeika. Gafeo 3: a ferromagnetic-piezoelectric compound. *Journal of Applied Physics*, 31(5):S263–S264, 1960.

[71] A Poole, B Roessli, O Zaharko, and KW Krämer. The magnetic structure of multiferroic bamnf4. *Journal of Physics: Condensed Matter*, 23(26):266004, 2011.

[72] Mohamed Balli, Benoit Roberge, Patrick Fournier, and Serge Jandl. Review of the magnetocaloric effect in rmno3 and rmn2o5 multiferroic crystals. *Crystals*, 7(2):44, 2017.

[73] JBNJ Wang, JB Neaton, H Zheng, V Nagarajan, SB Ogale, B Liu, D Viehland, V Vaithyanathan, DG Schlom, UV Waghmare, et al. Epitaxial bifeo3 multiferroic thin film heterostructures. *science*, 299(5613):1719–1722, 2003.

[74] Pierre Toulemonde, Pierre Bordet, Pierre Bouvier, and Jens Kreisel. Single-crystalline bimno 3 studied by temperature-dependent x-ray diffraction and raman spectroscopy. *Physical Review B*, 89(22):224107, 2014.

[75] X Fabreges, I Mirebeau, P Bonville, S Petit, G Lebras-Jasmin, A Forget, G André, and S Pailhes. Magnetic order in ybmno 3 studied by neutron diffraction and mössbauer spectroscopy. *Physical Review B*, 78(21):214422, 2008.

[76] Jean-Michel Moreau, Christian Michel, Robert Gerson, and William Joseph James. Ferroelectric bifeo3 x-ray and neutron diffraction study. *Journal of Physics and Chemistry of Solids*, 32(6):1315–1320, 1971.

[77] Richard B Frankel, NA Blum, S Foner, Arthur J Freeman, and M Schieber. Ferrimagnetic structure of magnetoelectric ga 2- x fe x o 3. *Physical Review Letters*, 15(25):958, 1965.

[78] T Arima, D Higashiyama, Y Kaneko, JP He, T Goto, S Miyasaka, T Kimura, K Oikawa, T Kamiyama, R Kumai, et al. Structural and magnetoelectric properties of ga 2- x fe x o 3 single crystals grown by a floating-zone method. *Physical Review B*, 70(6):064426, 2004.

[79] Elizabeth A Wood. The unit cell and space group of gallium iron oxide, a piezoelectric ferromagnetic crystal. *Acta Crystallographica*, 13(8):682–682, 1960.

[80] SC Abrahams, JM Reddy, and JL Bernstein. Crystal structure of piezoelectric ferromagnetic gallium iron oxide. *The Journal of Chemical Physics*, 42(11):3957–3968, 1965.

[81] George T Rado. Observation and possible mechanisms of magnetoelectric effects in a ferromagnet. *Physical Review Letters*, 13(10):335, 1964.

[82] SC Abrahams and JM Reddy. Magnetic, electric, and crystallographic properties of gallium iron oxide. *Physical Review Letters*, 13(23):688, 1964.

[83] Somdutta Mukherjee, Ashish Garg, and Rajeev Gupta. Probing magnetoelastic coupling and structural changes in magnetoelectric gallium ferrite. *Journal of Physics: Condensed Matter*, 23(44):445403, 2011.

[84] Chih-Yang Lin, Chen-Yu Wu, Chung-Yi Wu, Chenming Hu, and Tseung-Yuen Tseng. Bistable resistive switching in al2o3 memory

thin films. *Journal of the Electrochemical Society*, 154(9):G189, 2007.

[85] Rajeswar Panja, Sourav Roy, Debanjan Jana, and Siddheswar Maikap. Impact of device size and thickness of al 2 o 3 film on the cu pillar and resistive switching characteristics for 3d cross-point memory application. *Nanoscale research letters*, 9(1):692, 2014.

[86] L Goux, N Raghavan, Andrea Fantini, R Nigon, S Strangio, R Degraeve, G Kar, Yang Yin Chen, Francesca De Stefano, VV Afanas' Ev, et al. On the bipolar resistive-switching characteristics of al2o3-and hfo2-based memory cells operated in the soft-breakdown regime. *Journal of Applied Physics*, 116(13):134502, 2014.

[87] Andrey S Sokolov, Seok Ki Son, Donghwan Lim, Hoon Hee Han, Yu-Rim Jeon, Jae Ho Lee, and Changhwan Choi. Comparative study of al2o3, hfo2, and hfalox for improved self-compliance bipolar resistive switching. *Journal of the American Ceramic Society*, 100(12):5638–5648, 2017.

[88] L Goux, Karl Opsomer, R Degraeve, R Müller, Christophe Detavernier, DJ Wouters, M Jurczak, L Altimime, and JA Kittl. Influence of the cu-te composition and microstructure on the resistive switching of cu-te/al2o3/si cells. *Applied Physics Letters*, 99(5):053502, 2011.

[89] A Sleiman, PW Sayers, and MF Mabrook. Mechanism of resistive switching in cu/alox/w nonvolatile memory structures. *Journal of applied physics*, 113(16):164506, 2013.

[90] O Kurnosikov, FC De Nooij, Patrick R LeClair, JT Kohlhepp, B Koopmans, HJM Swagten, and WJM De Jonge. Stm-induced reversible switching of local conductivity in thin al2o3 films. *PHYSICAL REVIEW B Phys Rev B*, 64:153407, 2001.

[91] Kyung Min Kim, Byung Joon Choi, Bon Wook Koo, Seol Choi, Doo Seok Jeong, and Cheol Seong Hwang. Resistive switching in

pt/ al2o3/ tio2/ ru stacked structures. *Electrochemical and Solid State Letters*, 9(12):G343, 2006.

Chapter 2

Synthesis techniques and experimental details

This chapter focuses on the experimental techniques and characteristics used in the development of this thesis. At first, the technologies employed for ceramic preparation and the thin film synthesis is addressed. Finally, the functional and characterization techniques implemented is mentioned.

2.1 Synthesis of multiferroic ceramic oxides

Synthesis of high-quality material is essential for multifunctional device application. On ceramic processing, different factors such as purity of raw materials, degree of mixing, calcination and/or sintering temperatures as well as time affect the quality of ceramics. Thus, various processing parameters must be taken care during material preparation to achieve the best possible results. The pure $GaFeO_3$ ceramic targets

have been synthesized by solid state reaction method.

2.1.1 Solid state reaction method

Solid-state reaction route is the most widely used method for the preparation of polycystalline solids from the mixture of solid materials. The advantage of solid-state reactions is the easy availability of the precursors and the low cost of powder production on the industrial scale. Mostly solid-state chemical reaction process consists of four steps: diffusion, reaction, nucleation, and growth. The end-product depends on nucleus growth during these processes. When the nucleation rate is greater than the nucleus's growth speed, formation of nanocrystallite is expected, whereas if the nucleus's growing rate is greater than the nucleation rate, a lump crystal forms [1, 2, 3]. Solid state reaction is accomplished by the homogenous mixture of stoichiometric weighted compounds followed by following steps:

Mixing

Homogenous mixture of highly pure powder is crucial to obtain desired compound with high quality. The stoichiometric weighed compounds are mixed with acetone medium placed in stirrer for 10 - 12 hours at temperature of about 70 - 80°C. The mixture is then brought to dry at room temperature by grinding in mortar and pestle. Ball milling is

another process to carry out mixing.

Calcination

Calcination refers to the process of heating a substance to a high temperature in a controlled environment. The phase composition, particle size and aggregation of ceramic powders is determined primarily during the calcination process. The balance of thermodynamic and kinetic processes take place during this activity. The main purpose of this procedure is i) to remove a volatile substance, ii) to cause loss of moisture, reduction or oxidation, iii) to create new phase and iv) to optimize particle size and surface area of the particles.

Grinding and pressing

Thorough grinding of calcined mixture is necessary to achieve a homogenous mixture of reactants as well as to improve the reactivity of the reactants. The calcined powder is grinded in mortal and pestle to obtain fine powder to reduce the particle size and promote the fine mixing of any residual unreacted oxides. The finely grinded mixture pressed in hydraulic press to get a desired shape of the pellets and targets. Before pressing, a few drops of saturated solution of polyvinyl alcohol (PVA) is mixed with calcined powder and grounded uniformly to enhance the adhesive property.

Sintering

Sintering is the process by which a compact powder material transform to a dense material through thermal treatment. Usually, this process is performed slightly above calcination temperature and below the melting point of the desired phase in order to improve crystal quality by minimizing defects, enhance grain growth (reducing the total area of grain boundary) and to achieve maximum possible density.

2.2 Pulse Laser Deposition

Pulsed laser deposition (PLD) is a physical vapor deposition (PVD) technique to deposit thin film. It is one of the most popular techniques for the growth of functional oxide thin films [4]. The PLD technique involves three main steps: ablation of the target material, formation of a highly energetic plume, and the growth of the film on the substrate. During this process, energy from laser source is used to excite the target surface, subsequently resulting in electronic excitation, heating and physical ablation of the surface atoms/molecules. This produces a transient, highly luminous plasma plume containing neutrals, ions, atoms, molecules, electrons etc., expand rapidly away from the target surface. The threshold power density needed to produce such a plume depends on the target material, its morphology and the laser pulse wavelength

and duration [5, 6]. The ablated material is collected on an suitably placed substrate upon which it condenses and the thin film grows.

The PLD chamber is equipped with target holder, target corrousel, laser beam, substrate heater, and vacuum pumps etc. The schematic diagram is shown in figure 2.1.

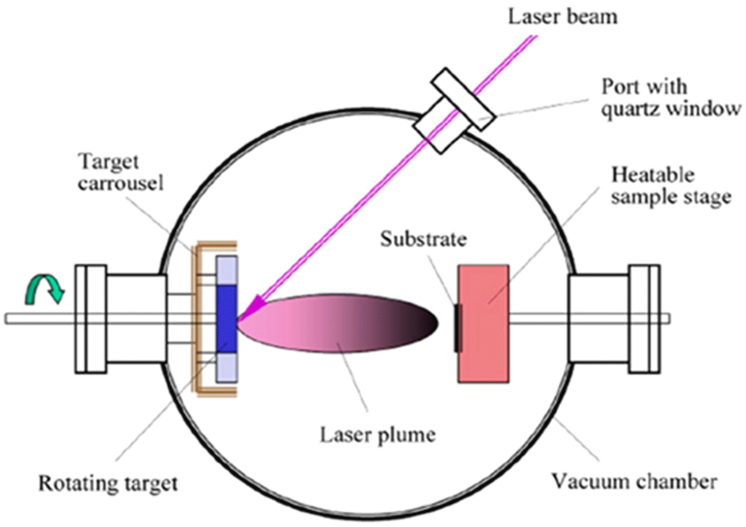

Figure 2.1: Schematic diagram of PLD

2.2.1 Advantages of PLD:

1. **Versatile:** Single chamber may include many target holders. Hence, placing many targets, many materials can be deposited in a wide variety of gases simultaneously.

2. **Cost effective:** One laser can serve many vacuum systems.

3. **Simple:** A desired thin film of any composition can be achieved once the target is available.

4. **Efficacy:** The energy source is well confined at the surface of the target, and by that it contributes to the efficiency, flexibility and the control of the processes.

5. **Flexibility:** The energy source is external to the deposition chamber, and can be adjusted in energy and wavelength to meet almost each experimental demand.

2.2.2 Disadvantages of PLD:

1. **Growth scale:** It is not suitable for large scale film growth.

2. **Uneven coverage:** Thin films may not be grown uniformly.

3. **Roughness:** Droplets and clusters may appear at the surface of the films that leads to higher roughness, that further leads to bad optical, electrical, magnetic and even crystalline properties.

2.3 Atomic Layer Deposition

Atomic layer deposition (ALD) technique is an advanced deposition technique with greater potential for producing very thin, conformal

films with control of the thickness and composition of the films possible at the atomic level. The trend of shrinking of device dimensions and increasing aspect ratios in integrated circuits (IC) require the introduction of new materials and advanced thin-film deposition techniques. The International Technology Roadmap for Semiconductoes (ITRS) has included ALD for high dielectric constant gate oxides in the MOSFET structure and for copper diffusion barriers in backend interconnects. In addition, ALD has met challenging requirements in other areas including the deposition of high quality dielectrics to fabricate trench capacitors for DRAM as well as metals and nitrides for electrodes and interconnects. ALD is already being utilized as a high potential technique to deposit high-k (high permittivity) gate oxides, high-k memory capacitor dielectrics, ferroelectrics, and multiferroics [7, 8, 9, 10].

2.3.1 Principle of ALD

ALD is a special modification of chemical vapor deposition (CVD) with the distinct feature that film growth takes place in a cyclic manner. Ultra thin-films in this technique are typically synthesized sub-monolayer by sub-monolayer by repeating two subsequently executed half-cycles. The first half cycle is involved with precursor consists of two steps; 1)

Exposure of the precursor and 2) purge of the excess precursor. The second half is involved with reactor, that also consists of two steps; 1) exposure of the reactor, and 2) a further purge of the excess reactor from reaction chamber [10, 11]. The schematic illustration of these cycles is shown in figure 2.2 . The growth cycles are repeated as many times as required for the desired film thickness. Depending on the process and the reactor being used, one cycle can take time from 0.5 s to a few seconds, and may deposit between 0.1 and 3 Å of film material [10].

In this studies, ALD tool named ALD R200 Advanced is used to deposit ALD thin films. This ALD-tool consists of a carrier gas system, precursor source system, a reaction chamber, a vacuum system and a lift system. The carrier gas has two basic functions during the deposition process. It creates a flow to the carrier gas line, which carries the precursor to the reaction chamber, thus, enabling the ALD reaction. Secondly, it operates as the purging gas, which purges the reaction chamber between the pulses. In addition, the carrier gas is also used to bring the reaction chamber to atmospheric pressure after the deposition. Every precursor source system is attached to a carrier gas line by a pneumatic ALD pulsing valve. The carrier gas is always flowing through the ALD valve independent of the activation state of

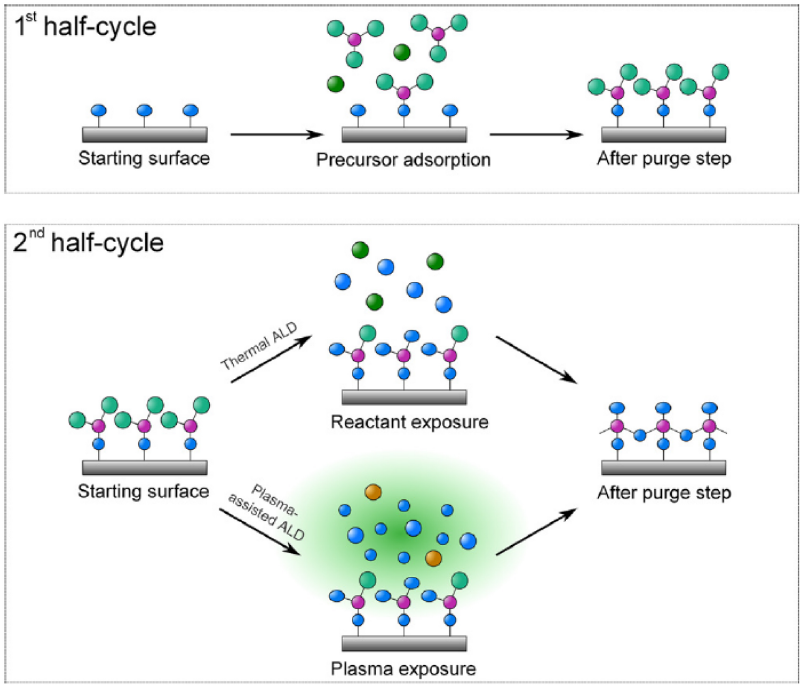

Figure 2.2: schematic representation of thermal ALD and plasma-assisted ALD. During the co-reactant step of the cycle (the 2nd halfcycle), the surface is exposed to a reactant gas or vapor such as NH_3 or H_2O, or to species generated by a plasma.

the valve. The tool is equipped with different precursor-source-system for solid and liquid precursors. The reactor comprises of two chambers, the outer is vacuum chamber and inner is reaction chamber where substrate holder and heater are situated. Deposition of thin films takes place in reaction chamber. The vacuum system is connected to the reactor with a pumping line.

In this document, thin films of Al_2O_3 are grown in this system with plasma-assisted reagent. Transparent resistive random access memory

(T-RRAM) study has been carried out in Al_2O_3 films grown in this system.

2.4 Experimental Techniques

2.4.1 X-ray Diffraction

X-rays are a form of electro-magnetic radiation. These occur in the region of the electromagnetic spectrum between 0.01 nm and 10 nm. This wavelength is bounded on the short wavelength side by Gamma rays and on the long wavelength side by Ultra-Violet radiation. Xray Diffraction (XRD) is an efficient analysis technique to analyze all kinds of matter ranging from fluids to powder and crystals. XRD was first discovered by Max von Laue in 1912 in three dimensional diffraction grating [12]. This technology got much attention after W.H.Bragg and W.L.Bragg (father and son) used this technology to confirm Barlow's hypothetic model of rock salt, which is the first X-ray diffraction analysis of single crystal [13, 14]. Bragg's laboratory then became the school and center for the development of this new method, with analysis of polycrystalline samples and later used this technology in mineralogy, that revealed the theory that only 127 groups exist in nature, while the rest 103 called nonsymmophic could not occur in reality.

X-Ray are produced in a cathode ray tube when high energy elec-

tron (generated from hot tungsten filament), suddenly decelerate and collide with metal target(anode) under high vacuum. Anode is mainly Cu, Mo, Al and Mg. After the discovery of the diffraction of X-rays by crystal, Bragg and his son derived Bragg's law, which relates the wavelength of X-ray to the glancing angle of reflection, given by 2d sin θ = nλ, where n is an integer determined by the order, λ is the wavelength of x-ray, and moving electrons, protons and neutrons, d is the spacing between the planes in the atomic lattice and θ is the angle between the incident ray and the scattering planes. Bragg diffraction occurs when

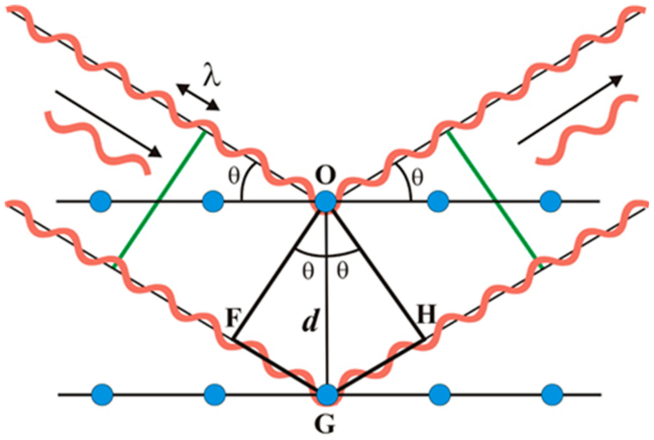

Figure 2.3: Bragg's diffraction

electromagnetic radiation or subatomic particle waves with wavelength comparable to atomic spacings, are incident upon a crystalline sample, scattered by the atoms in the system and undergo constructive interference in accordance to Bragg's law.

The advantages of X-ray Powder Diffraction are:

- Rapid identification of materials.
- Ease of sample preparation.
- Computer-aided material identification.
- Large library of known crystalline structures.
- Multi-sample stage.

Other applications include:

- characterization of crystalline materials.
- identification of fine-grained minerals such as clays and mixed layer clays that are difficult to determine optically
- determination of unit cell dimensions
- measurement of sample purity

With specialized techniques, XRD can be used to:

- determine crystal structures using Rietveld refinement
- determine of modal amounts of minerals (quantitative analysis)
- characterize thin films samples by:

  - determining lattice mismatch between film and substrate and to inferring stress and strain
  - determining dislocation density and quality of the film by rocking curve measurements
  - measuring superlattices in multilayered epitaxial structures
  - determining the thickness, roughness and density of the film using glancing incidence X-ray reflectivity measurements
- make textural measurements, such as the orientation of grains, in a polycrystalline sample

The scattering of X-rays from atoms produces a diffraction pattern, which contains information about the atomic arrangement within the crystal. In this study, the XRD measurements are carried out using Rigaku Smartlab X-Ray Diffractometer (XRD) equipped with Cu anode x-ray tube with x-ray wavelength 1.54 Å(Cu kα) operating in Brag-Brentano mode. Phases are identified from XRD patterns by comparing peak positions with database entries with JCPDF files. After identification of phase, further refinement of structure and profile parameters are done with Rietvelt refinement. Rietveld refinement technique is used in the characterization of crystalline materials. This method uses a least squares approach to refine a theoretical line profile until it matches the

measured profile.

2.4.2 Raman Spectroscopy

Raman spectroscopy is a valuable tool for studying molecular vibrations, whether in the industrial or the laboratory setting. Raman scattering along with infrared (IR) absorption is used to obtain information about the structure and properties of molecules from their vibrational transition. IR absorption arises from a direct resonance between the frequency of the IR radiation and the vibration frequency of a particular normal mode of vibration. In Raman spectroscopy, the sample is irradiated by intense laser beam in the UV- visible region (ν_o) and the scattered light is usually observed in direction perpendicular to the incident beam. The scattered light consists of two types: (i) Rayleigh scattering, is strong and has the frequency same as the incident beam (ν_o) and (ii) Raman scattering which is weak and has frequency $\nu_o \pm \nu_m$, where ν_m is a vibrational frequency of a molecule. The ν_o - ν_m and $\nu_o + \nu_m$ lines are called Stokes and anti-Stokes lines respectively.

According to classical theory, Raman scattering can be explained as follows: The electric field strength (E) of the electromagnetic wave (laser beam) fluctuates with time (t) is given by

$$E = E_o cos 2\pi\nu_o t \tag{2.1}$$

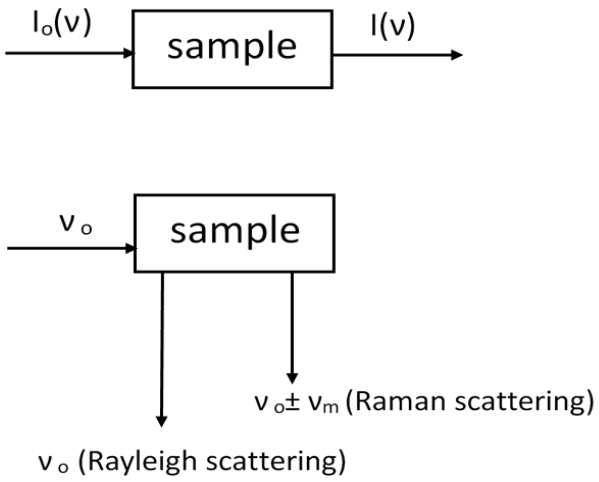

Figure 2.4: Schematics of Rayleigh and Raman scattering process.

where E_o is the vibrational amplitude and ν_o is the frequency of the laser. If a diatomic molecule is irradiated by this light, an electric dipole moment P is induced:

$$P = \alpha E = \alpha E_o cos 2\pi \nu_o t \tag{2.2}$$

Here, α is a proportionality constant and is called polarizability. If the molecule is vibrating with a frequency ν_m the nuclear displacement q is written

$$q = q_o cos 2\pi \nu_m t \tag{2.3}$$

where q_o is the vibrational amplitude. For a small amplitude of

vibration, α is a linear function of q. Thus, it can be written as

$$\alpha = \alpha_o + (\frac{d\alpha}{dq})q_o.... \tag{2.4}$$

where, α_o is the polarizability at the equilibrium position, and dα/dq is the rate of change of α with respect to the change in q, evaluated at the equilibrium position. Combining equation 2.2 with 2.3 and 2.4 we obtain

P=α E_o cos2$\pi\nu_o$t

=α_o E_o cos2$\pi\nu_o$t +$(\frac{d\alpha}{dq})_o$ q E_o cos2$\pi\nu_o$t

=α_o E_o cos2$\pi\nu_o$t + +$(\frac{d\alpha}{dq})_o$ q_o cos2$\pi\nu_m$t E_o cos2$\pi\nu_o$t

$$= \alpha_o E_o cos2\pi\nu_o t + +1/2(\frac{d\alpha}{dq})_o q_o E_o[cos2\pi(\nu_o + \nu_m)t + cos2\pi(\nu_o - \nu_m)t] \tag{2.5}$$

According to classical theory, the first term represents an oscillating dipole that radiates light of frequency ν_o (Rayleigh scattering), while the second term corresponds to the Raman scattering of frequency ν_o + ν_m (anti-Stokes) and ν_o - ν_m(Stokes). If (dα/dq)$_o$ is zero, the vibration is not Raman-active. Namely, to be Raman-active, the rate of change of polarizability (α) with the vibration must not be zero [15, 16].

In the present work, Raman measurement were performed in backscattering geometry using Jobin Yvon T64000 spectrometer equipped with

a triplegrating monochromator and a Coherent Innova 90C argon ion laser operating at 514.5 nm. A liquid-nitrogen-cooled charge coupled device (CCD) collects and process the Raman scattered signal through 50x objective. Temperature dependent Raman spectra of the sample is collected in vacuum using a Linkam module.

2.4.3 Scanning Electron Microscopy

Scanning electron microscopy (SEM) is a versatile technology used for imaging a surface of material. In this technology, the incident electron beam scans across the sample surface and interacts with the sample to generate backscattered secondary electrons that are used to create an image of the sample. Due to its high lateral resolution, its great depth of focus and its facility for X-ray microanalysis, SEM is often used in materials science including polymer science to elucidate the microscopic structure or to differentiate several phases from each other [17].

The types of signals produced by an SEM include secondary electrons, back-scattered electrons (BSE), characteristic X-rays, light (cathodoluminescence), specimen current and transmitted electrons. The signals result from interactions of the electron beam with atoms at or near the surface of the sample, as shown in schematic figure 2.5. The electron beams are very narrow, due to which the micrographs have a large

depth of field yielding a characteristic three-dimensional appearance. This technique is useful for understanding the surface structure of a sample. Back-scattered electrons (BSE) are beam electrons that are reflected from the sample by elastic scattering. BSE are often used in analytical SEM along with the spectra made from the characteristic X-rays. As the intensity of the BSE signal is strongly related to the atomic number (Z) of the specimen, BSE images can provide information about the distribution of different elements in the sample. Characteristic X-rays are emitted when the electron beam removes an inner shell electron from the sample, causing a higher energy electron to fill the shell and release energy [18, 19]. These characteristic X-rays are used to identify the composition and measure the abundance of elements in the sample.

In this work, the microstructure grain growth and surface topography of the samples was analyzed using a scanning electron microscope (SEM) (JEOL JSM-6480LV) at a magnification of 5000x and 1000x operated with an accelerating voltage of 20 V.

2.4.4 Energy Dispersive X-ray

Energy Dispersive X-Ray (EDX) is a technique of elemental analysis based on the generation of characteristic Xrays in atoms of the spec-

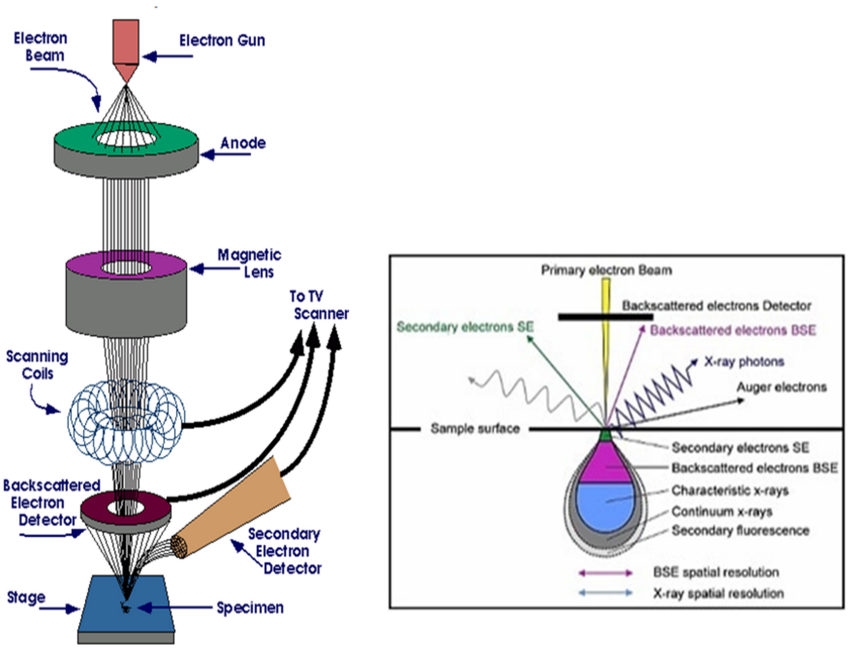

Figure 2.5: Schematics of SEM

imen by the incident beam electrons. The incident beam may excite an electron in an inner shell, ejecting it from the shell, creating an electron-hole. During this period, two fundamental physical events occur; elastic scattering and an inelastic scattering. Elastic scattering involves a change in direction of the electron without loss in energy. It is generally caused by interactions with the nucleus comprising the materials. The inelastic scattering is loss of energy with no noticeable change in direction, usually generated from interaction with both the bound electrons and the nucleus in the atoms. Nevertheless, the atoms are ionized. An electron from an outer, higher-energy shell then fills

the hole, and the difference in energy between the higher-energy shell and the lower energy shell may be released in the form of an X-ray [20, 21, 22].

2.4.5 X-ray Photo Spectroscopy

X-ray Photoelectron spectroscopy (XPS) is a surface characterization technique that can reveal which chemical elements are present at the surface and the nature of the chemical bond that exists between these elements, except hydrogen and helium [23, 24]. XPS spectra are obtained by irradiating a material with a beam of X-rays while simultaneously measuring the kinetic energy and number of electrons that escape from the top 1 to 10 nm (escape depth) of the material being analyzed. XPS requires ultra high vacuum conditions. Because the energy of a particular X-ray wavelength equals a known quantity, we can determine the electron binding energy (E_b) of the emitted electrons by using an equation that is based on the work of Ernest Rutherford $E_b = h\nu - E_{kin} - W_f$ where E_b is the energy of the electron emitted from one electron configuration within the atom, $h\nu$ is the energy of the X-ray photons being used, E_{kin} is the kinetic energy of the emitted electron as measured by the instrument and W_f is the work function of the material [23]. Each element produces a characteristic set of XPS

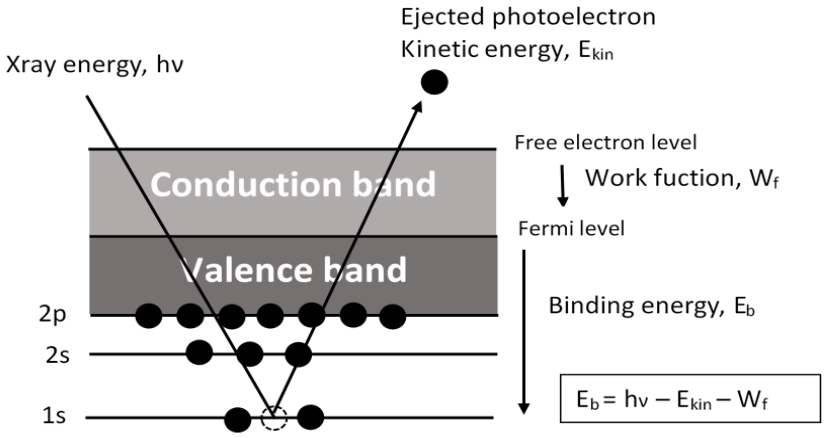

Figure 2.6: Schematic of the principle of XPS

peaks at characteristic binding energy values that directly identify each element that exists in or on the surface of the material being analyzed.

2.4.6 Magnetic Characterization

Magnetic properties of the samples in this study are measured in Physical Property Measurement System (PPMS) at Vibrating Sample Magnetometer (VSM) mode from Quantum Design. VSM works on the principle that a changing magnetic flux will induce a voltage in a pickup coil. The time dependent induced voltage is given by the equation:

$$V_{coil} = \frac{d\phi}{dt} = \frac{d\phi}{dz}\frac{dz}{dt} \tag{2.6}$$

where ϕ is the magnetic flux enclosed by the pickup coil, z is the vertical sample w.r.t the coil and t is time. For a sinusoidally oscillation sample position, the voltage is based on the following equation: $V_{coil} = 2\pi fCmAsin(2\pi ft)$ where C is a coupling constant, m is the DC magnetic moment of the sample, A is the amplitude of oscillation and f is the frequency of oscillation. The sample is positioned at the vertical center of a gradiometer pick-up coil. VSM motor module use optical linear encoder signal obtained from VSM linear motor transport to control the position and amplitude of the oscillation in pick-up coil. The voltage induced in the pickup coil is amplified and lock-in. The VSM detection module detects the in-phase and quadrature phase signals from the encoder and the amplifier voltage from the pick-up coil. These signals are averaged and sent over CAN bus to the VSM application running on the PC. The schematic diagram of operating principle for the VSM is shown in figure 2.7.

VSM in this system has two options, VSM standard which can function from 1.8 K to 400 K and VSM oven that ranges from 300 K to 1000 K. In this work, the magnetic measurements M-H and M-T were done in the temperature range of 5K to 400 K and with the magnetic field range of ($\pm$ 20 kOe)

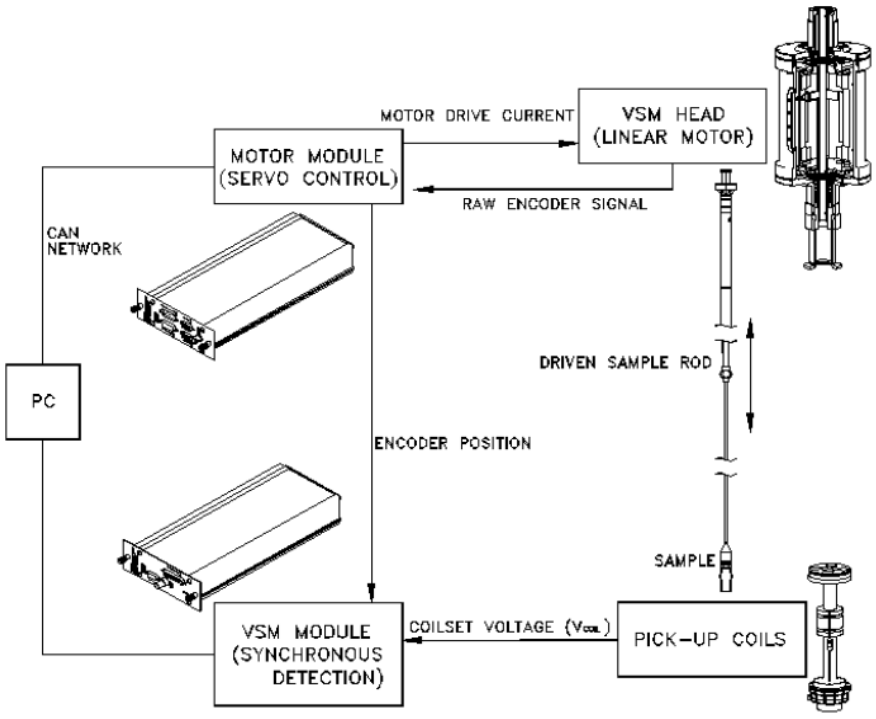

Figure 2.7: Schematic of operating principle for the VSM option

2.4.7 Ferroelectric Hysteresis Loop

Electric hysteresis loop of polarization P versus external electric field E is the most important characteristic of ferroelectric materials. Measurement of the hysteresis loops has generally been carried out using a modified Sawyer-tower circuit [25, 26, 27]. The polarization is related to the strain and since small currents are somewhat simpler to measure than small displacements the P-E loop can provide a means of investigating displacement behaviour. Indeed the charge can be used in a feedback loop to drive the piezoelectric with a non linear field to give a linear displacement [27]. The ferroelectric hysteresis loops (P-E

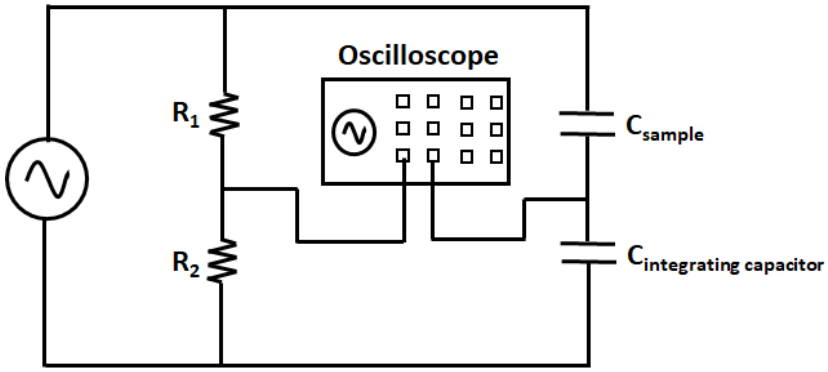

Figure 2.8: Schematic of the experimental setup to carry out ferroelectric measurement.

loops) of the materials in this study were measured using a ferroelectric tester (Radiant Technologies, Inc.). The set-up consists of a ferroelectric tester, an optical microscope, a probe station and control PC. A schematic of the experimental setup is shown in figure 2.8. Here the field applied across the sample is attenuated by a resistive divider, and the current is integrated into charge by virtue of a large capacitor in series with the sample. Both these voltages are then fed into the X and Y axes of an oscilloscope to generate the P-E loop. The applied voltage was usually a sinusoid at mains frequency as this was the simplest method to generate the required voltage and current.

2.4.8 Dielectric constant and loss tangent Study

Dielectric constant, also called relative permittivity (ϵ_r) is a measure of the amount of electric potential energy, in the form of induced polarization that is stored in a given volume of material under the action of an

electric field. ϵ_r indicates how easily a material can become polarized by imposition of an electric field on an insulator. It can be expressed as $\epsilon_r = \epsilon/\epsilon_o$ where ϵ, ϵ_o are absolute permittivity ($C^2/(N\ m^2)$) and permittivity of vacuum of free space ($8.854187817x10^{-12}\ C^2/(N\ m^2)$). The capacitance of a capacitor depends on the permittivity of the dielectric layer as well as the area (A) of the capacitor and the separation distance (d) between the two conductive plate, given by $C = \epsilon_r\ \epsilon_o(A/d)$.

The ϵ_r of a material depends upon the polarizability (electronic, atomic, and orientational) of the molecules. The electronic and atomic polarization occurs in non-polar molecules. In electronic polarization, the application of electric field causes a displacement of the electrons to the nucleus. However, in atomic polarization, displacement of the atomic nuclei relative to one another takes place. Orientational polarizability occurs in polar molecules in which the application of an electric field causes an orientation of dipoles.

The electronic polarization induced by the applied field is caused by displacement of the electrons within the atom, whereas the atomic polarization is caused by atoms within the molecules. Orientational polarization exists only in polar materials and its dispersion may lie within a wide frequency range (i.e. 10^2 - 10^{10} Hz), depending on the material and temperature. The electronic and atomic polarization may

persists frequency upto 10^{16} Hz and 10^{13} Hz respectively.

Dielectric loss peaks reflect internal motions, which involve the re-orientation of electric dipoles. The dielectric loss tangent (tan δ) of a material denotes a quantitative dissipation of the electrical energy due to different physical processes such as electrical conduction, dielectric relaxation, dielectric resonance and loss from non-linear processes. Origin of dielectric losses can also be considered as being related to delay between the electric field and the electric displacement vectors .The total dielectric loss is the sum of intrinsic and extrinsic losses. Intrinsic dielectric losses are the losses in the perfect crystals which depend on the crystal structure and can be described by the interaction of the phonon system with the ac electric field. Extrinsic losses are associated with imperfections in the crystal lattice such as impurities, microstructural defects, grain boundaries, porosity, microcracks, order–disorder, random crystallite orientation, dislocations, vacancies, dopant atoms etc. The extrinsic losses are caused by lattice defects and therefore can be in principle eliminated or reduced to the minimum by proper material processing [28]. Dielectric loss factor is expressed as the ratio of imaginary part of the dielectric constant to the real part.

$$tan\delta = \frac{\epsilon''}{\epsilon'} \tag{2.7}$$

From dielectric loss and dielectric permittivity, AC conductivity of materials can be evaluated using relations $\sigma_{AC} = 2\pi\epsilon_o\epsilon'$ f tanδ where f is the frequency of the applied field, ϵ_o is the permittivity of free space, ϵ' is the real part of relative permittivity of the samples, tan δ is the loss factor and σ_{AC} is an ac conductivity [29].

In this study, the dielectric study through capacitance measurement, loss tangent and impedance of the pellets and thin films were measured in an HP 4294A Impedance Analyzer. A cryostat with a programmable temperature controller (M/S MMR technology Inc. Model K-20) was used for the temperature dependent measurements.

2.4.9 Atomic Force Microscopy

Atomic force microscope (AFM) is a type of scanning probe microscope (SPM), which uses a fine probe to prove over a surface rather than use electrons or a beam of light. Since its invention in 1986, AFM has become the most widely used in surface, materials, and biological sciences [30].

Principle of AFM

The mechanism of the AFM is based on the detection of forces acting between a sharp probe (also called as AFM tip or sensor) and the surface of the sample. The tip is attached to very flexible can-

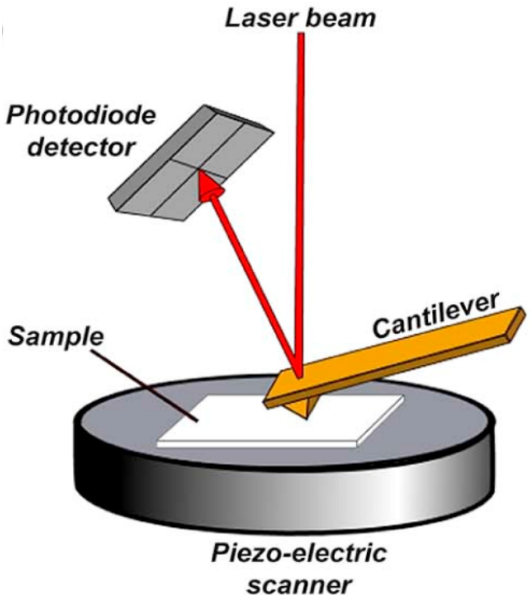

Figure 2.9: Schematic presentation of AFM

tilever. Laser beam is used to detect the cantilever motion. The light is reflected from cantilever onto the photo-diode, position-sensitive detectors. Photo-detector consisting of four-segments. The differences between the segments of photo-detector of signals indicate the position of the laser spot on the detector [31, 32].

The probe is a sharp tip of $\sim$ 3 - 6 μm tall pyramid with 15 - 40 nm end radius. Though the lateral resolution of AFM is low ($\sim$30 nm) due to the convolution, the vertical resolution can be up to 0.1 nm. The AFM probe interacts with the substrate through a raster scanning motion. The up/down and side to side motion of the AFM tip as it scans along the surface is monitored through a laser beam reflected off the cantilever. The schematic diagram is shown in figure 4.2.

2.4.10 Piezo Force Microscopy

Piezoresponse force microscopy (PFM) is a variant of atomic force microscopy (AFM) that allows imaging and manipulation of piezoelectric/ferroelectric materials domains.

The invention of voltage-modulted version of AFM, i.e. PFM has produced a wealth of new opportunities in ferroelectrics and other polar materials. It enables non-destructive visualization and control of FE nanodomains, as well as direct measurements of the local physical characteristics of ferroelectrics, such as nucleation bias, piezoelectric coefficients, disorder potential, energy dissipation, and domain wall (DW) dynamics [33].

Principle of PFM

PFM is based on the detection of local piezoelectric deformation in ferroelectric sample induced by an external electric field. The tip is brought into contact with the surface, and the piezoelectric response of the surface is detected as the first-harmonic component of bias-induced tip deflection $d = d_o + A\cos(\omega t + \phi)$, where ϕ is the phase that presents information on the polarization direction below the tip. For c^- domains (polarization vector pointing downward), the application of a positive tip bias results in the expansion of the sample and surface oscillations

are in phase with the tip voltage, hence $\phi = 0$. For c^+ domains, $\phi = 180°$. The amplitude A defines the local electromechanical response and depends on the geometry of the tip-surface system and material properties. An additional contribution to PFM contrast originates from long-range electrostatic tip-surface interactions [33, 34, 35].

The PFM technique is based on the converse piezoelectric effect, which is a linear coupling between the electrical and mechanical properties of a material. Since all ferroelectrics exhibit piezoelectricity, an electric field applied to a ferroelectric sample results in changes of its dimensions [36].

In this study, the AFM and PFM study was done using a Nano Scope V from Veeco. AFM films were imaged using contact mode imaging at room temperature.

Bibliography

[1] Jia Zhuang, Yan-Hua Chi, and Dong Wang. Preparation of different topography $nico_2o_4$ with surfactant by solid state reaction. *Journal of Inorganic Materials*, 1, 2007.

[2] Nikolay Kosinov, Jorge Gascon, Freek Kapteijn, and Emiel JM Hensen. Recent developments in zeolite membranes for gas separation. *Journal of Membrane Science*, 499:65–79, 2016.

[3] Chunli Bai and Minghua Liu. From chemistry to nanoscience: not just a matter of size. *Angewandte Chemie International Edition*, 52(10):2678–2683, 2013.

[4] DB Chrisey and GK Hubler. Pulsed laser deposition of thin films, john wiley & sons. *New York*, 1994.

[5] S Anil, J Venkatesan, MS Shim, EP Chalisserry, and S-K Kim. Bone response to calcium phosphate coatings for dental implants. In *Bone Response to Dental Implant Materials*, pages 65–88. Elsevier, 2017.

[6] PR Willmott and JR Huber. Pulsed laser vaporization and deposition. *Reviews of Modern Physics*, 72(1):315, 2000.

[7] CM Garner, D Herr, and C Krautschik. International technology roadmap for semiconductors, 2007 edition, directed self-assembly requirements for sub 20 nm lithography (supplement), 2007.

[8] Ofer Sneh, Robert B Clark-Phelps, Ana R Londergan, Jereld Winkler, and Thomas E Seidel. Thin film atomic layer deposition equipment for semiconductor processing. *Thin solid films*, 402(1-2):248–261, 2002.

[9] Steven M George. Atomic layer deposition: an overview. *Chemical reviews*, 110(1):111–131, 2010.

[10] Markku Leskelä and Mikko Ritala. Atomic layer deposition chemistry: recent developments and future challenges. *Angewandte Chemie International Edition*, 42(45):5548–5554, 2003.

[11] HB Profijt, SE Potts, MCM Van de Sanden, and WMM Kessels. Plasma-assisted atomic layer deposition: basics, opportunities, and challenges. *Journal of Vacuum Science & Technology A: Vacuum, Surfaces, and Films*, 29(5):050801, 2011.

[12] SV Borisov and NV Podberezskaya. X-ray diffraction analysis: A brief history and achievements of the first century. *Journal of Structural Chemistry*, 53(1), 2012.

[13] William Lawrence Bragg. The structure of some crystals as indicated by their diffraction of x-rays. *Proceedings of the Royal Society of London. Series A, Containing papers of a mathematical and physical character*, 89(610):248–277, 1913.

[14] William Lawrence Bragg, David C Phillips, Henry Lipson, et al. *development of X-ray analysis*. G. Bell, 1975.

[15] John R Ferraro. *Introductory raman spectroscopy*. Elsevier, 2003.

[16] Ewen Smith and Geoffrey Dent. Modern raman spectroscopy: a practical approach. 2005.

[17] Goerg H Michler. Scanning electron microscopy (sem), 2008.

[18] Joseph I Goldstein, Dale E Newbury, Joseph R Michael, Nicholas WM Ritchie, John Henry J Scott, and David C Joy. *Scanning electron microscopy and X-ray microanalysis*. Springer, 2017.

[19] Ludwig Reimer. Scanning electron microscopy: physics of image formation and microanalysis, 2000.

[20] E Fernandez-Segura and Alice Warley. Electron probe x-ray microanalysis for the study of cell physiology. *Methods in cell biology*, 88:19–43, 2008.

[21] Don A Samuelson. Energy dispersive x-ray microanalysis. In *Free radical and antioxidant protocols*, pages 413–424. Springer, 1998.

[22] A John Morgan, Carole Winters, and Stephen Stürzenbaum. X-ray microanalysis techniques. In *Electron microscopy methods and protocols*, pages 245–276. Springer, 1999.

[23] PG Zambonin and E Desimoni. X-ray photoelectron spectroscopy: principles, instrumentation, data processing and molten salt applications. In *Molten Salt Chemistry*, pages 425–445. Springer, 1987.

[24] Grzegorz Greczynski and Lars Hultman. X-ray photoelectron spectroscopy: Towards reliable binding energy referencing. *Progress in Materials Science*, 107:100591, 2020.

[25] Charles Baldwin Sawyer and CH Tower. Rochelle salt as a dielectric. *Physical review*, 35(3):269, 1930.

[26] MM Berkens and Th Kwaaitaal. Spontaneous polarisation and transition temperature of a ferroelectric measured by a simple and accurate method. *Journal of Physics E: Scientific Instruments*, 16(6):516, 1983.

[27] AM Glazer, P Groves, and DT Smith. Automatic sampling circuit for ferroelectric hysteresis loops. *Journal of Physics E: Scientific Instruments*, 17(2):95, 1984.

[28] MT Sebastian, MAS Silva, and ASB Sombra. Measurement of microwave dielectric properties and factors affecting them. *Microw. Mater. Appl. 2V Set, John Wiley & Sons, Ltd, Chichester, UK*, page 1e51, 2017.

[29] MA El Hiti. Dielectric behavior and ac electrical conductivity of zn-substituted ni mg ferrites. *Journal of magnetism and magnetic materials*, 164(1-2):187–196, 1996.

[30] ADL Humphris, MJ Miles, and JK Hobbs. A mechanical microscope: High-speed atomic force microscopy. *Applied physics letters*, 86(3):034106, 2005.

[31] Surena Vahabi, Bahareh Nazemi Salman, and Anahita Javanmard. Atomic force microscopy application in biological research: a review study. *Iranian journal of medical sciences*, 38(2):76, 2013.

[32] Uroš Maver, Tomaž Velnar, Miran Gaberščček, Odon Planinšek, and Matjaž Finšgar. Recent progressive use of atomic force microscopy in biomedical applications. *TrAC Trends in Analytical Chemistry*, 80:96–111, 2016.

[33] Alexei Gruverman, Marin Alexe, and Dennis Meier. Piezoresponse force microscopy and nanoferroic phenomena. *Nature communications*, 10(1):1–9, 2019.

[34] Sergei V Kalinin and Dawn A Bonnell. Imaging mechanism of piezoresponse force microscopy of ferroelectric surfaces. *Physical Review B*, 65(12):125408, 2002.

[35] K Franke, H Huelz, and M Weihnacht. How to extract spontaneous polarization information from experimental data in electric force microscopy. *Surface science*, 415(1-2):178–182, 1998.

[36] Marin Alexe and Alexei Gruverman. *Nanoscale characterisation of ferroelectric materials: scanning probe microscopy approach*. Springer Science & Business Media, 2004.

Chapter 3

Study on Structural, electronic, magnetic and spin-phonon coupling on $Ga_{2-x}(Fe_{1-y}Mn_y)_xO_3$, $0 \leq y \leq 0.02$ and $1 \leq x \leq 1.4$ ceramics

3.1 Introduction

Multiferroic materials that simultaneously exhibit ferroelectric and ferromagnetic orderings with strong magnetoelectric (ME) coupling have been excessively studied in last few decades due to their potential application in several devices such as memory, multi-stage data storage, high-frequency filters and sensor applications [1, 2, 3, 4, 5, 6, 7]. Obtaining strong ME effects in single phase multiferroic materials at room temperature, understanding its origin and manipulating the processing and composition to obtain enhanced physical properties constitute the holy grail of multiferroic research. Due to the natural incompatibility between ferroelectricity and magnetism, only a few single-phase multi-

ferroic oxides are available. Until now, these materials were not envisioned for devices due to their low ME coupling at room temperature. Recently Intel research group has designed magnetoelectric spin-orbit logic device utilizing a single-phase material (La-doped $BiFeO_3$) which has higher switching energy (10 to 30 times), lower switching voltage (5 times) and higher logic density (by a factor of 5) than the present CMOS devices [8]. But La-doped $BiFeO_3$ is still not optimal, due to its high leakage current and small ME coupling coefficient. The new material approach for the realization of room-temperature strong ME coupling is very promising and potentially capable of enabling a wide range of ME devices are still awaiting a suitable material. Many of researchers focus on developing new material with significant magnetoelectric (ME) coupling above RT. While, in some known materials, these conditions can be achieved by engineering their properties and transition temperature via controlled compositional modulation and lattice strains. On this respect, gallium ferrite ($GaFeO_3$ or GFO), is an exciting magnetoelectric (ME) compound owning RT piezoelectric [4] and a near RT antiferromagnetic [9, 10]. The flexibility of optimizing transition temperature (Tc) as desired by varying Fe concentration or/and by modifying the synthesis technique is the interesting aspect of this compound.

After the synthesis of single crystal $Ga_{2-x}Fe_xO_3$ ($0.7 < x < 1.4$) by Remeika [11] in late 1960, this compound has been of research interest due to its robust optical ME effect [12], linear ME effect as a function of Fe contents [9], and magnetization induced second harmonic generation [13]. Due to isovalent and close ionic radii of Fe^{3+}(0.645 Å) and Ga^{3+}(0.624 Å), cations can lead to a site-disorder between Fe/Ga positions [14] which is suggested to be a primary source of net magnetic moment in GFO [15, 16]. The sum of occupancy of Fe cation at the Fe2 and Ga2 sites is larger than the Fe composition on Fe1 site leading to its Ferrimagnetic behavior with easy magnetization axis is reported to be along c-axis [9]. Sun *et al.* [17] have shown the coupling between polarization and magnetization of the compound and found the existence of a linear relation between dielectric constant and square of magnetization. Additionally, magnetism in GFO is manifested in a number of interesting phenomena such as magnetoelectric effect [9] magnetization induced second harmonic generation [18], optical magnetoelectric effect [12, 19], and magneto-structural coupling [20, 21] etc. Observation of large ferroelectric value recently reported by Song *et al.*, [22] had made the compound much exciting. This value is higher than previously predicted by Stoeffler [23] [21], however smaller than theoretical calculation done on the basis of first principle by Roy *et al.* [21].

GFO is an orthorhombic crystal structure with space group $Pc2_1n$ with the lattice parameters a = 8.7413 Å, b = 9.38955 Å, and c = 5.08044 Å in bulk GFO [23]. One GFO unit cell contains eight formula units with two types of cations Ga^{3+} and Fe^{3+}, generally represented as Ga1, Ga2, Fe1 and Fe2, where the Ga1 site tetragonal and others are octahedrally surrounded by oxygen [9, 24]. Fe concentration plays a significant role in the magnetic properties and transition temperature. The low-temperature magnetic transition temperature (i.e., 220 K) of $Ga_{2-x}Fe_xO_3$ for x = 0.8 raises to 340 K when the x value increases to 1.4. Thus, with appropriate modification in composition and processing conditions of the samples, the transition temperature can be raised beyond RT [9, 25], directing the material toward a prospective RT magnetoelectric.

This chapter is assigned to the study of synthesis, structural and electric and magnetic characteristic study of solid state ceramic of gallium ferrite and its derivatives (Mn-doped gallium ferrite). First, the synthesis process of powder and subsequent target of $Ga_{2-x}(Fe_{1-y}Mn_y)O_3$ is discussed, followed by the structural characterization with X-ray diffraction, scanning electron microscopy, electron dispersive spectroscopy, and Raman spectroscopy. Finally, measurements of magnetic and electric properties are elaborated.

3.2 Ceramic preparation

Polycrystalline $Ga_{2-x}(Fe_{1-y}Mn_y)_xO_3$, $0 \leq y \leq 0.02$ and $1 \leq x \leq 1.4$ powder samples were synthesized by high-temperature solid-state reaction method from a stoichiometric mixture of oxides of gallium (Ga_2O_3), iron (Fe_2O_3), and manganese (Mn_2O_3) with purity higher than 99.8% (all from Alfa Aesar Co). These ingredients were first spun via magnetic spinner in acetone environment in a beaker for whole night at 80°C. It was then mixed thoroughly using a mortar and pestle for 2 hours in acetone medium and brought it to dry. The powders were then calcined at an optimized temperature of 1300°C ($x \leq 1.2$) and at 1320°C ($1.2 \leq x \leq 1.4$) for 10 hours in air using a Carbolite HTF1700 furnace with a heating and cooling rate of 5 °C/min. The calcined powder was further grinded to obtain fine mixture and sieved through a 150 μm mesh. Poly vinyl alcohol (1%) was added on the fine calcined powder as a binder to prepare pellets of 13 mm diameter and the target diameter of 1 inch. Hydrostatic press was used to shape these ceramics with the pressure of 6 tons for 2 mins. The pressed ceramics were sintered at 1350°C and 1370°C respectively for 5 hours in air. The study on these prepared compounds is carried out in two groups; the $GaFeO_3$ group, written as GFOn (here, y=0); and the Mn-doped $GaFeO_3$ group written as GFMOn (here, y= 0.02), where n=1, 2 and 3. Here, n=1,

2 and 3 represents the variation in Fe content i.e. (x=1.0, 1.2 and 1.4 respectively). It can be further clarified from table 3.1 where symbols used for specific compounds are shown.

Table 3.1: Compounds with their representation

Symbol	Compound	Symbol	Compound
GFO1	$GaFeO_3$	GFMO1	$GaFe_{0.98}Mn_{0.02}O_3$
GFO2	$Ga_{0.8}Fe_{1.2}O_3$	GFMO2	$Ga_{0.8}(Fe_{0.98}Mn_{0.02})_{1.2}O_3$
GFO3	$Ga_{0.6}Fe_{1.4}O_3$	GFMO3	$Ga_{0.6}(Fe_{0.98}Mn_{0.02})_{1.4}O_3$

3.3 Results and Discussions

3.3.1 X-Ray diffraction pattern

The phase purity and crystal structure of the ceramics were characterize by using XRD patterns. Rietveld analysis were performed on room temperature XRD pattern for the detail analysis of the phase and unit cell parameters using Fullproof suite. The reflection peak position is initially inspected with JCPDF file prior to carry out the refinement. The well peak match with the JCPDF file #761005 suggests the orthorhombic phase formation belonging to space group $Pna2_1(C^9_{2v})$. The Rietveld refinements of X-ray diffraction (XRD) data collected at room temperature for $Ga_{2-x}(Fe_{1-y}Mn_y)_xO_3$ are shown in figure 3.1. In the samples, no secondary peaks in the diffraction pattern were found until $x \leq 1.2$ showing single phase GFO. For $x > 1.2$, some secondary peaks usu-

ally from α-Fe_2O_3 were seen (JCPDF file #1309-37-1). For refinement, phase identification is done with Ẋpert Highscore plus software [26] considering a CIF file with COD #1008838. A smooth background was constructed by considering the linear interpolation of selected points and the diffraction peaks were modeled using the pseudo-Voigt function. A pseudo-Voigt function was used for profile simulation after selecting an appropriate number of background points. To begin with, the refinements were carried out for scale factor, lattice parameters and profile width parameters. Thereafter, the position coordinate and isotropic thermal parameters were refined. The refined lattice parameter and unit cell volume of all samples are listed in table 4.1. The goodness of fit (γ^2) value is somehow higher in some refinement. But the positive, negative, and positive value of FWHM parameters (U, V, and W) imply the acceptance value of the above parameters. We have observed an increase in lattice parameters on increasing Fe and Mn contents, shown in figure 3.1 suggesting that the compound follows well Vegard's law [27]. On the other hand, with Mn doping, the lattice parameters and volume are slightly reduced with respect to the parent compound (for n=1 and 2). The decrease in lattice parameter in case of GFO1-GFMO1 and GFO2-GFMO2 can be explained due to the smaller radius of Mn^{3+} that replaces Fe^{3+}. However, lattice pa-

rameter is increased in case of GFO3-GFMO3 (i.e. for n=3) due to the competing tendency of Mn^{3+} ions for the site occupation. Much of Mn^{3+} (0.64 Å) substitute at Fe^{3+} (0.645 Å) octahedral site, but some portions occupy Ga^{3+} (0.624 Å) octahedral site due to their close ionic radii. Ramana *et al.* [28] reported the similar behavior of decreasing lattice size on Mn substituted Cobalt Ferrite. Electronic interaction caused by strongly changing microstructure might also be responsible for this type of behavior.

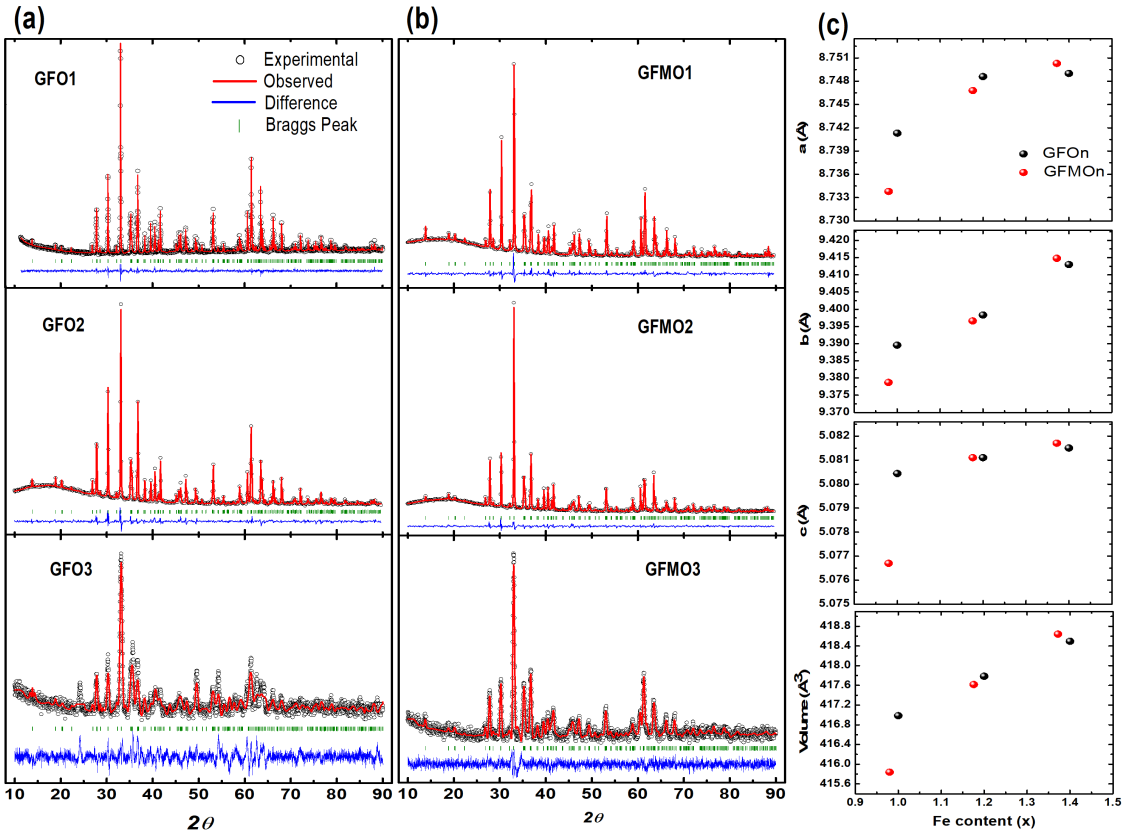

Figure 3.1: Rietveld Analysis of (a) GFOn and (b) GFMOn (n=1,2,3), (c) Lattice parameters and unit cell volume of GFOn and GFMOn with respect to Fe contents.

Further analysis of refined structural parameters of GFO1 is carried

out with VESTA software. Bond lengths and bond angles of the tetrahedral and octahedral polyhedral units of GFO1 is derived through this software. The crystal structure along c-axis is shown figure 3.2(a) that clearly marks the position of Ga and Fe. Ga1 is tetrahedral coordinated with oxygen ions whereas Ga2, Fe1, and Fe2 are octahedrally coordinated with oxygen ions. From the ionic position, the bond length and bond angle of cations with neighboring oxygen ions have been obtained, shown in figure 3.2(b). The average bond lengths for Ga1-O, Ga2-O, Fe1-O, and Fe2-O ions were obtained as 1.9321 Å, 2.0195 Å, 2.103 Å, and 2.1976 Å respectively. These results are in fair agreement with the previous theoretical calculated values [21] and neutron diffraction results [9]

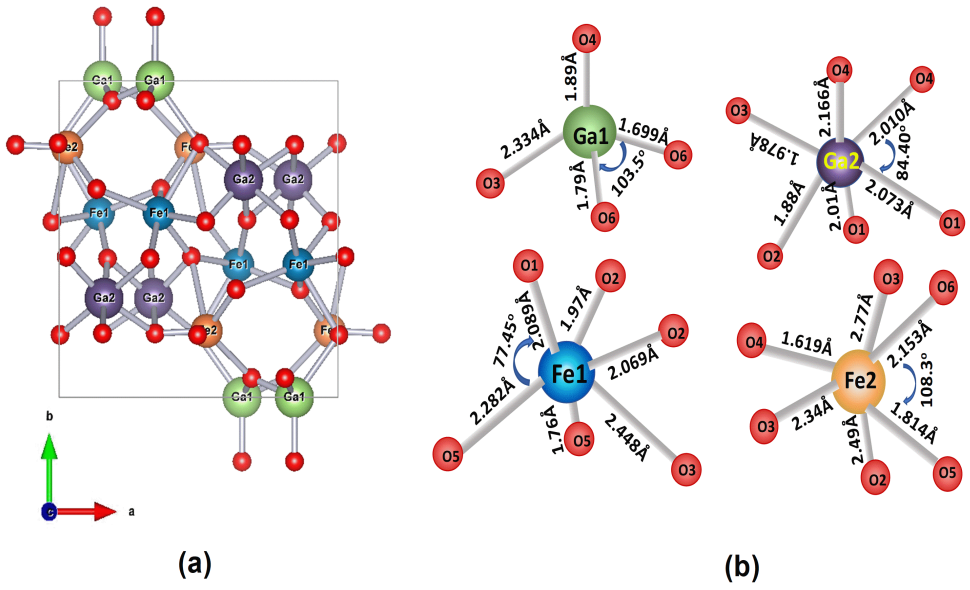

Figure 3.2: (a) Schematic crystal structure of GFO along the c-axis (b) schematic of cations–oxygen bond lengths and bond angles simulated using the VESTA program.

3.3.2 Scanning Electron Microscopic Studies:

SEM studies were carried out to check the granular structure and microscopic properties of elements in the sample, both at large surface area and at a single grain area. Surface micrographs of $Ga_{2-x}(Fe_{1-y}Mn_y)_xO_3$, shown in figure 3.3 illustrated a well sintered granular structure with almost uniformly distributed grains. The final average grain size obtained are $\sim$ 2-8 μm. The larger grain sizes are seen in GFOn/GFMOn for n=3 (i.e. for x=1.4), as a consequences of higher sintering temperature. It can be seen in the SEM image that the pores are decreasing with an increase in Fe and Mn composition. Figure 3.4(a) is the elemental mapping of GFO1, scanned for large surface area. It is clear that, all elements (Ga, Fe, O) are distributed uniformly over all area. To check the distribution pattern at microscopic area, elemental mapping is done further at single grain size, as shown in figure 3.4(b). Elements are well distributed across small size as well.

Elemental mapping is done for GFO3 and GFMO3 samples (not shown here). Absence of clustering of Mn and Fe in the SEM images within the resolution limit indicates that the observed physical properties are of intrinsic properties of the materials. Hence it can be concluded that the magnetic properties observed in GFO are not due to the secondary phases or clustering of Fe.

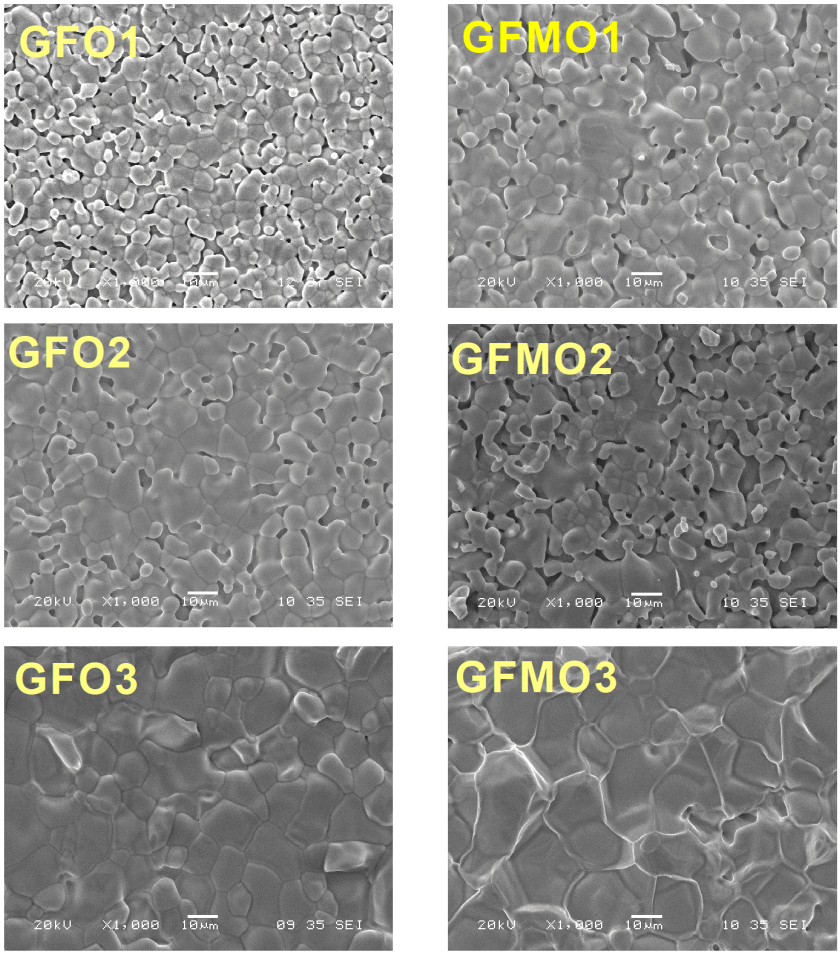

Figure 3.3: SEM images of all samples

Presence of all cationic elements were further confirmed by EDX spectrum. Figure 3.5 is the EDX spectrum recorded from the sample indicating the presence of elemental compositions (Ga, Fe, and O ions) at their respective characteristic X-ray emission lines (O(kα) 0.5249keV, Ga(kα) 9.251keV, Ga(kβ) 10.2642 keV, Ga(lα) 1.0979 keV, Fe (kα) 6.4038 keV, Fe(kβ) 7.0579 keV, and Fe(lα) 0.7056keV).

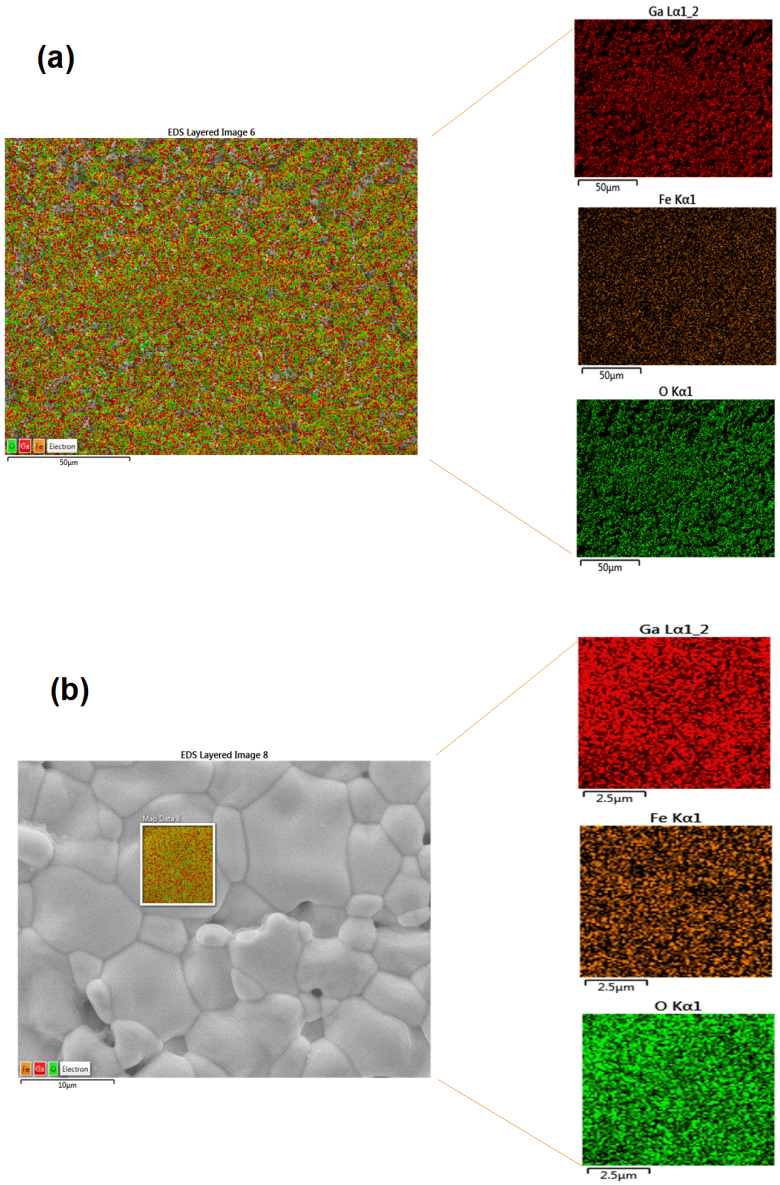

Figure 3.4: Elemental mapping of GFO1

3.3.3 Raman Study

For a better understanding of the structural changes upon composition variation, we studied Raman spectra of all samples at RT. Fig. 3.6 shows the RT Raman spectra of all compositions in which 17 promi-

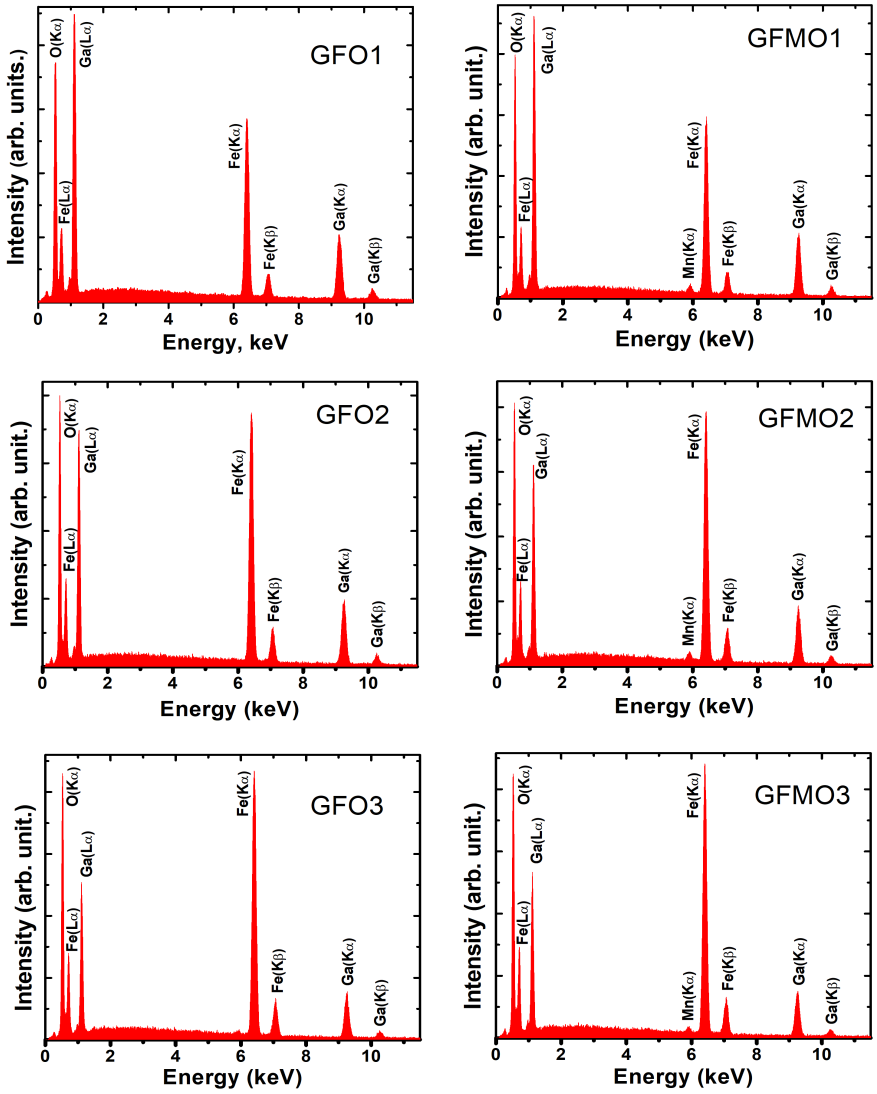

Figure 3.5: EDX spectrum of GFO ceramics

nent Raman modes are shown in the spectral range of 80-860 cm-1. Theoretically, the RT orthorhombic phase of GFO consists of 117 Raman active phonons from a group theoretical analysis of phonon modes from C_{2v} factor group distributed as Γ_{opt} = 29A1 + 30A2 + 29B1 + 29B2. Reduced number of modes for pure GFO was reported in earlier studies as well [29, 30]. The number of Raman modes doesn′t change upon increasing Fe and Mn contents. It is noticed that the number of observed Raman modes remain the same upon increasing the Fe contents and after doping the Mn contents suggesting that there is no phase change due to the incorporation of Fe and Mn. It can be seen in both graphs of Fig. 3.6 that the position of most prominent modes move towards lower frequency as Fe content increases indicating that the modes soften with excess Fe concentration.

The relative intensities of the modes corresponding to 357, 430 ,689 cm^{-1} tend to decrease with respect to their nearest counterparts, i.e. the modes corresponding to 391, 459, and 743 cm^{-1}, with increasing Fe concentration. This indicates that the vibrations corresponding to 357, 430 ,689 cm^{-1} modes are due to Ga1-O bonding. This could be explained in the way, as Fe content is increasing, the population of Ga1 is reduced, lowering the spectral intensity. Similar behavior is observed by Mukherjee *et al.* [25]. Detail analysis of temperature

Table 3.2: Lattice parameters of all compounds determined by Reitveld refinement

	GFO1	GFMO1	GFO2	GFMO2	GFO3	GFMO3
a	8.7413	8.7338	8.7486	8.7468	8.7490	8.7503
b	9.38955	9.3787	9.3983	9.3966	9.413	9.4148
c	5.08044	5.0767	5.0811	5.0811	5.0815	5.0817
V	416.985	415.8380	417.7845	417.6168	418.494	418.6397
a*	0.114399	0.114498	0.114304	0.114328	0.114298	0.114282
b*	0.106501	0.106624	0.106402	0.106421	0.106236	0.106216
c*	0.196833	0.196980	0.196806	0.196807	0.1967922	0.196785
V*	0.0023982	0.002405	0.002393	0.002394	0.0023895	0.002389
γ^2	2.06	4.76	4.44	3.56	2.59	1.503
R_p	1.55	1.37	1.25	1.3	2.18	1.69
R_{wp}	2.1	2.05	1.81	1.75	2.84	2.19
R_e	1.46	0.942	0.851	0.875	1.76	1.79
U	0.02249	0.00222	0.00211	0.00460	0.20212	0.13631
V	-0.02991	-0.00658	-0.00100	-0.00362	-0.00510	-0.00762
W	0.01344	0.00535	0.00625	0.00704	0.02764	0.15451

dependent Raman spectra for pure $GaFeO_3$ (GFO1) is presented in another session.

In Mn-inclusive (GFMOn) Raman spectra, the relative intensity is decreasing with an increase in Fe contents; however, the decreasing rate is not as significant as in GFOn. Additionally, we see a shift in phonon modes at around 600 cm^{-1} in GFMOn. It could be attributed to stretching and bending of MnO6 octahedral in $RMnO_3$ perovskite, indicating that Mn is occupying Fe site only [31]. The modes in the vicinity of 600 - 620 cm^{-1} are varying in Mn-doped samples, which might be due to the change of Fe-O bonds induced by Mn^{+2} ions [32].

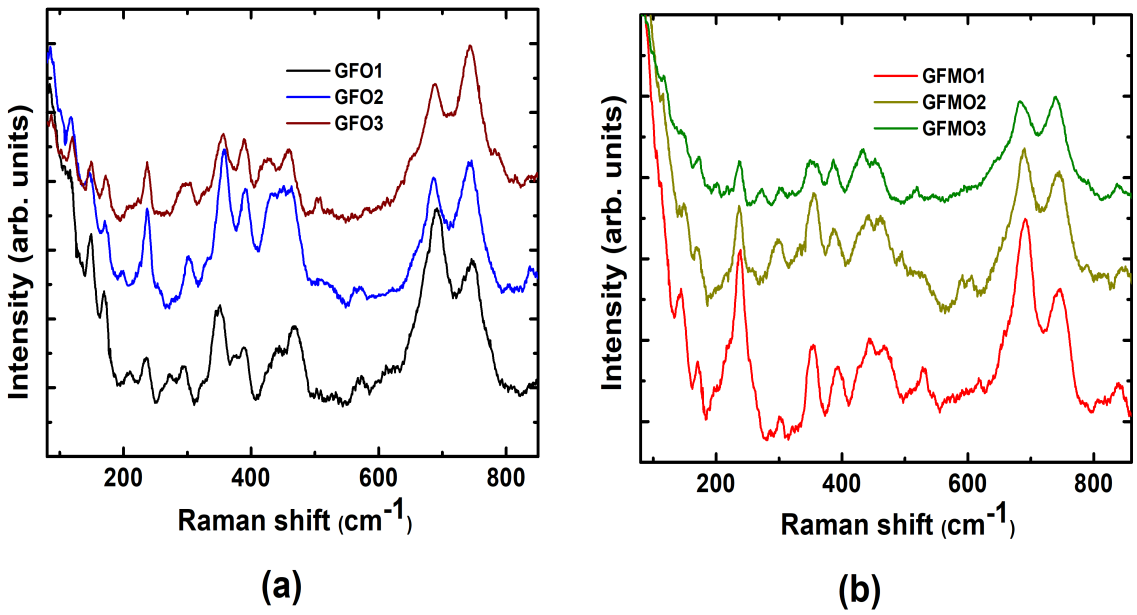

Figure 3.6: Raman spectra of GFOn and GFMOn at RT.

3.3.4 Magnetic Properties

To observe the existence of magnetic ordering in $Ga_{2-x}(Fe_{1-y}Mn_y)_xO_3$, dc-magnetization measurements have been carried out as a function of temperature M(T) and as a function of magnetic field M(H). Both M(T) and M(H) measurements were carried out in the in-plane (magnetic field parallel to the sample's surface) configuration with external static magnetic field of 100, and 1000 Oe, respectively in a wide temperature range of 5 - 395 K. The M(T) measurements were recorded at two different conditions: zero-field-cooled (ZFC) and field-cooled (FC). Figure 3.7 shows the temperature dependence of magnetization of all samples under field-cooled (FC) and zero-field-cooled (ZFC) conditions

at the static magnetic field of 1000 Oe. Upon warming, magnetization decreases slowly at the beginning and then decreases sharply, after specific temperature, magnetization vanishes indicating the samples have undergone to paramagnetic state. All samples show thermomagnetic irreversibility. The observed bifurcation of the ZFC and FC magnetization curves in these compounds possibly arises from ineffective Fe ions as mentioned by Wang *et al.* [33] and/or the frustrated behavior due to the geometrical arrangement of the Fe1, Fe2, and Ga2 in corner sharing tetrahedral positions as described previously by Mukherjee et al [20]. It can be seen from Fig.3.7 that all samples have undergone a ferrimagnetic-paramagnetic transition, and the T_C increases with the increase of Fe content. Addition of Mn lowers T_C value slightly than parent GFO compound. The decrease of T_C on adding Mn might be due to the reduction in Fe-O interaction. On adding Mn, different interaction is possible in the system such as Fe^{3+}-O^{2-}-Fe^{3+}, Mn^{3+}-O^{2-}-Mn^{3+} and Fe^{3+}-O^{2-}-Mn^{3+} super-exchanges. Of these, the Fe^{3+}-O^{2-}-Fe^{3+}, Mn^{3+}-O^{2-}-Mn^{3+} are strong antiferromagnetic [34, 35] where as, Fe^{3+}-O^{2-}-Mn^{3+}interaction could be both ferromagnetic or antiferromagnetic [36]. Thus, the addition of Mn would lead to decrease Fe - Fe linkage that could decrease T_C, which is seen in our case between GFOn and GFMOn for n=1 and 2. However, for higher Fe content,

T_C value doesn't lower with Mn addition (as in the case of GFO3 and GFMO3). It could be because, at this condition (n=3), Fe-O-Fe interaction is dominating against Fe-O-Mn interaction due to the higher concentration of Fe. T_C value for pure GFO (GFO1) is found to be at 220 K, which increased to 340 K on increasing Fe content (GFO3). Magnetic field dependence of magnetization (M-H) was also carried out at different temperature (5 - 400K) is shown in figure 3.8. Gradual increase of remanent magnetization (M_R)and coercive field (H_C) with a decrease in temperature is seen for all samples, which is the typical signature of ferrites. The wider hysteresis of GFO loop figure 3.8(a) became narrower with increasing Fe and Mn composition figure 3.8(f). The M_R and H_C for GFO1 (pure GFO) are obtained as 10.08 emu/g and 7.792 kOe at 5K. M_R value increased to 16.82 emu/g whereas H_C value decreased to 1.95 kOe for GFMO3. Table 3.3 shows the M_R and H_C values for all compositions at different temperature.

T (K)	GFO1		GFMO1		GFO2		GFMO2		GFO3		GFMO3	
	M_R emu/g	H_C kOe	M_R emu/g	H_C kOe	M_R emu/g	H_C kOe	M_R emu/g	H_C kOe	M_R emu/g	H_C kOe	M_R emu/g	H_C kOe
5	10.08	7.792	9.26	4.626	17.159	5.937	14.189	4.520	12.49	6.24	18.79	4.105
50	9.08	6.610	8.58	3.579	16.20	5.66	13.393	4.342	11.83	5.909	17.96	4.024
100	7.766	5.725	6.93	3.126	14.577	5.623	11.890	4.281	10.669	5.751	16.32	4.006
150	6.206	3.688	4.8	1.384	12.49	5.209	9.958	3.972	9.354	5.398	14.53	3.956
200	2.10	0.154	0.147	1.017	10.13	4.302	7.918	3.246	8.115	4.793	12.780	3.677
250			0.024	0.007	7.04	2.328	4.967	1.124	6.648	3.300	10.74	2.983
300						0.024	0.297	0.037	2.28	0.109	6.73	1.448
350									0.070	0.373	0.21	0.01
400									0.070	0.566	0.027	0.007

Table 3.3: Remanent magnetization (M_R) and coercive field (H_C) of GFOn and GFMOn at temeprature range (5-400 K)

Precise analysis of M-H measurement is carried out. 3.9(a,b) shows

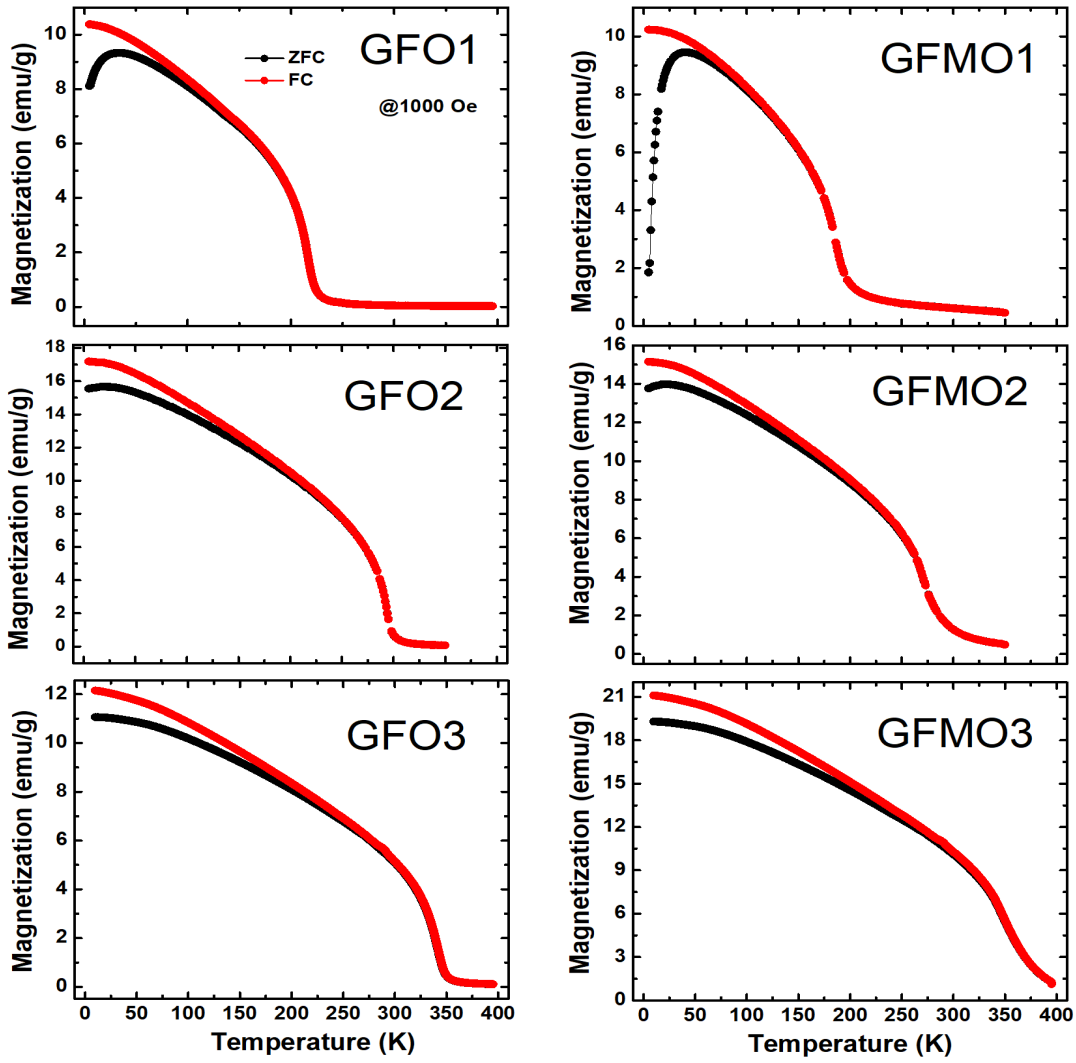

Figure 3.7: Magnetization vs temperature of $Ga_{2-x}(Fe_{1-y}Mn_y)_xO_3$ shows the transition temperature higher than RT for x $\leq$ 1.4.

the magnetic field dependence of magnetization (M-H) measurements of GFOn and GFMOn at 300 K. GFO3 possess low magnetization, whereas GFO2 and GFO1 are paramagnetic at RT as shown in Fig. 3.9(a).

The magnetization of GFMO3 is significantly higher than GFO3,

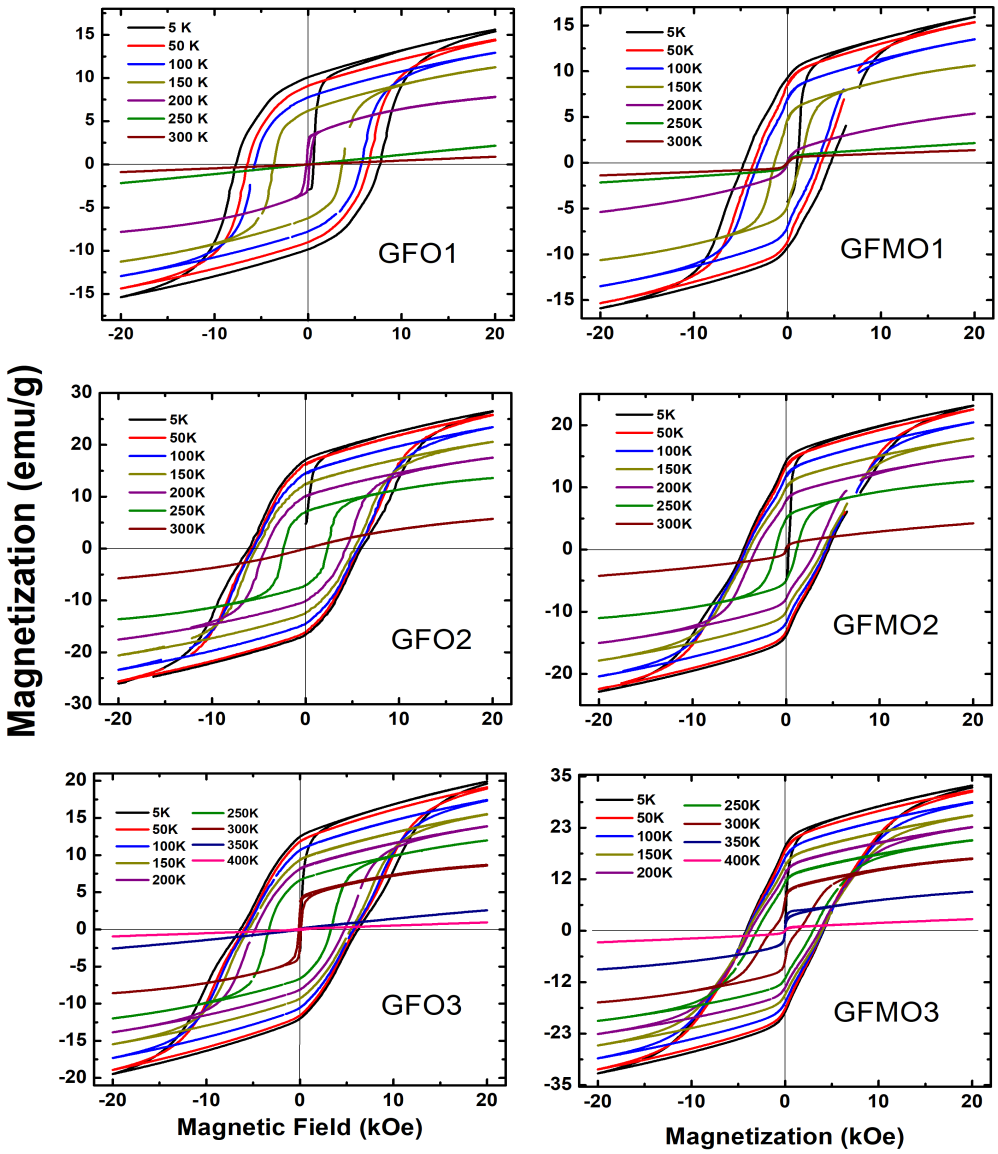

Figure 3.8: Magnetization versus magnetic field measured at various temperature (5K - 400K)

which can be seen in Fig. 3.9(a)(b), whereas GFMO1 and GFMO2 show paramagnetic behavior at RT. On increasing Fe contents, the magnetization of the compound increases. However, we observed that GFO3 exhibits lower magnetization than GFO2 below 250 K despite higher Fe content. The magnetization behavior of GFOn at 100K, shown in an inset in Fig. 3.9(a) depicts this behavior. This might be due to the presence of a significant amount of isolated Fe dopants in GFO3 which exhibits paramagnetic behavior at low temperature. Similar type of observations has been reported by Ray and Chakraborty et al. [37, 38]. At room temperature, we observed a systematic increase of magnetization with an increase of Fe contents. The inset of Fig. 3.9(a)(b) is the magnetization of GFMOn at 100 K. It is seen that Mn-doped GFO shows better magnetization with the lower coercive field. We observed a linear increase in transition temperature with increasing Fe contents. Additionally, the rate of increasing T_C was found to be higher in Mn-doped GFO, as shown in Fig. 3.9(c). Fig. 3.9(d) depicts the coercivity (H_C) of GFOn and GFMOn at 100K. H_C of GFMOn is observed to be lower than GFOn, i.e. H_C decreases on Mn addition, which is similar to the earlier report [36]. This indicates Fe is being replaced by Mn. Such type of behavior is also found in Mn-substituted $CoFe_2O_4$ [28]. On increasing Fe contents, Magnetization (M_R) of the

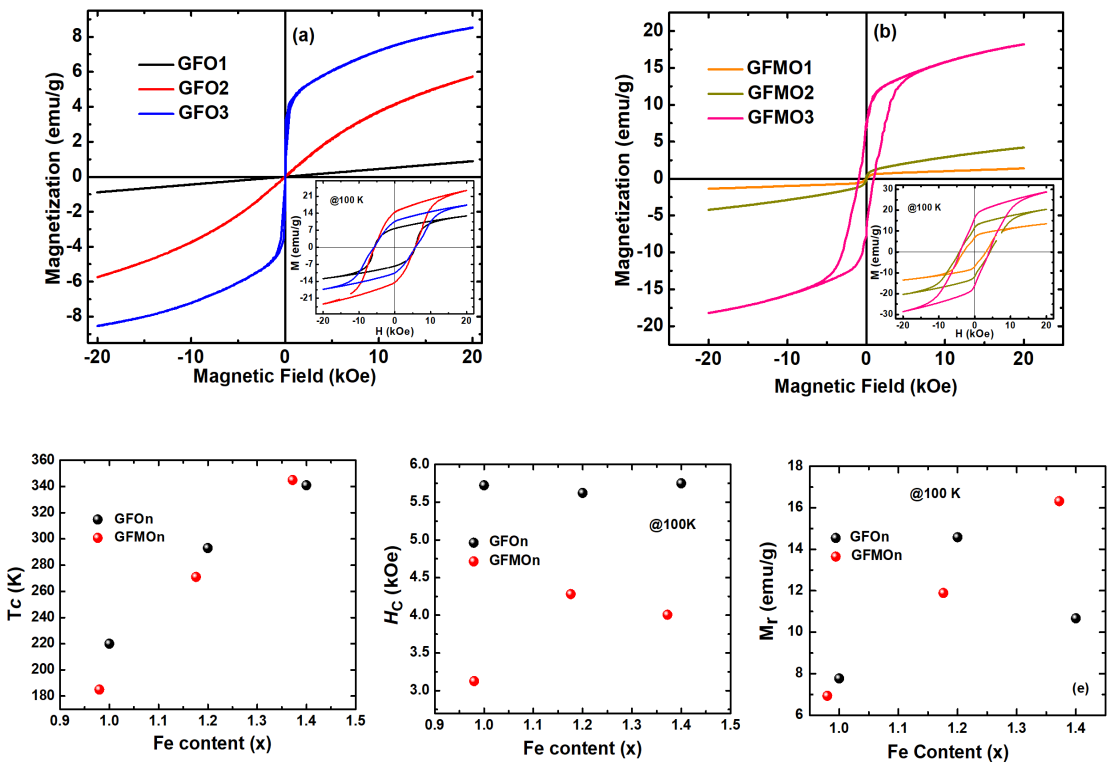

Figure 3.9: (a) Magnetization vs magnetic field of GFOn at RT. Inset of (a) shows the magnetization hysteres of GFOn at 100 K. (b) magnetization vs field of samples GFMOn at RT. Inset of (b) is the magnetization hysteresis loops of GFMOn at 100 K. (c) transition temperature (d) Coercive field and (e) remanant magnetization of GFOn and GFMOn w.r.t. Fe content.

compound increases (Fig. 3.9(e)). This property with higher M_R and lower H_C on adding Mn indicates the advantage of doping Mn on GFO.

3.3.5 XPS Study

Net magnetic moment in GFO is usually due to the contribution of extra Fe atoms occupying at Ga2 sites pointing at the same direction [9]. On magnetic study, we have observed the increase of remanant

magnetization and decreasing of coercive field with increasing Fe and Mn content. This is an exciting result that the investigators would like to achieve as such properties possess great potentiality in device application.

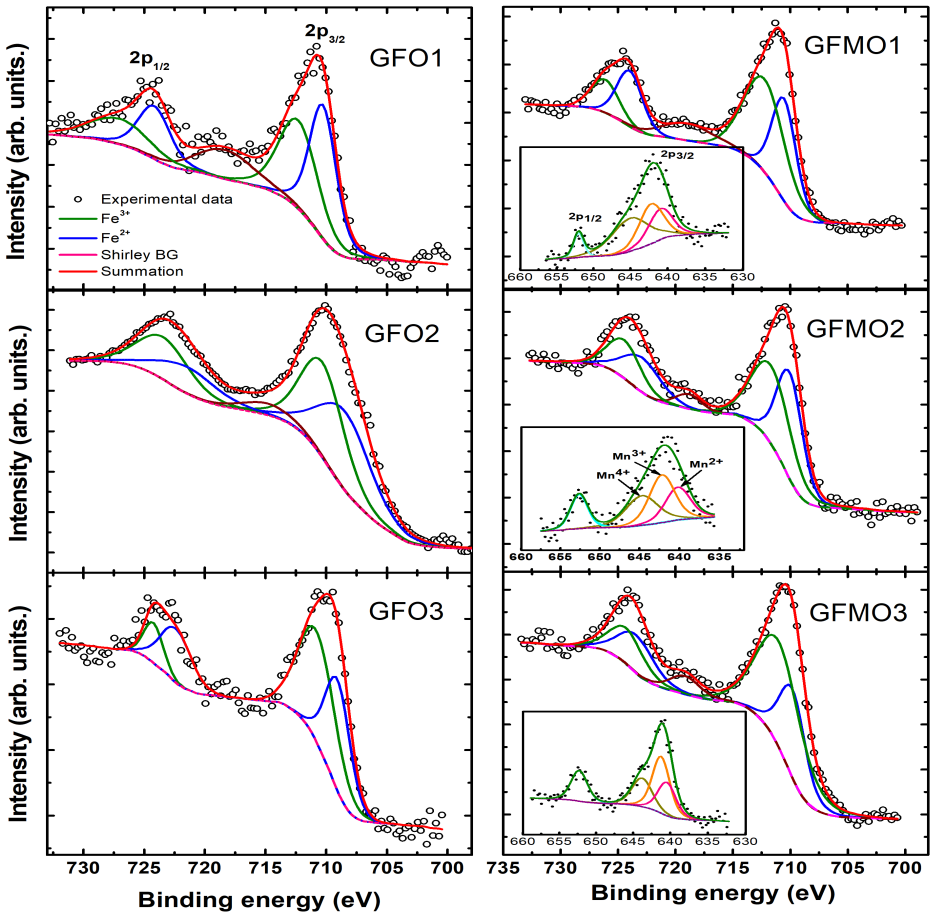

Figure 3.10: XPS analysis of Fe element of all samples. Insets in GFMOn are the XPS spectra of Mn compound.

To understand the chemical states of doped elements in the samples, X-ray Photospectroscopy (XPS) is performed. All elements were

observed at their respective binding energy state. Here we analyze the obtained XPS data of Fe and Mn using CasaXPS software [39]. The binding energy of C1s (284.6 eV) was used as the reference peak for all other spectra analysis. Fig. 3.10 shows the fitted XPS data for Fe element present in the samples. Fe 2P splits into two main peaks $2p_{1/2}$ and $2p_{3/2}$ components due to spin-orbit coupling. The peaks were further deconvoluted to estimate Fe^{3+} and Fe^{2+} ions contributions. The concentration ratios of Fe^{3+}/Fe^{2+} ions with satellite for GFOn are calculated as 47.92/36.3/15.78, 49.59/45.29/4.78, 52.07/48.93 for n = 1, 2 and 3 respectively. For GFMOn the values are found to be 49.63/41.24/9.12, 49.11/46.54, 58.46/36.03/5.50 for n = 1, 2 and 3 resp. This shows the co-existence of Fe^{3+} and Fe^{2+} ions. Fe^{2+} ion can be formed within the iron sublattice even by a slight oxygen deficiency in the compounds. Equation 3.1-3.4 indicates the creation of Fe^{2+} ions [40].

$$O_o \rightarrow V_o + \frac{1}{2}O_2 \tag{3.1}$$

$$V_o \rightarrow V_o^{\bullet} + e' \tag{3.2}$$

$$V_o^{\bullet} \rightarrow V_o^{\bullet\bullet} + e' \tag{3.3}$$

$$Fe^{3+} + e' \rightarrow Fe^{2+} \tag{3.4}$$

The presence of Fe^{2+} confirmed by CasaXPS fitting indicates Fe^{2+} -

Fe^{3+} polaronic hopping phenomena [41] which could be explained by the process,

$$2Fe_{Fe}(2Fe^{3+}) + O_o \leftrightarrow \frac{1}{2} + V_o^{\bullet\bullet} + 2Fe'_{Fe}(2Fe^{2+}) \tag{3.5}$$

It is seen that in all samples, the amount of Fe^{3+} ions are higher than Fe^{2+} ions, which agrees well with the excellent magnetic behavior obtained in the compounds depicted in figure 3.8. XPS spectra of Mn were also recorded for GFMOn samples, shown in the inset of corresponding Fe spectra. The peaks at B.E. $\sim$ 641 eV and $\sim$ 653 eV corresponds to the Mn components; $Mn2p_{3/2}$ and $Mn2p_{1/2}$, which are split due to spin-orbit coupling. Mn $2P_{3/2}$ is further deconvoluted into Mn^{4+}, Mn^{3+}, and Mn^{2+}. Interaction between Mn ions and Fe ions could lead to electron transfer causing vacancy degeneracy as

$$Mn^{4+} + Fe^{2+} \leftrightarrow Fe^{3+} + Mn^{3+}. \tag{3.6}$$

3.3.6 Temperature dependent Raman Spectroscopy and spin phonon coupling on $GaFeO_3$

As mentioned earlier, the room-temperature orthorhombic phase of GFO has eight formula units in the crystallographic unit cell. The cations are occupied at four in-equivalent sites. The non-magnetic Ga1

and Ga2 ions occupy at 4a sites while magnetic Fe1 and Fe2 ions sit at 4a sites and six oxygen ions occupy at 4a sites. Since the primitive cell has eight formula units, one can expect 40 atoms in the orthorhombic primitive cell which translate into 117 ($\Gamma = 0$) optical phonon modes. Detailed group theoretical analysis of the orthorhombic phase has not yet reported so far. A systematic group theoretical analysis of phonon modes from the C_{2v} factor group of the crystal using correlation method is presented in table 3.4. The corresponding mode symmetry and their spectral activity are also included in the table.

Table 3.4: Factor Group theoretical analysis of modes from C_{2v} factor group on $GaFeO_3$ system

	Site		site	C_{2v} factor group			
Atoms	a	b	representation	A1	A2	B1	B2
Ga1	4a	C1	A	3	3	3	3
Ga2	4a	C1	A	3	3	3	3
Fe1	4a	C1	A	3	3	3	3
Fe2	4a	C1	A	3	3	3	3
O1	4a	C1	A	3	3	3	3
O2	4a	C1	A	3	3	3	3
O3	4a	C1	A	3	3	3	3
O4	4a	C1	A	3	3	3	3
O5	4a	C1	A	3	3	3	3
O6	4a	C1	A	3	3	3	3
			Γ_{total}	30	30	30	30
			$\Gamma_{acoustic}$	1	1	1	1
			$\Gamma_{optical}$	29	30	29	29
			Γ_{raman}	29	30	29	29
			Γ_{IR}	29		29	29

The group theoretical classification of normal modes is $\Gamma_{opt} = 29A_1 + 30A_2 + 29B_1 + 29B_2$, which are all Raman active, where A_1, B_1 and

B_2 are active in infrared. Therefore, 117 Raman active phonons are expected to be observed. All phonon modes are non-degenerate. The reduced Raman spectra of GFO at selective temperatures are shown in figure 3.11. At room temperature the major Raman bands are located at 86, 119, 151, 170, 239, 353, 395, 439, 468, 692 and 747 cm^{-1} in the frequency range of 50 - 900 cm^{-1}. A total of 17 Raman modes are identified using Raman line-shape analysis. The observed Raman spectrum and the total simulated Lorentzian least squares curve fit pattern are depicted in Figure 3.11(a). The observed Raman mode frequencies are similar to those reported earlier [29]. The observed Raman mode frequencies are less than the theoretically predicted one. The less number of modes could be accidental degeneracy of several phonon frequencies lying close to each other or smaller polarizability of several phonons leading to insufficient intensity. To account for the structural changes [42], spin-phonon coupling [29, 43] the thermal evolution of phonon spectra are useful. The elimination of thermal population factor from Raman spectra are essential for analyzing the spectra to identify and ascertain the magnetoelastic coupling and structural ordering arising at induced temperature. The experimental raw Raman spectra were corrected from the Bose-Einstein thermal factor using $I(\omega) = I_{exp}(\omega)/[1 + n(\omega,T)]$, where $n(\omega, T) = [\exp(\hbar\omega/k_BT) - 1]^{-1}$, where

$I_{exp}(\omega)$ is the recorded Raman intensity and the n(ω, T) is the phonon occupation number, $\hbar$ and k_B are the Planck and Boltzmann constants, respectively. The lorentzian multicomponent line-shapes analysis was adopted to follow the changes in Raman spectra quantitatively. A minimum number of Lorentzian peaks were considered to fit each spectrum, which yielded a good agreement between the experimental data and the total fitted Raman spectra. If more number of spectral lines than required were used, it leads to strong correlations in fitted parameters due to their inherent large standard errors, that could lead to unphysical interpretation. Secondly, at low temperature, the Raman peaks become sharper due to the increase in the phonon lifetime; thereby, often overlapping modes are resolved. Thus, the analyses of Raman spectra were carried at 82 K, the lowest temperature of the present study. The deconvolution of the Raman peaks of the spectrum recorded at 82 K, yielded 31 modes (Figure 3.11(b)). Table 3.5 lists the normal mode frequencies of the observed Raman mode frequencies, and the mode positions are marked in Figure 3.11(a). Upon increasing temperature, the Raman bands soften continuously due to anharmonicity involved in the interatomic potential. A few Raman modes located at 153, 175, 240, 700, and 756 cm^{-1} show faster hardening behavior below 220 K, the magnetic phase transition temperature, T_C. The line-widths of modes

are broadened, and peak intensities decrease due to enhance phonon scattering mechanism; hence, at room temperature, only 17 modes are observed due to mode broadening resulting into coalescing of a few peaks with each other (Table 3.5). Neither disappearance of existing modes nor appearance of any new modes proves the absence of structural phase transition in GFO within the temperature range. Earlier temperature dependent diffraction studies [9, 29] on GFO indicates the structural stability of the compound in the similar temperature range.

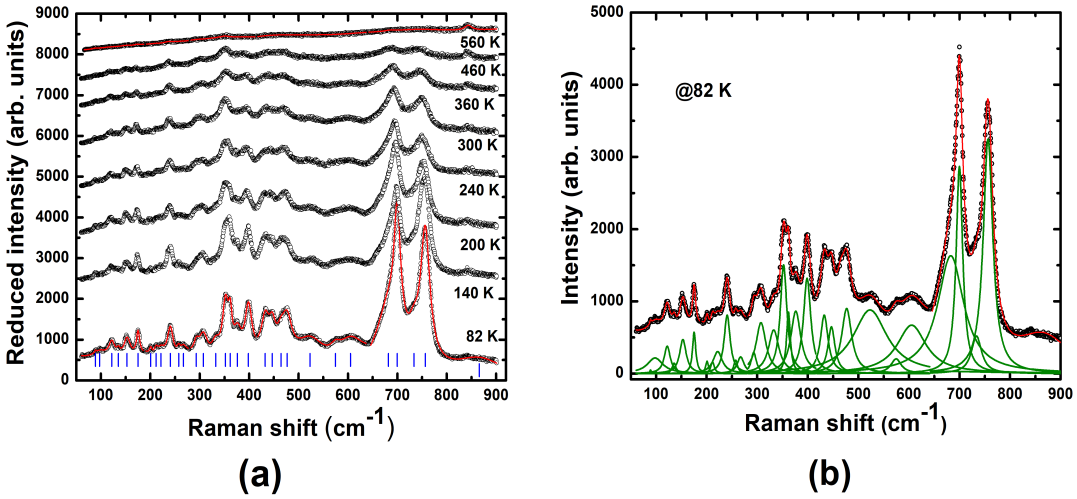

Figure 3.11: (a) Reduced Raman spectrum obtained after correcting for the thermal population factor. Multi-Lorentzian fitted reduced Raman spectra measured at 82, and 560 K. Vertical ticks indicate the individual fitted Lorentzian peak positions. (b) The reduced Raman spectrum for the $GaFeO_3$ at 82 K along with Lorentzian fits. Solid curves are the Lorentzian least-square fits to data. Individual fitted Lorentzian peaks are also shown.

Often coupling between the spin degree of freedom and phonons are observed in MF compounds. Studies on spinphonon coupling in oxides play an important role in its exotic properties; by varying its mag-

Table 3.5: Observed mode frequencies at 82 K, 300 K, their mode assignments and spin-phonon coupling constant (λ) for modes are also given:

82 K (cm^{-1})	300 K (cm^{-1})	Assignment	Spin-phonon coupling constant (λ)
89.64	87.84	...	
99.99	99.5(w)	...	
122.48	118	Translational modes	
134.98	133.91(b)	...	
152.9	151.6	...	0.89
175.22	172.35	...	1.1
200.32	199.47	...	
212	...	...	
221.8	...	...	
240	239.02	...	0.89
258.3	...	Librational modes	
267.27	..	of rigid units	
294.84	..	...	
307.12	303.29	...	
353.62	..	...	
359.9	..	...	
375.21	..	...	
399.2	395.55	Bending vibration	
433.34	..	of polyhedral units	
445.31	442.3	...	
473.84	470.4	...	
525.78	524.12	...	
604.81	602.22	Stretching vibration	2.14
700	693.52	of polyhedral units	2.93
755.9	749.7	...	
842.38	845.3		

netic ordering, its structural properties can be controlled [44]. Often the strength of the spinphonon coupling parameter on these oxides is related to their magnetoferroelectricity, colossal magnetoelastic behavior, etc. Therefore, it is of interest to examine the coupling strength of phonon modes of oxides and get insight into the intriguing spin or-

dered coupling phenomena in that material. The magnetoelastic coupling is manifested in the magnetodielectric effect, dielectric behavior, and phonon spectra [17, 20, 44, 45]. In Raman spectra, the change in phonon frequency with temperature has a contribution from lattice anharmonicity, spin-phonon interaction, and electron-phonon coupling effect.

As discussed earlier, the perovskite orthorhombic structured GFO consists of Ga1-O tetrahedron corner shared with Ga2-O, Fe1-O and Fe2-O octahedron units while the cations octahedral units have edge shared networks. The Ga1-O4 tetrahedra unit is tightly bound whereas octahedral units are comparatively loosely bound. Therefore, in the present Raman spectra of GFO, the vibrational mode involving tetrahedral vibration can be seen in the high-frequency region and the mode vibrations involving octahedral units are expected in the low-frequency part. Hence, the Raman spectrum is contributed by the vibrational modes associated with both tetra- and octahedral units. The internal vibration represented by high-frequency range 650 - 850 cm^{-1} is attributed to the symmetric stretching vibration of GaO4 units, while the symmetric stretching vibrations of octahedral units are in the range of 600 - 650 cm^{-1}. The asymmetric stretching vibration of tetra and octahedral units are observed in the range 500 - 900 cm^{-1}. The bending

vibrations of these polyhedral units are assigned in between 400 - 490 cm^{-1}. The librational modes (rigid rotation) involving the tetrahedral and octahedral rigid units and the lattice translational mode related to Ga^{3+} and Fe^{3+} cations are noticed in the low-frequency range 80 - 390 cm^{-1}. As mentioned in the introduction, the temperature induces a change in the mode frequency is a consequence of lattice anharmonicity, spin-phonon coupling, and another excitation effect like electron-phonon coupling [42, 46]. However, the latter electron-phonon contribution is absent since GFO is a dielectric. Hence, the resulting contributions from anharmonicity and spin-phonon coupling are expected for observed shift in mode frequencies in GFO with temperature. Furthermore, as the magnetic ordering is observed below T_C (220 K), one can expect the spin-phonon coupling below T_C, in the low-temperature ferrimagnetic phase. Above T_C, in the high-temperature paramagnetic phase, the only anharmonicity governs the shift in mode frequency and can be analyzed by using the sole anharmonicity formalism, consists of a major contribution from cubic and quartic anharmonicity [42]. The effect of cubic anharmonicity leads to decay of a phonon of frequency ω_o into two phonons of each frequency $\omega_o/2$, whereas quartic anharmonicity resulting in three phonons of each frequency $\omega_o/3$. Therefore, the shift in frequency (ω) can be analyzed by using the relation $\omega =$

ω_o + C [1 + 2/(exp(x)-1)] + D [1 + 3/(exp(y)-1) + 3/(exp(y)-1)$^{-1}$], where, ω_o is mode frequency at 0 K, x = $\hbar\omega/2k_BT$ and y = $\hbar\omega_o/3k_BT$. C and D are coefficient of cubic and quartic anharmonicity, respectively. The observed mode frequencies namely 153, 175, 240, 700 and 756 cm^{-1} exhibiting steeper hardening below T_C, are fitted for the paramagnetic phase using the above expression in figure 3.12. An example of mode frequency that hadn't exhibited magnetoelastic coupling (399 cm^{-1}) is also shown in figure 3.12. The prominent mode at 240 cm^{-1} exhibits higher dispersion of the measured data since the mode frequency is affected by the neighboring weak modes located at 221 and 257cm^{-1}. These near-by weak modes are not observed at higher temperature (280 K) due to their insufficient intensity. A significant shift in mode frequency ($\Delta\omega$) from the theoretically extrapolated line below T_C can be attributed to the spin-phonon coupling effect, govern by using the relation, $\Delta\omega = \lambda^*$<Si.Sj>; where <Si.Sj> is the spin-spin correlation function and λ is the spin-phonon coupling constant. Similar kind of mode behavior due to magnetoelastic coupling is observed in several magnetic systems, such as MnF_2 [47], FeF_2 [47], $Sr_4Ru_3O_{10}$ [48], $BiFeO_3$ [49]. The shift in mode frequency $\Delta\omega$ is given in table 3.5. The internal mode located at 756 cm^{-1} is found to have a large magnetoelastic coupling with $\Delta\omega$ value as large as 4.4 cm^{-1} while the lowest

value of $\Delta\omega$ is observed for translational mode at 153 cm^{-1} indicating its weaker spin-phonon interaction.

One can estimate quantitatively the magnetoelastic coupling constant between the phonon and the Fe-cationic spins in the ferrimagnetic phase. As mentioned earlier, the stronger magnetic interaction is ferromagnetic along c-axis, and it is weaker in the ab-plane; the net magnetic ordering is ferrimagnetic in nature. The spin-spin correlation function can be approximated by using molecular field approximation and <Si.Sj> can be obtained from the ensemble average of nearest-neighbor spins [48, 29] as <Si.Sj> = $2[M(T)/Ms]^2$, where M(T) is the magnetization per Fe-site magnetic ion, Ms represents the saturation magnetization. The factor 2 is considered to take care of two sets of nearest-neighbors of Fe-cations in a unit cell. The resulting expression for the phonon frequency due to spin-phonon coupling effect can be written as: $\Delta\omega = \lambda^* 2[M(T)/Ms]^2$. The slope of the plot of ω versus $[M(T)/Ms]^2$ shown in figure 3.13 essentially represent spin-phonon coupling strength λ. We examine those modes (effected by magnetic ordering), namely 153, 176, 240, 700, and 756 cm^{-1} behavior with respect to $[M(T)/Ms]^2$ and the respective coupling constants are obtained (Table 3.5). The spin-phonon coupling strength is found to be larger for internal mode vibrations located at 700 and 756 cm^{-1}. Translational

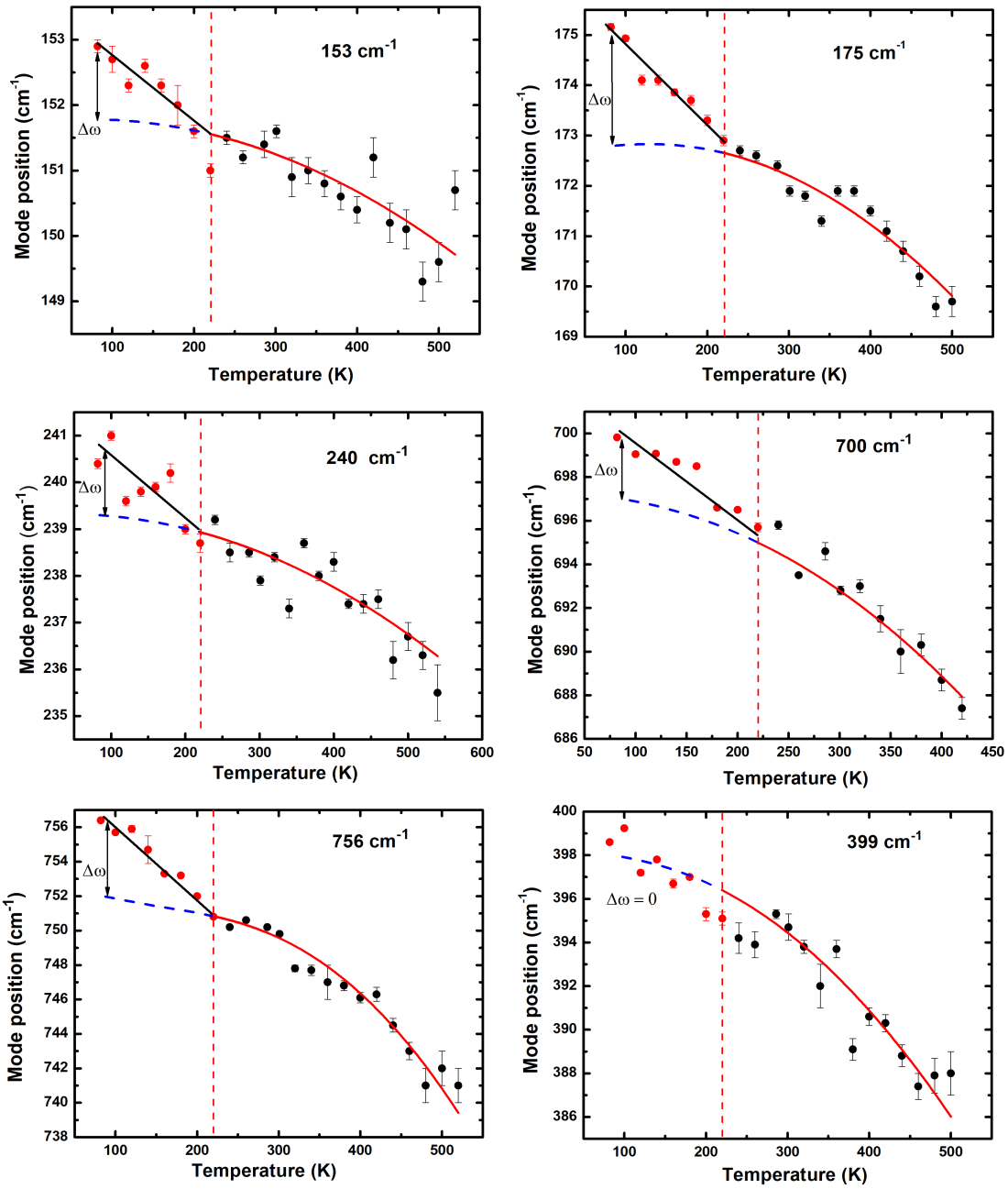

Figure 3.12: Mode frequency vs. temperature for several characteristic phonons. The anharmonic model was used to fit the data in the paramagnetic phase above 220 K. Extrapolated phonon positions in the ferrimagnetic phase below 220 K was used to extract the frequency shift ($\delta\omega$). An example of the mode at 399 cm^{-1} which is not affected by spin-phonon coupling is also included.

modes at 153 and 175 cm^{-1} and the librational rigid mode at 240 cm^{-1} are found to have nearly the same coupling strength ($\lambda \sim 1$). Larger λ values of internal modes indicate a stronger sensitivity of magnetic interaction to the atomic vibration displacements. The magnitude of λ values is found to be three times larger than the earlier reported [29] value for a 374 cm^{-1} librational rigid vibrational mode. In contrast to earlier observation on the change of spin dynamics $\sim$ 180 K [29], no anomaly in mode frequency ω versus magnetization around $\sim$ 180 K is found in the present study.

3.3.7 Dielectric studies

Figure 3.14 show frequency dependent permittivity (ϵ_r) of the GFOn and GFMOn measured at RT in the frequency range 100 Hz - 1 MHz. With increase in Fe/Mn concentration, permittivity is increased at low frequency regime. However, at high frequency regime, the change in permittivity is insignificant with Fe-doping. For pure composition (GFO1), ϵ_r value is $\sim$ 100 at 100 Hz. This value is increased to $\sim$ 400 for Fe and Mn doped compounds. On the other hand, it is seen that ϵ_r and tanδ are strongly dependent on frequency, as in figure 3.14. Permittivity values of GFOn and GFMOn are at 130 - 430 at lowest frequency (100 Hz), which decreases to $\sim$ 50 for frequencies higher than 1

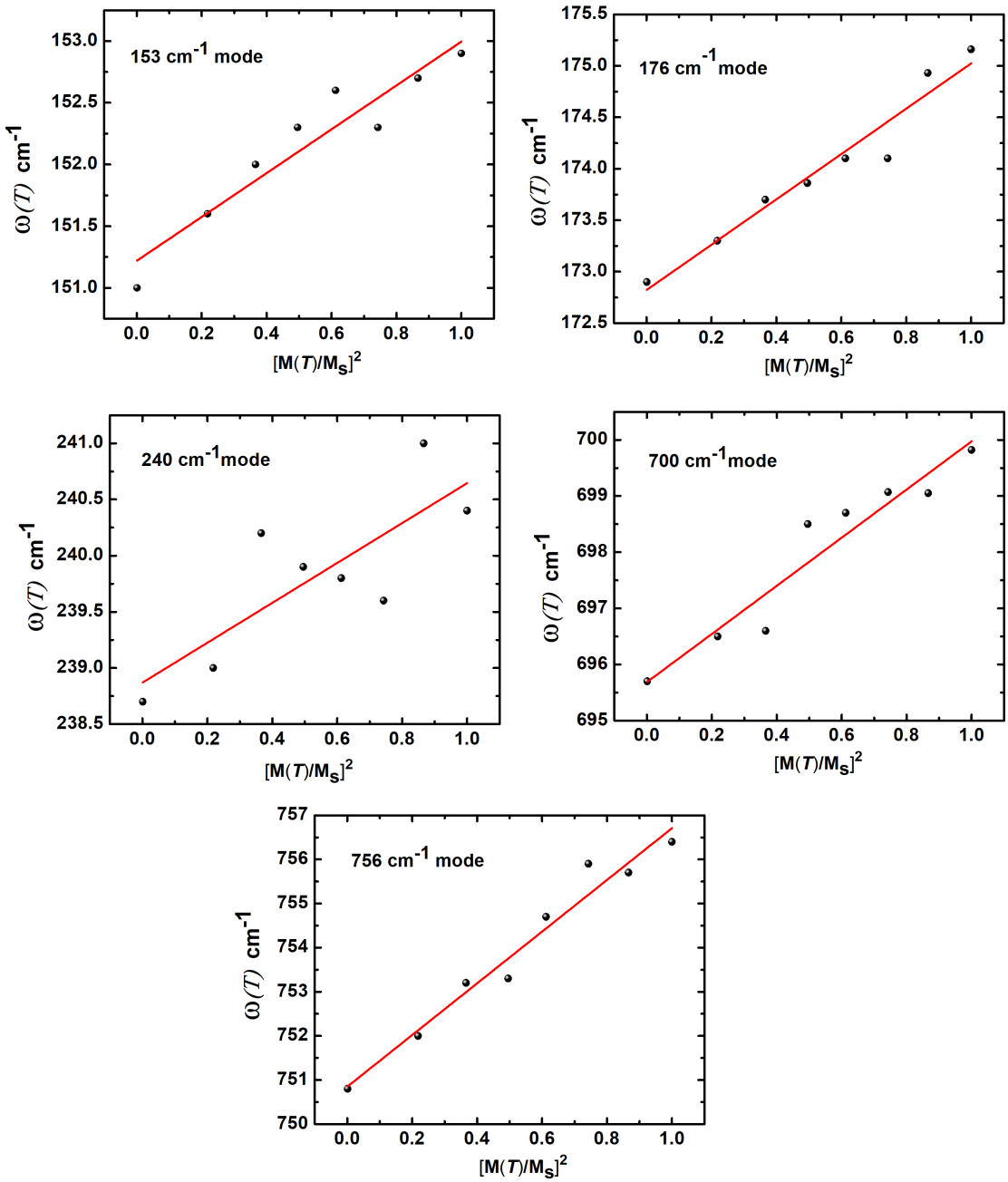

Figure 3.13: Plots of ω(T) versus [M(T)/Ms]^2 are shown for 153, 176, 240, 700, and 756 cm^{-1} modes. Linear least square fits to the data are shown by lines. Slope of these lines represent the spin-phonon coupling constants, λ.

kHz. Permittivity initially decreases sharply with increase in frequency upto 1 kHz and then decreases slowly and become almost constant up

to 1 MHz, which is usual dielectric dispersion. The dispersion of dielectric constant with frequency is due to Maxwell-Wagner type interfacial polarization in agreement with Koop's phenomenological theory [50, 51, 52]. It is well known that the polarization in ferrite is through a mechanism similar to the conduction process. The dipole of ferrite (Fe^{3+} and Fe^{2+}) experiences rotational displacement that results in orientation polarization. The polarization at lower frequencies may result from electron hopping between $Fe^{3+} \leftrightarrow Fe^{2+}$ and $Mn^{2+} \leftrightarrow Mn^{3+}$ ions in ferrite lattice. With increase in frequency, the polarization decreases and reaches a constant value as seen in figure 3.14. It is due to the fact that beyond a certain frequency of external field the electron exchange $Fe^{3+} \leftrightarrow Fe^{2+}$ and $Mn^{2+} \leftrightarrow Mn^{3+}$ cannot follow the alternating field [53].

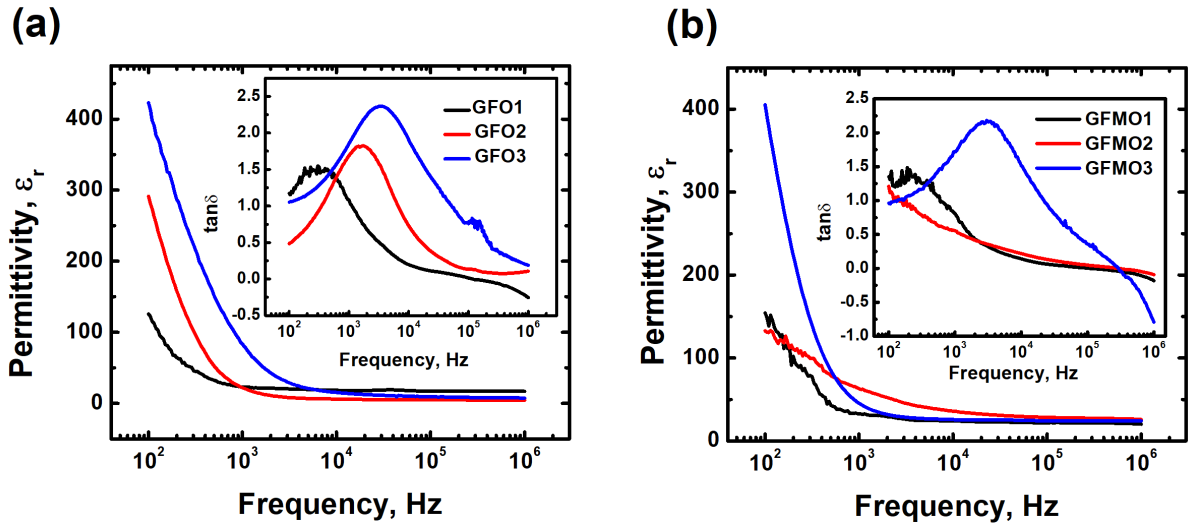

Figure 3.14: Room temperature frequency dependent permittivity of (a) GFOn and (b) GFMOn. Inset of represents tangent loss of (a) GFOn and (b) GFMOn

The dispersion of ϵ_r can also be explained based on the contributions from various sources of polarizations, such as electronic, atomic, and orientation, and interfacial (space charge polarization). Electronic and atomic polarizations are frequency independent, but orientational and interfacial polarizations are frequency dependent. In frequency region of 100 Hz to 1kHz, all types of polarization appear. Above 1 kHz, there are contributions only from electronic and ionic polarization. The decrease in orientational and space charge polarization with increasing frequency is responsible for decrease in ϵ_r at high frequency.

Inset figures show the loss tangent (tanδ) of respective compounds. In general, the dielectric loss in polycrystalline ferrites is a result of the lag in polarization with respect to the applied alternating electric field. The dielectric loss peak is observed in some compositions. This indicates that a polarizing species with a relatively long relaxation time [54]. This is originated from the thermally activated long and/or short range movement of charge carriers such as space charges, various charged defects etc. Moreover, the loss factor is considered to be caused by domain wall resonance. At higher frequencies, losses are found to be low since domain wall motion is inhibited and magnetization is forced to change by rotation [53].

We studied temperature dependent dielectric constant and dielectric

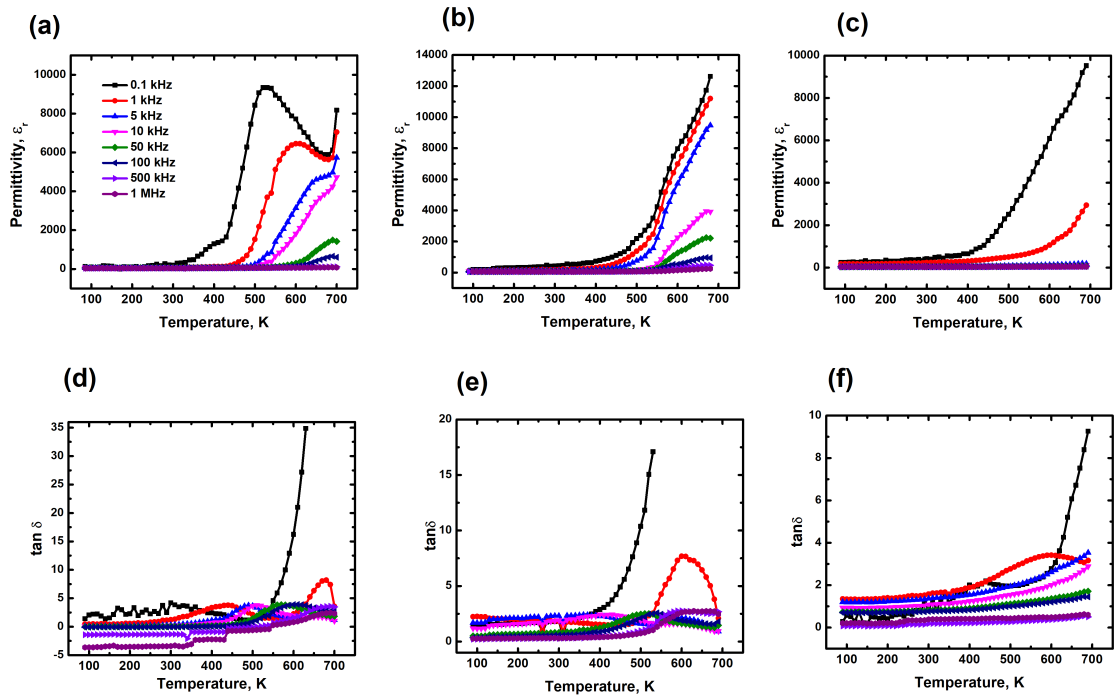

Figure 3.15: (a, b, c) Temperature dependent permittivity and (d, e, f) dielectric loss of GFO1, GFO3, and GFMO3 repectively measured at various frequencies

loss for GFO1 ($GaFeO_3$, principle compound) and the compositions with T_C > RT, they are GFO3 and GFMO3. Figure 3.15(a,b, and c) are the plots of temperature dependent permittivity of GFO1, GFO3 and GFMO3 repectively. This study is done in the temperature range of 90 to 700 K and frequency range of 100 Hz - 1 MHz. In case of GFO1, figure 3.15(a), we can see the dielectric maxima shifting towards higher temperature for larger frequency. Within the given temperature range, maxima peak is not seen for high frequencies (>100 kHz) . In case of GFO3 and GFMO3, dielectric maxima could not be observed within the temperature range (figure 3.15 (b and c)). Unfortunately, we

have experimental limitation to go beyond 700 K. However the trend of increasing permittivity is analogous to GFO1, i.e. the dielectric maxima of lowest frequency (100 Hz) is largest and appears at lowest temperature whereas, the maxima for highest frequency is smallest and appears at highest temperature.

The increase in permittivity with temperature can be explained as: at relatively low temperature (i.e. upto 300 K), charge carriers are unable to orient themselves in the direction of applied field contributing less polarization that result in lower permittivity. On increasing temperature, more bound charges are released and the mobility of charge carriers increases due to the increase in thermal energy, which enable them to align in the direction of easy axis of an applied AC field. This in turn, enhances their contribution to space charge polarization leading to an increase in the value of permittivity. As mentioned above, dielectric constant of any material is due to the dipolar, electronic, ionic and interfacial polarization. At low frequencies, dipolar and interfacial polarization (which are strongly temperature dependent) known to play the dominate role. The interfacial polarization increases with increasing temperature via generation of crystal defects, whereas dipolar polarization decreases with increasing temperature. The rapid increase in the permittivity with temperature at low frequencies suggests that

the effect of the temperature is more pronounced on the interfacial than on the dipolar polarization. At high frequencies, electronic and ionic polarization are the main contributors and hence their temperature dependence is insignificant [55, 56, 57].

In figure 3.15(a) shifting of dielectric maxima at higher temperature with increasing frequency resembles the relaxor nature of the compound. Moreover, large dielectric dispersion below and above T_m and a similar shift of dielectric loss peak with temperature strongly suggests the relaxor behavior. Temperature dependent dielectric loss of GFO1, GFO3, and GFMO3 is shown in figure 3.15(d, e, and f) respectively. In case of GFO1 (figure 3.15(d)), one prominent peak is clearly observed at all frequency. It can be seen that there tends to appear secondary peak at higher temperature region. This behavior is seen in dielectric graph as well. Likewise, the maxima shifts towards higher temperature with higher frequency. The compounds possess loss of $\sim$ 1 to 2.5 upto $\sim$ 400 K, at high temperature, graph shows speedy increasement. The high loss could be the consequences of oxygen vacancies formed during sintering process due to volatilization and/or charge compensation process. The material is synthesized at high temperature, so both Fe^{2+} and Fe^{3+} naturally develop in the matrix. These Fe ions aid to increase ionic conduction at higher temperature, resulting the speedy raise of

dielectric loss at high temperature [58, 59, 60].

3.3.8 Leakage Current (I-V)- study

Figure 3.16 shows the IV characteristics of GFOn and GFMOn. The current was recorded within both polarities of DC applied the electric field. With an increase in Fe contents leakage, current density increases as Fe is transition metal with lower resistivity.

On doping Mn, the leakage current is reduced in all composition approximately by 2 orders, which indicates the significant improvement in the reduction of leakage current density. The decrease in leakage current could be due to the substitution of Fe^{2+} with Mn^{2+} that decreases the hopping possibilities between Fe^{2+} and Fe^{3+}. A possible mechanism explaining this behavior can be explained using the Kröger-Vink notation, oxygen vacancies in compounds during the growth process can be written.

$$\delta O_o^x \rightarrow \delta(V_o^{\bullet\bullet} + 2e' + \frac{1}{2}O_2) \tag{3.7}$$

Where $V_o^{\bullet\bullet}$ is oxygen vacancy with a double positive charge. Fe^{3+} acts as an acceptor of electrons and gets reduced into Fe^{2+}.

$$2\delta Fe_{Fe}^X + 2\delta e^- \Leftrightarrow 2\delta Fe'_{Fe}(Fe^{3+}toFe^{2+}) \tag{3.8}$$

Thus, it allows the electrical conduction via a hopping mechanism

due to simultaneous presence of $Fe^{2+}$and Fe^{3+}, which is also elucidated above in XPS study. Immediately after completing Fe oxidation (all Fe^{2+} ions become Fe^{3+}), further oxidation (second-stage oxidation) increases current density due to the formation of hole $h^{\bullet}$ which can be written as $\delta\ V_o^{\bullet\bullet} + \frac{1}{2}\ O_2 \rightarrow O_o^X + 2h^{\bullet}$ resulting in higher leakage, which is seen in figure 3.16(a).

In the case of Mn-doped GFO, the substitution of Fe with Mn leads to the creation of holes.

$$\delta MnO \rightarrow \delta(Mn'_{Fe} + h^{\bullet} + \frac{1}{2}O_2) \tag{3.9}$$

where Mn'_{Fe} represents Mn in the Fe site with an apparent negative charge and $h^{\bullet}$ denotes a hole. These holes can be recombined with electrons $e^- + h^{\bullet} \rightarrow 0$. In this case, Mn acts as a buffering species for suppressing an increase of $h^{\bullet}$ by oxidation. After Fe^{2+} is completely oxidized to Fe^{3+}, Mn^{2+} absorbs $h^{\bullet}$ generated in further oxidation process by the valence increase of Mn [61] as expressed by

$$Mn'''_{Fe} + h^{\bullet} \rightarrow Mn''_{Fe}(Mn^{2+} to Mn^{3+}) \tag{3.10}$$

$$Mn''_{Fe} + h^{\bullet} \rightarrow Mn'_{Fe}(Mn^{3+} to Mn^{4+}) \tag{3.11}$$

Thus, the origin of lower leakage observed in Mn-GFO compounds

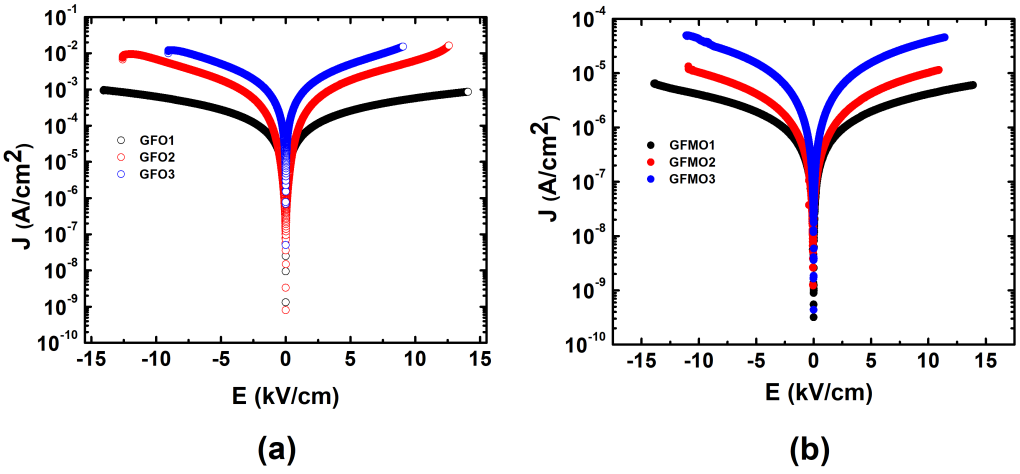

Figure 3.16: Leakage current of (a) GFOn and (b) GFMOn

is plausibly by the hole absorbing function originating from the Mn-valences.

3.3.9 Magnetoelectricity study

To confirm the magnetoelectric coupling, we have carried out magnetocapacitance, magneto loss, magnetoimpedance and magneto-phase measurements of GFO3 at RT. The direct magnetodielectric coupling of the system can be calculated qualitatively in terms of magneto-capacitance (MC%), magneto-loss (ML%), magneto-impedance(MI%) and magneto-phase (Mϕ%) with the help of M-W equations [62, 63].

$$MC(\%) = \frac{C(H,T) - C(0,T)}{C(0,T)} X100\% \tag{3.12}$$

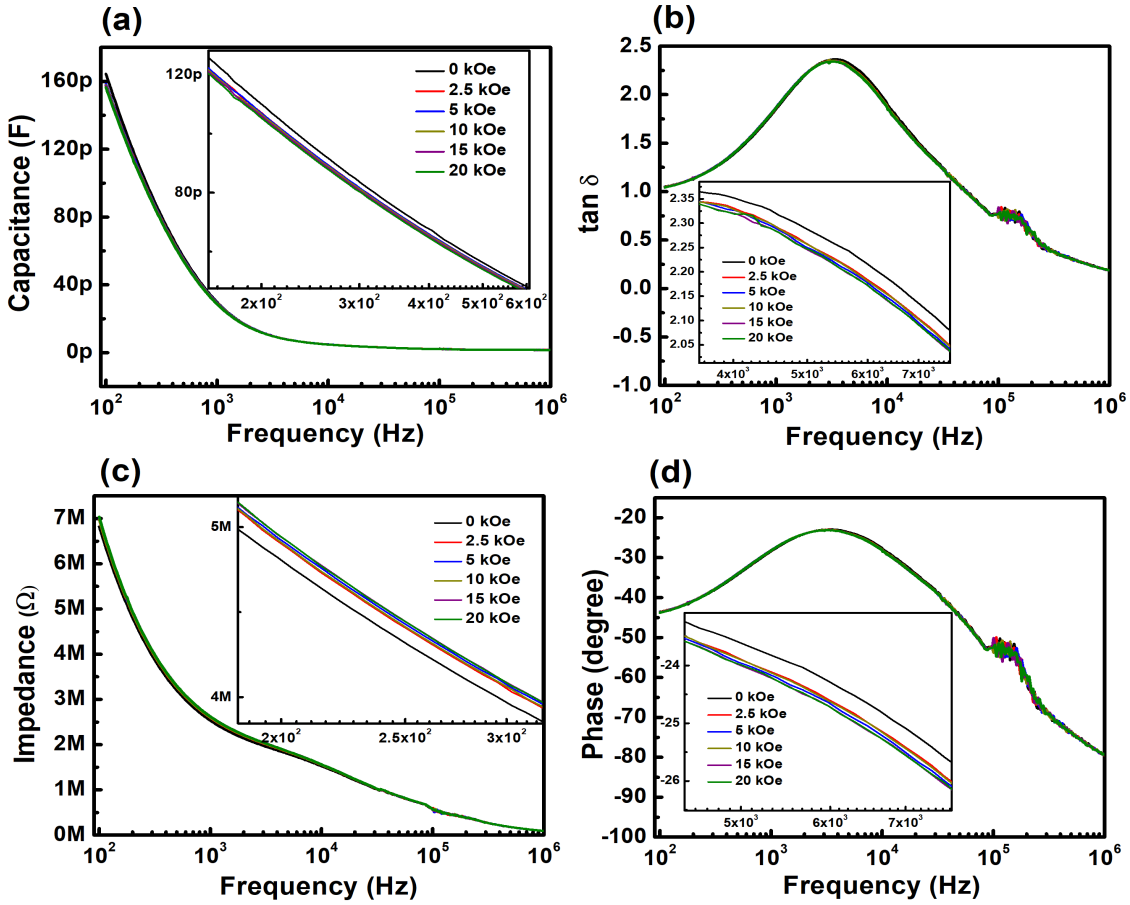

Figure 3.17: (a) Capacitance, (b) dielectric loss, (c) Impedance, (d) phase angle as a function of frequency for GFO3 ceramic. Insets show the magnified version of respective plot.

$$ML(\%) = \frac{tan\delta(H,T) - tan\delta(0,T)}{tan\delta(0,T)} X100\% \tag{3.13}$$

$$MI(\%) = \frac{I(H,T) - I(0,T)}{(I(0,T)} X100\% \tag{3.14}$$

$$M\phi(\%) = \frac{\phi(H,T) - \phi(0,T)}{\phi(0,T)} X100\% \tag{3.15}$$

Figure 3.17(a-d) shows the frequency dependent electrical characters (capacitance, tangent loss, impedance and phase angle) of GFO3 collected at several static bias magnetic field (0≤H≤ 2T). Insets are the

enlarged version of respective characters shown to highlight the changes with applied bias magnetic field. In figure 3.17(a) the capacitance decreases throughout the frequency range on increasing static magnetic field implying negative coupling coefficients. On changing static field from 0 T to 0.5 T, a significant change of capacitance, whereas at high field, i.e. on increasing field from 0.5 T to 2 T, the change in capacitance is minimal. It is because once the spin is aligned the changed in magnetic configuration with increasing field become negligible [58]. Using above formula, MC(%), ML (%), MI(%), Mϕ (%) is calculated at 1 kHz w.r.t maximum field (2T) which is obtained as -3.6%, 0.7%, 3.46%, 0.6% respectively. On applying magnetic field to a multiferroic system, the magnetic phase shows piezomagnetic effect and gets strained. This strain induces stress which generates electric field on ferroelectric domains; that helps to modify electrical order parameters such as capacitance, loss and impedance [62, 64, 65]. In figure 3.17(b), the dielectric loss increases on increasing frequency at the beginning and then decreases after certain frequency. This indicates the increase in deflection boundary in dielectric leading to relaxation behavior which is similar to Debye relaxation [66]. This is further cleared in our case by phase vs frequency plot in figure 3.17(d). These results confirm the presence of coupling between magnetic and electrical parameters at RT.

Bibliography

[1] Wilma Eerenstein, ND Mathur, and James F Scott. Multiferroic and magnetoelectric materials. *nature*, 442(7104):759, 2006.

[2] JF Scott. Multiferroic memories. *Nature materials*, 6(4):256–257, 2007.

[3] Casey Israel, ND Mathur, and JF Scott. A one-cent room-temperature magnetoelectric sensor. *Nature materials*, 7(2):93–94, 2008.

[4] Enno Lage, Christine Kirchhof, Viktor Hrkac, Lorenz Kienle, Robert Jahns, Reinhard Knöchel, Eckhard Quandt, and Dirk Meyners. Exchange biasing of magnetoelectric composites. *Nature materials*, 11(6):523–529, 2012.

[5] Xi Chen, Andreas Hochstrat, Pavel Borisov, and Wolfgang Kleemann. Magnetoelectric exchange bias systems in spintronics. *Applied physics letters*, 89(20):202508, 2006.

[6] Ramamoorthy Ramesh. Emerging routes to multiferroics. *Nature*, 461(7268):1218–1219, 2009.

[7] Manfred Fiebig. Revival of the magnetoelectric effect. *Journal of physics D: applied physics*, 38(8):R123, 2005.

[8] Sasikanth Manipatruni, Dmitri E Nikonov, Chia-Ching Lin, Tanay A Gosavi, Huichu Liu, Bhagwati Prasad, Yen-Lin Huang, Everton Bonturim, Ramamoorthy Ramesh, and Ian A Young. Scalable energy-efficient magnetoelectric spin–orbit logic. *Nature*, 565(7737):35–42, 2019.

[9] T Arima, D Higashiyama, Y Kaneko, JP He, T Goto, S Miyasaka, T Kimura, K Oikawa, T Kamiyama, R Kumai, et al. Structural and magnetoelectric properties of ga 2- x fe x o 3 single crystals grown by a floating-zone method. *Physical Review B*, 70(6):064426, 2004.

[10] Yu F Popov, AM Kadomtseva, GP Vorob'ev, VA Timofeeva, DM Ustinin, AK Zvezdin, and MM Tegeranchi. Magnetoelectric effect and toroidal ordering in ga 2- x fe x o 3. *Journal of Experimental and Theoretical Physics*, 87(1):146–151, 1998.

[11] JP Remeika. Gafeo 3: a ferromagnetic-piezoelectric compound. *Journal of Applied Physics*, 31(5):S263–S264, 1960.

[12] J. H. Jung, M. Matsubara, T. Arima, J. P. He, Y. Kaneko, and Y. Tokura. Optical magnetoelectric effect in the polar GaFeO3 ferrimagnet. *Physical Review Letters*, 93(3):037403–1, 2004.

[13] Y. Ogawa, Y. Kaneko, J. P. He, X. Z. Yu, T. Arima, and Y. Tokura. Magnetization-Induced Second Harmonic Generation in a Polar Ferromagnet. *Physical Review Letters*, 92(4):4, 2004.

[14] Rana Saha, Ajmala Shireen, Sharmila N. Shirodkar, Umesh V. Waghmare, A. Sundaresan, and C. N.R. Rao. Multiferroic and magnetoelectric nature of GaFeO3, AlFeO3and related oxides. *Solid State Communications*, 152(21):1964–1968, 2012.

[15] J. Y. Kim, T. Y. Koo, and J. H. Park. Orbital and bonding anisotropy in a half-filled GaFeO3 magnetoelectric ferrimagnet. *Physical Review Letters*, 96(4):2–5, 2006.

[16] Myung Joon Han, Taisuke Ozaki, and Jaejun Yu. Magnetic ordering and exchange interactions in multiferroic GaFeO3. *Physical Review B*, 75(6):060404, 2007.

[17] ZH Sun, BL Cheng, S Dai, LZ Cao, YL Zhou, KJ Jin, ZH Chen, and GZ Yang. Dielectric property studies of multiferroic gafeo3. *Journal of Physics D: Applied Physics*, 39(12):2481, 2006.

[18] Kaoru Eguchi, Yukito Tanabe, Tomoyuki Ogawa, Masaaki Tanaka, Yutaka Kawabe, and Eiichi Hanamura. Second-harmonic generation from pyroelectric and ferrimagnetic GaFeO3. *Journal of the Optical Society of America B*, 22(1):128, 2005.

[19] N. Kida, Y. Kaneko, J. P. He, M. Matsubara, H. Sato, T. Arima, H. Akoh, and Y. Tokura. Enhanced optical magnetoelectric effect in a patterned polar ferrimagnet. *Physical Review Letters*, 96(16):4–7, 2006.

[20] Somdutta Mukherjee, Ashish Garg, and Rajeev Gupta. Spin glass-like phase below 210 K in magnetoelectric gallium ferrite. *Applied Physics Letters*, 100(11):112904, 2012.

[21] Amritendu Roy, Somdutta Mukherjee, Rajeev Gupta, Sushil Auluck, Rajendra Prasad, and Ashish Garg. Electronic structure, Born effective charges and spontaneous polarization in magnetoelectric gallium ferrite. *Journal of Physics Condensed Matter*, 23(32):325902, 2011.

[22] Seungwoo Song, Hyun Myung Jang, Nam-Suk Lee, Jong Y Son, Rajeev Gupta, Ashish Garg, Jirawit Ratanapreechachai, and James F Scott. Ferroelectric polarization switching with a remarkably high activation energy in orthorhombic gafeo 3 thin films. *NPG Asia Materials*, 8(2):e242–e242, 2016.

[23] Daniel Stoeffler. First principles study of the electric polarization and of its switching in the multiferroic GaFeO 3 system. *Journal of Physics Condensed Matter*, 24(18):185502, 2012.

[24] J. Atanelov and P. Mohn. Electronic and magnetic properties of GaFeO3: Ab initio calculations for varying Fe/Ga ratio, inner cationic site disorder, and epitaxial strain. *Physical Review B - Condensed Matter and Materials Physics*, 92(10):1–11, 2015.

[25] Somdutta Mukherjee, Vishal Ranjan, Rajeev Gupta, and Ashish Garg. Compositional dependence of structural parameters, polyhedral distortion and magnetic properties of gallium ferrite. *Solid State Communications*, 152(13):1181–1185, 2012.

[26] Highscore plus software. *PANalytical*, 2004.

[27] L. Vegard. Die Konstitution der Mischkristalle und die Raumfullung der Atome. *Phys. Z.*, 5(1):17–26, 1921.

[28] C. V. Ramana, Y. D. Kolekar, K. Kamala Bharathi, B. Sinha, and K. Ghosh. Correlation between structural, magnetic, and dielectric properties of manganese substituted cobalt ferrite. *Journal of Applied Physics*, 114(18), 2013.

[29] Somdutta Mukherjee, Ashish Garg, and Rajeev Gupta. Probing magnetoelastic coupling and structural changes in magnetoelectric gallium ferrite. *Journal of Physics Condensed Matter*, 23(44), 2011.

[30] Sita Dugu, Karuna Kara Mishra, Dhiren K. Pradhan, Shalini Kumari, and Ram S. Katiyar. Coupled phonons and magnetic orderings in GaFeO3 : Raman and magnetization studies. *Journal of Applied Physics*, 125(6):064101, 2019.

[31] Dalhyun Do, Jin Won Kim, and Sang Su Kim. Effects of Dy and Mn codoping on ferroelectric properties of BiFeO 3 thin films. *Journal of the American Ceramic Society*, 94(9):2792–2795, 2011.

[32] Zhengjun Chai, Guoqiang Tan, Zhongwei Yue, Wei Yang, Meiyou Guo, Huijun Ren, Ao Xia, Mintao Xue, Yun Liu, Long Lv, and Yun Liu. Ferroelectric properties of BiFeO3 thin films by Sr/Gd/Mn/Co multi-doping. *Journal of Alloys and Compounds*, 746:677–687, 2018.

[33] N. Wang, F.S. Wen, L. Li, Y.F. Lü, S.C. Liu, Y.F. Lu, Z.Y. Liu, B. Xu, J.L. He, D.L. Yu, and Y.J. Tian. Magnetic frustration effect in polycrystalline Ga2xFexO3. *Journal of Magnetism and Magnetic Materials*, 322(21):3595–3600, 2010.

[34] G. H. Jonker. Magnetic compounds with perovskite structure iv. *Physica*, 22:707, 1956.

[35] K. Maaz, Arif Mumtaz, S. K. Hasanain, and Abdullah Ceylan. Synthesis and magnetic properties of cobalt ferrite (CoFe2O4) nanoparticles prepared by wet chemical route. *Journal of Magnetism and Magnetic Materials*, 308(2):289–295, 2007.

[36] M. Bakr Mohamed and H. Fuess. Effect of Mn doping on structural and magnetic properties of GaFeO 3. *Journal of Magnetism and Magnetic Materials*, 323(15):2090–2094, 2011.

[37] Sugata Ray, Priya Mahadevan, Suman Mandal, S. R. Krishnakumar, Carlos Seiti Kuroda, T. Sasaki, Tomoyasu Taniyama, and Mitsuru Itoh. High temperature ferromagnetism in single crystalline dilute Fe-doped BaTi O3. *Physical Review B - Condensed Matter and Materials Physics*, 77(10):1–6, 2008.

[38] Tanushree Chakraborty and Sugata Ray. Evolution of diffuse microscopic phases and magnetism in Ca, Fe co-doped BaTiO3. *Journal of Alloys and Compounds*, 610:271–275, 2014.

[39] N. Fairley. *CasaXPS Version 2.2.19*.

[40] Qingqing Ke, Xiaojie Lou, Yang Wang, and John Wang. Oxygen-vacancy-related relaxation and scaling behaviors of Bi0.9La0.1Fe0.98Mg0.02O3 ferroelectric thin films. *Physical Review B*, 82(2):024102, 2010.

[41] Vijay Singh, Aatish Daryapurkar, Shailendra S. Rajput, Somdutta Mukherjee, Ashish Garg, and Rajeev Gupta. Effect of annealing atmosphere on leakage and dielectric characteristics of multiferroic gallium ferrite. *Journal of the American Ceramic Society*, 100(11):5226–5238, 2017.

[42] K. K. Mishra, Sharat Chandra, Nilesh P. Salke, S. N. Achary, A. K. Tyagi, and Rekha Rao. Soft modes and anharmonicity in H3[Co(CN)6]: Raman spectroscopy and first-principles calculations. *Physical Review B - Condensed Matter and Materials Physics*, 92(13):1–9, 2015.

[43] Pradeep Kumar, Achintya Bera, D. V.S. Muthu, Sharmila N. Shirodkar, Rana Saha, Ajmala Shireen, A. Sundaresan, U. V. Waghmare, A. K. Sood, and C. N.R. Rao. Coupled phonons, magnetic excitations, and ferroelectricity in AlFeO3: Raman and first-principles studies. *Physical Review B - Condensed Matter and Materials Physics*, 85(13):1–6, 2012.

[44] Rajeev Gupta, M Kim, H Barath, SL Cooper, and G Cao. Field- and pressure-induced phases in sr 4 ru 3 o 10: A spectroscopic investigation. *Physical review letters*, 96(6):067004, 2006.

[45] Alexandre Thomasson, Jens Kreisel, Christophe Lefèvre, François Roulland, Gilles Versini, Sophie Barre, and Nathalie Viart. Raman scattering of magnetoelectric gallium ferrite thin films. *Journal of Physics Condensed Matter*, 25(4):0–6, 2013.

[46] Karuna Kara Mishra, Samatha Bevara, TR Ravindran, SJ Patwe, Mayanak K Gupta, Ranjan Mittal, R Venkata Krishnan, SN Achary, and AK Tyagi. High pressure behavior of complex phosphate k2ce [po4] 2: Grüneisen parameter and anharmonicity properties. *Journal of Solid State Chemistry*, 258:845–853, 2018.

[47] DJ Lockwood and MG Cottam. The spin-phonon interaction in fef2 and mnf2 studied by raman spectroscopy. *Journal of Applied Physics*, 64(10):5876–5878, 1988.

[48] Rajeev Gupta, M. Kim, H. Barath, S. L. Cooper, and G. Cao. Field- and pressure-induced phases in Sr4Ru3O10: A spectroscopic investigation. *Physical Review Letters*, 96(6):1–4, 2006.

[49] Manoj K Singh and Ram S Katiyar. Phonon anomalies near the magnetic phase transitions in bifeo3 thin films with rhombohedral r3c symmetry. *Journal of Applied Physics*, 109(7):07D916, 2011.

[50] James Clerk Maxwell. *Electricity and magnetism*. Oxford University Press, 1993.

[51] Karl Willy Wagner. Zur theorie der unvollkommenen dielektrika. *Annalen der Physik*, 345(5):817–855, 1913.

[52] CG Koops. On the dispersion of resistivity and dielectric constant of some semiconductors at audiofrequencies. *Physical Review*, 83(1):121, 1951.

[53] RS Devan, YD Kolekar, and BK Chougule. Effect of cobalt substitution on the properties of nickel–copper ferrite. *Journal of Physics: Condensed Matter*, 18(43):9809, 2006.

[54] T Tsurumi and T Harigai. Dielectric and optical properties of perovskite artificial superlattices. In *Handbook of Advanced Dielectric, Piezoelectric and Ferroelectric Materials*, pages 971–1005. Elsevier, 2008.

[55] AMM Farea, Shalendra Kumar, Khalid Mujasam Batoo, Ali Yousef, et al. Influence of frequency, temperature and composition on electrical properties of polycrystalline co0. 5cdxfe2. 5- xo4 ferrites. *Physica B: Condensed Matter*, 403(4):684–701, 2008.

[56] Larry L Hench and Jon K West. Principles of electronic ceramics. 1989.

[57] VL Mathe and RB Kamble. Anomalies in electrical and dielectric properties of nanocrystalline ni–co spinel ferrite. *Materials Research Bulletin*, 43(8-9):2160–2165, 2008.

[58] Dhiren K Pradhan, Pankaj Misra, Venkata S Puli, Satyaprakash Sahoo, Dillip K Pradhan, and Ram S Katiyar. Studies on structural, dielectric, and transport properties of ni0. 65zn0. 35fe2o4. *Journal of Applied Physics*, 115(24):243904, 2014.

[59] DG Chen, XG Tang, QX Liu, YP Jiang, CB Ma, and R Li. Impedance response and dielectric relaxation in co-precipitation derived ferrite (ni, zn) fe2o4 ceramics. *Journal of Applied Physics*, 113(21):214110, 2013.

[60] A Verma, OP Thakur, C Prakash, TC Goel, and RG Mendiratta. Temperature dependence of electrical properties of nickel–zinc ferrites processed by the citrate precursor technique. *Materials Science and Engineering: B*, 116(1):1–6, 2005.

[61] Yuji Noguchi and Masaru Miyayama. Effect of Mn doping on the leakage current and polarization properties in K0.14Na0.86NbO3 ferroelectric single crystals. *Journal of the Ceramic Society of Japan*, 118(8):716–2010, 2010.

[62] G Catalan. Magnetocapacitance without magnetoelectric coupling. *Applied Physics Letters*, 88(10):102902, 2006.

[63] Magnetoelectricity at room temperature in the Bi0.9-xTb xFeO3 system. *Physical Review B - Condensed Matter and Materials Physics*, 69(21):9–11, 2004.

[64] Takuro Katsufuji and H Takagi. Coupling between magnetism and dielectric properties in quantum paraelectric eutio 3. *Physical Review B*, 64(5):054415, 2001.

[65] DH Wang, WC Goh, M Ning, and CK Ong. Effect of ba doping on magnetic, ferroelectric, and magnetoelectric properties in mutiferroic bi fe o 3 at room temperature. *Applied physics letters*, 88(21):212907, 2006.

[66] Raphael Lucas de Sousa e Silva, Prasun Banerjee, and Adolfo Franco Júnior. Functional properties of donor-and acceptor-co-doped high dielectric constant zinc oxide ceramics. *Physical Chemistry Chemical Physics*, 21(18):9456–9464, 2019.

Chapter 4

Study on electronic, magnetic and optical properties on $Ga_{2-x}(Fe_{1-y}Mn_y)_xO_3$, $0 \leq y \leq 0.02$ and $1 \leq x \leq 1.4$ thin films

4.1 Introduction

The field of material science and engineering has changed the modern society through its ability of extraordinary combination of chemical, physical and mechanical properties. Modern technology requires thin films for different applications. Thin film technology is the basic of astounding development in solid state electronics. Due to unique phenomenon of thickness control, geometry and optimization of the films, this technology has advanced many new areas of research in solid-state physics and chemistry. This technology has an extensive applications in diverse fields of electronics, optics, space science, aircrafts, defense etc. in the forms of active devices and passive components such as piezo-

electric devices, micro-miniaturization of power supply, rectification and amplification, sensor elements. Solar energy, magnetic memories, super conduction films, interference filters, reflecting and anti-reflection coatings are another ingenious applications of this technology [1, 2]. In this chapter, structure, surface morphology, magnetic and electric behavior of GFO thin films grown by pulse laser deposition technique will be discussed.

After Remeika synthesized GFO for 1st time in 1960, this material gained a huge scientific attraction. Mishra *et al.* [3] have shown the phase stability of GFO up to a temperature of 1368 K, which opens the possibility to exhibit ferroelectricity up to high temperature. Arima et al [4], at first showed the electric polarization, P_s value ~ 2.5 $\mu C/cm^2$ in a GFO single crystal using neutron diffraction. However, Stoeffler [5] has predicted the P_s value to be 25 $\mu C/cm^2$ computed through electronic structure using first principles. Roy et al, on the other hand has obtained a P_s value of ~ 59 $\mu C/cm^2$ along the b-axis calculated based on first principles with the structure obtained from the minimization of the free energy [6]. Ferroelectricity emerges in GFO mainly due to tilting and distortion of the FeO6 octahedra and the off-centering shift of the Fe ions [3]. In recent studies, S Song et al. [7] has reported net polarization ($2P_r$) of ~ 35 $\mu C/cm^2$ at room temperature, which is

the highest reported experimental value so far. Additionally, the significant activation barrier of 1.05 eV per f. u. is calculated through the Kohn-Sham (K-S) energy as a function of the fractional unit graph with the help of the minimum corresponding ground state K-S energy. This value is $\sim$ 2.5 times larger than $BiFeO_3$ and $\sim$ 20 times larger than $Pb(Zr,Ti)O_3$, making o-GFO superior and stable against thermally activated random dipole switching across the centrosymmetric Pnna barrier [7, 8].

In multiferroics, due to availability of small cross susceptibilities value between different order parameters, the designing of device based on multiferroics is still challenging. However , a giant cross susceptibilities in multiferroics is recently reported that would open the possibilities of practical use of these materials in magneto- and optoelectronics [9]. Although the detailed nature of the multiferroic state differs from system to system, there are several common features. The polar multiferroic state breaks both time reversal symmetry (due to the magnetic order) and spatial inversion symmetry (due to ferroelectric order). This has profound significance for the optical properties of these materials [10]. Multiferroic materials exhibit remarkable optical properties in the absence of external magnetic field. In 2006, Rai *et al* [11] have measured the non-linear optical response in $YMnO_3$ showing

the strong coupling between ferroelectric and antiferromagnetic domain walls indicating strong coupling between the magnetic and ferroelectric structure in the system. This also suggests an approach for incorporating multiferroics into optical devices. The domain structure modification through external magnetic and/or elelctric fields could provide a method for tuning the non-linear optical response in these system [10]. These effects has been observed in $HoMnO_3$ producing a change in second harmonic generation signal by modifying magnetic structure through electric field [12], and recently Bi_2FeCrO_6 showed enormous change in second harmonic generation response in an applied magnetic field [13]. It is suggested that a spatial variation in the toroidal moments (across a domain wall) produces the optical equivalent of Lorentz force on the light. This directional dependent optical path would lead to non-reciprocal refraction through domain walls [14]. This effect could be utilized to produce novel optical devices. Investigation on magnetization induced second harmonic generation (MSHG), X-ray directional dichroism in single crystal [15, 16] and later observation of large second-harmonic kerr rotation in GFO thin films on YSZ buffered Si [17] shows the material to be potential candidate for magneto-optical applications as well.

4.2 Experimental details:

Highly oriented gallium ferrite $Ga_{2-x}(Fe_{1-y}Mn_y)O_3$, $0 \leq y \leq 0.02$ and $1 \leq x \leq 1.4$ thin films of thickness ~ 250 nm were grown on strontium ruthenate (SRO) buffered (111) strontium titanate (STO) by pulsed laser deposition (PLD) method. An excimer laser of KrF with $\lambda = 248$ nm is used in PLD. A buffer SRO layer of thickness ~ 30 nm were deposited on highly cleaned STO (111) substrates by the PLD method. The parameters used to deposit SRO and $Ga_{2-x}(Fe_{1-y}Mn_y)O_3$ are given in table 4.1. For all deposition, oxygen is used as carrier gas with base pressure maintained at x 10^{-6} Torr.

Table 4.1: Parameters used in deposition process

	Energy density (J/cm^2)	Frequency (Hz)	Substrate temp °C	Oxygen deposition pressure (Torr)	Cooling rate
SRO	1.5	10	680	200	5°C/min
$Ga_{2-x}(Fe_{1-y}Mn_y)O_3$	2	5	725	300	2°C/min

Prior to deposit thin films, the STO substrates were kept for sonication in acetone medium for about 10 mins. Then the samples were subjected to oxygen plasma-etching at a power of 30 W under a pressure of 200 mTorr for ultrahigh cleaning i.e., to remove any organic impurities from the surface. The thickness of the sample was checked by an Ambios Tech XP-200 profilometer. Surface morphology and

piezoresponse of the samples were studied by a Veeco Nanoscope V atomic force microscope (AFM) and piezo-response force microscope (PFM). Magnetic measurements were done utilizing the quantum Dynacool PPMS. Platinum (Pt) top electrodes of area $\sim$ 110 x 110 μm^2 were deposited through a shadow mask to form a Pt/GFO/SRO (MIM) capacitor for electrical measurements. The Sawyer Tower test configuration (Radiant Technologies Model RT 6000 HVA-4000 V) was used to record remnant polarization and coercive field of the prepared capacitor.

4.2.1 X-Ray Diffraction study

Figure 4.1(a) shows the XRD patterns of bare STO substrate along with $Ga_{2-x}(Fe_{1-y}Mn_y)_xO_3$ films deposited on SRO buffered STO. The schematic diagram of $Ga_{2-x}(Fe_{1-y}Mn_y)_xO_3$ thin films are deposited on strontium titanate (STO) (111) substrate buffered with strontium ruthenite (SRO) is shown in figure 4.1(b). The wide range of the θ-2θ scan (10° - 90°) showed the peaks only at (*0k0*) direction (in $Pc2_1n$ setting) and those from substrates in all films, figure 4.1(a). This suggests the deposition of thin films are highly oriented. From this graph, we calculated the lattice parameter of the the films, using Bragg's law, $2d\sin\theta = n\lambda$, where d, n, and λ are the interplanar spacing, reflec-

tion order, and wavelength. The lattice parameter (k value) of GFO1 was obtained as 9.433 Å which was slightly increased upon Fe and Mn doping. The value raised to 9.44 for GFMO3.

On the other hand, the STO substrate exhibits a cubic crystal structure with a lattice constant a = 3.905 Å. The bulk SRO is arranged in an orthorhombic lattice, but it is often described as a pseudo-cubic unit cell with a lattice parameter of 3.93 Å due to its small distortion of the octahedral structure [18]. With this value, the lattice misfit between substrate and SRO is calculated as -0.64%. Generally, STO (111) substrates have a hexagonal platform, figure 4.1(c). For this, the best possible alignment of the thin film is on two-unit cells of SRO (111) during the growth of GFO film, with the possibility of three domain growth as shown in figure 4.1(c). The compressive strain of the film was calculated using the equation

$$\epsilon = \frac{a_{bulk} - a_{film}}{a_{bulk}} X100 \tag{4.1}$$

and observed as 0.46% out-of-plane strain. (here, a_{bulk} = 9.389 Å) [19]. SRO (111) bottom electrode is chosen due to its compatibility with hexagonal STO (111) substrate along with fatigue and imprinting resistance.

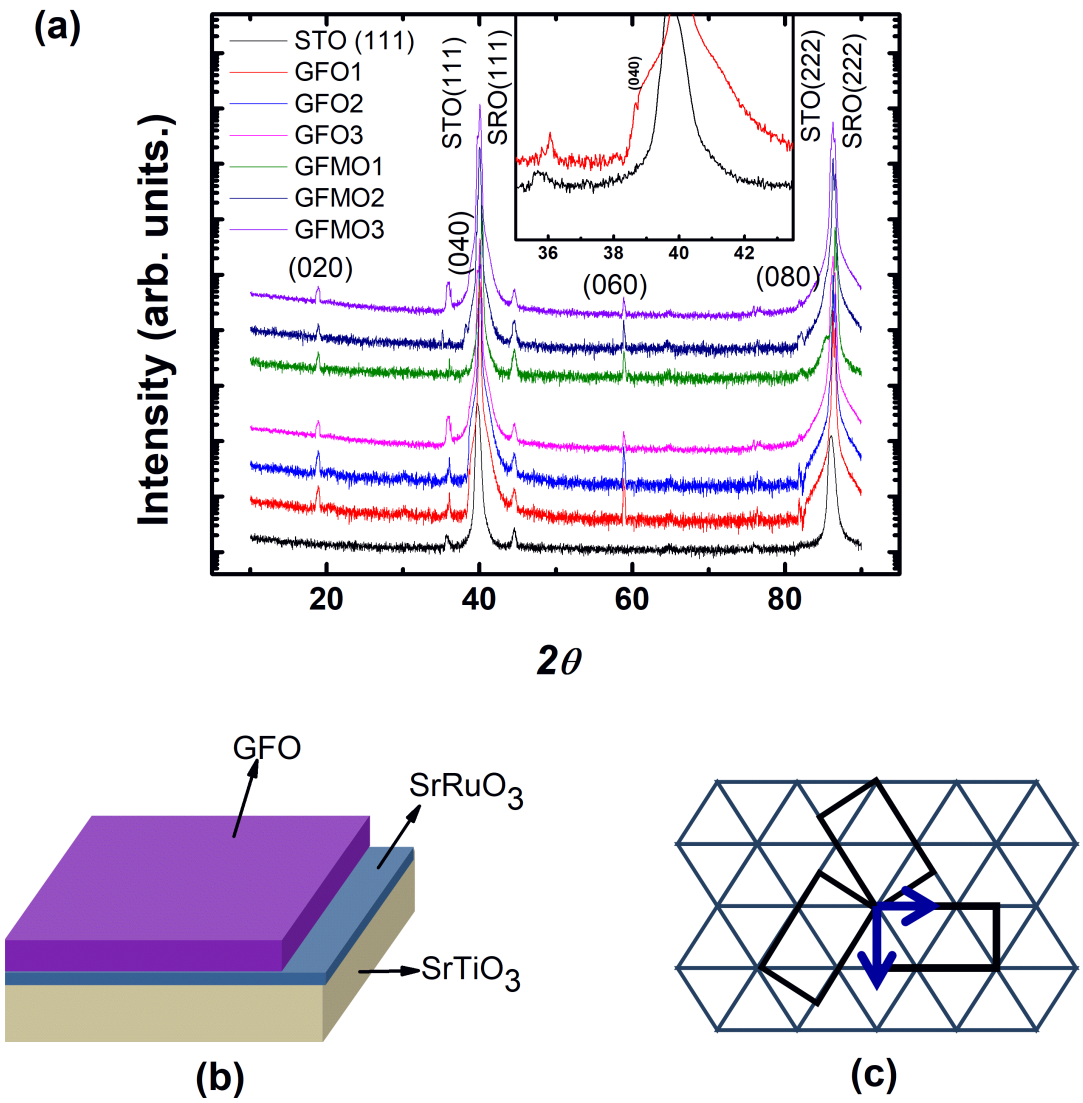

Figure 4.1: (a) XRD pattern of $Ga_{2-x}(Fe_{1-y}Mn_y)O_3$ recorded from 10° - 90° at RT, (b) Schematic diagram of thin films with buffered layer SRO on substrate STO, and (c) Possible alignment of film growth on STO substrate

4.2.2 Atomic Force Microscopy

The uniformity of the surface was analyzed by AFM. The microscopic AFM image of STO/SRO/ $Ga_{2-x}(Fe_{1-y}Mn_y)_xO_3$ thin films are shown in figure 4.2. The surface topography captured by AFM in the contact mode on a scan size of 3 x 3 μm^2, appeared to be homogeneous and smooth. It is seen in the images that the deposited films lack granular structure and are free of microcracks, pores or holes. The average surface roughness (R_a) of films are found to be 2 - 4 μm. The smooth surface with low roughness is required for improvement of multifunctional properties [20, 21, 22].

4.2.3 Magnetic properties

Magnetization versus temperature (M-T) plots for all films collected at both field cooled (FC) and zero field cooled (ZFC) are shown in figure 4.3. All samples are cooled at 0.1 T and also measured at 0.1 T. All samples showed thermomagnetic irreversibility and undergone paramagnetic phase change at temperature 250 - 350 K. It is observed that with increase in Fe contents, magnetic transition temperature, T_C is increased, however doping Mn reduced T_C slightly. With Mn-doped samples, the plausible interchange of Fe^{3+} - O^{2-} - Fe^{3+} networks into Mn^{3+} - O^{2-} - Mn^{3+} and Fe^{3+} - O^{2-} - Mn^{3+} and their super-exchanges

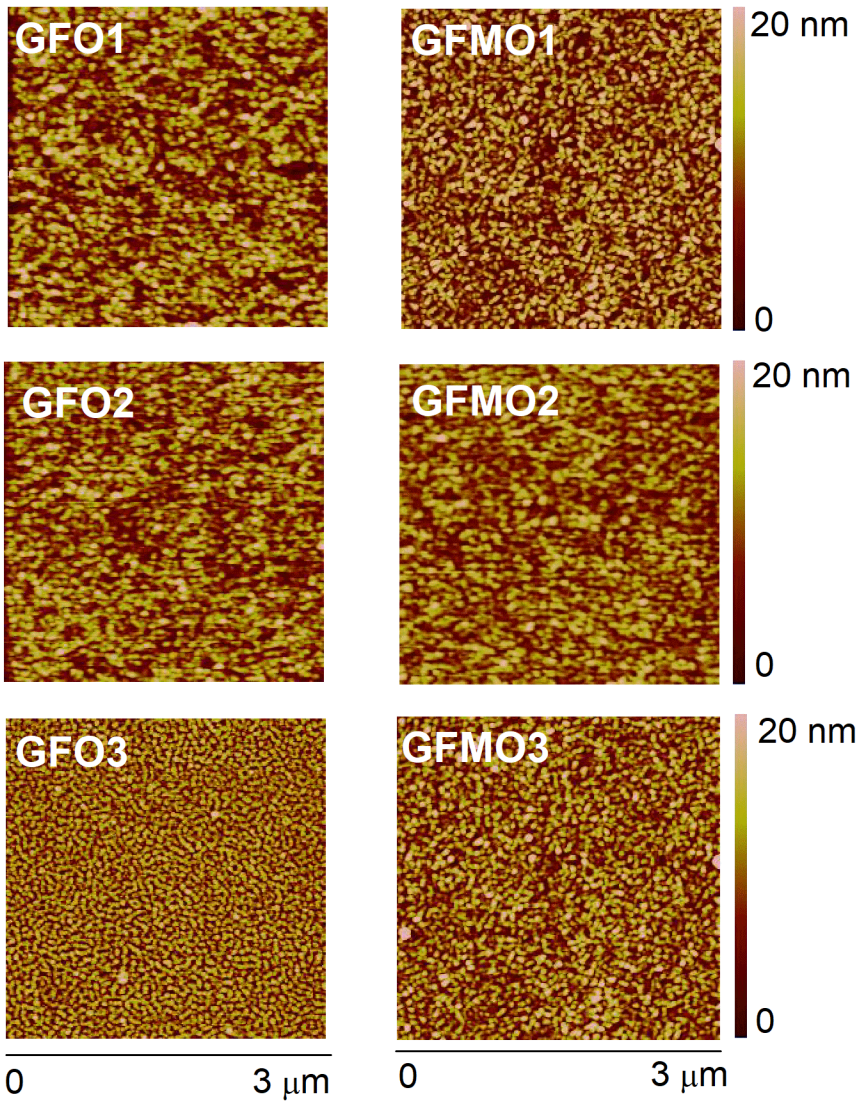

Figure 4.2: AFM image of $Ga_{2-x}(Fe_{1-y}Mn_y)_xO_3$ films scanned at 0-20 nm height and 1 - 3μm

lead to decrease in Fe-Fe linkage that cause the reduction in T_C. It can be noted here that the reduction in T_C is not significant in our case unlike the previous on Mn substituted perovskite [23]. It is due to low quantities of Mn substitution ($\sim$ 2%) in our study. Another finding of this experiment was that the bifurcation between FC and ZFC was larger than that in ceramics with same field applied. A rounded maximum, T_{max} (hump) in the ZFC curve is seen for all cases. T_{max} is related to the blocking of the particles with the mean particle size. For noninteracting particles, T_{max} is proportional to blocking temperature, T_B, with proportionality constant b = 1 - 2, depending on the type of size distribution [24, 25, 26]. The rounded peak maxima in our case suggests the well-defined value for T_B illustrating a narrow distribution of particle sizes and hence of energy barriers. The magnetic hysteresis loops of GFO measured at the field range of +/- 2T carried at various temperature 10 - 400 K is shown in Figure 4.4. The coercive field (H_C) and saturation magnetization (M_S) decreases gradually with the increase of temperature and vanished at 250 K for GFO1. This value increases upto 350 K for Fe and Mn doped GFO, (GFMO3). At higher temperature, the spin are disordered due to thermal energy causing the disappearance of H_C and M_S that shows ferrimagnetic-paramagnetic phase transition. The phase transition T_C in thin films is obtained at

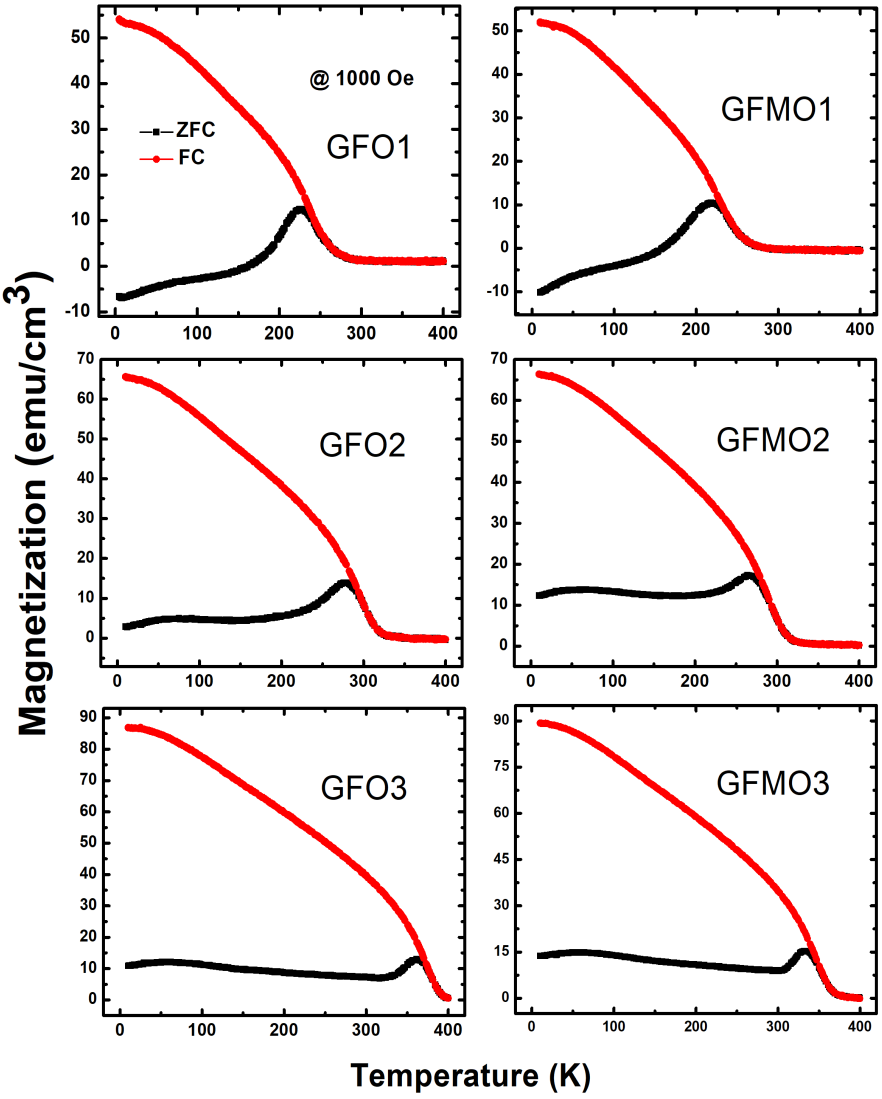

Figure 4.3: Magnetization as a function of temperature measured at 100 Oe

slightly higher temperature than in bulk ceramics. This could be due to the strain at SRO/GFO interface. These properties of higher T_C in thin film in comparison to bulk has been reported theoretically and experimentally [27, 28]. On increasing Fe concentration, the magnetization of the film increases. However, with Mn co-doping, magnetization

decrease slightly compared to their parent element. According to Neel's

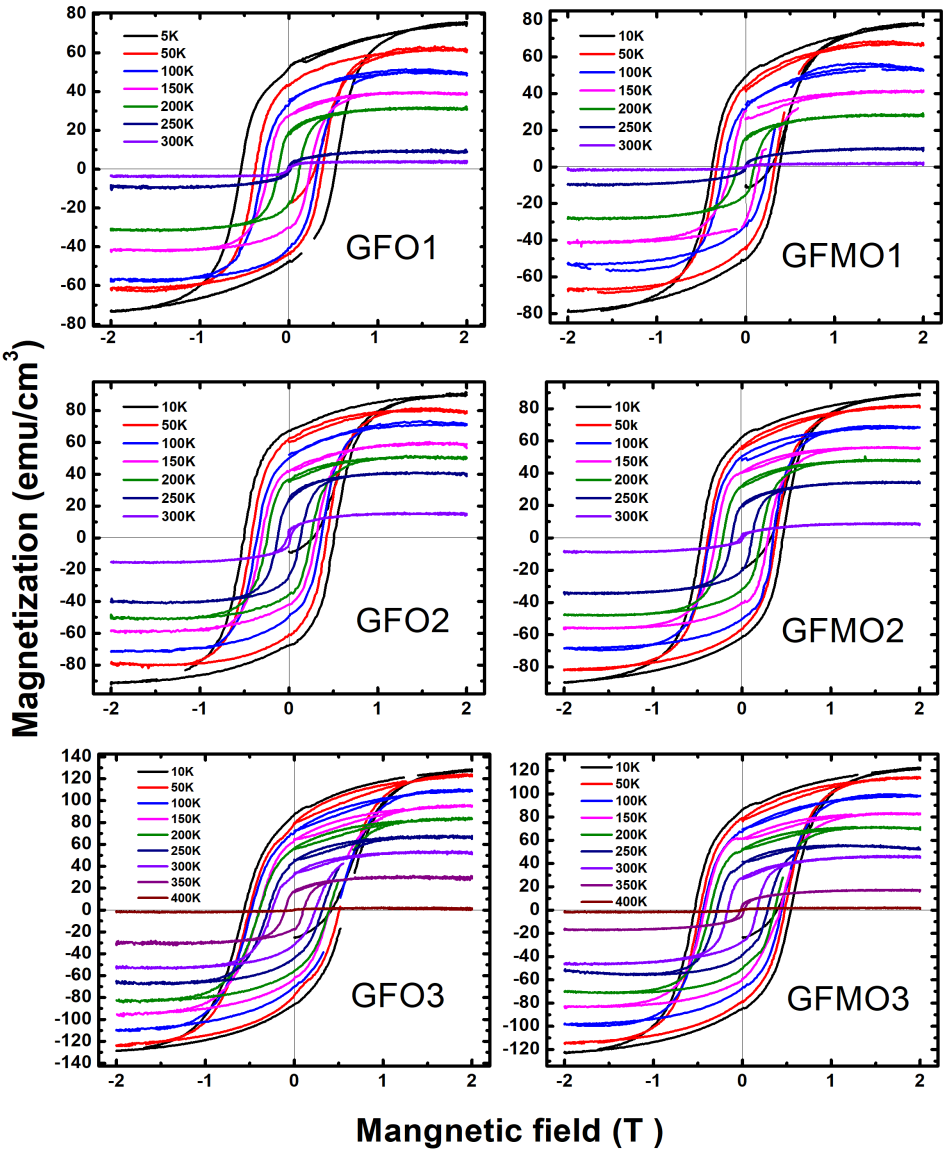

Figure 4.4: Magnetization as a function of field measured at various temperature.

two sublattice theory for ferrimagnetism [29], the sublattice magnetizations M_A and M_B are antiparallelly aligned and the total magnetization given by $M_S = M_C$ - M_A. On Mn addition, the replacement of Fe^{3+}

(5μB) in octahedral sites by Mn^{3+} (4μB) would decrease the net magnetic moment in B sites that weaken the AB superexchange interaction between the two antiparallel magnetic sublattices [30] reducing the total magnetization. When the iron concentration is increases, the excess iron ions will be deposited at tetrahedral (T_d) sites and the directions of Mn and Fe spins at T_d sites are antiparallel to each other resulting in reduced magnetization of sublattice A [31].

4.2.4 Piezoelectric force microscopy

$GaFeO_3$ is known as RT piezoelectric material, however its magnetic transition temperature (Tc) is below RT. From magnetization study of various component of GFO, it is observed that GFO3 and GFMO3 have T_C above room temperature, as shown in figure 4.3. In order to confirm RT multiferroics, we probe a ferroelectric property on these two compounds, as well as on the principle compound GFO1. Piezoresponse force microscopy (PFM) is an ideal tool to characterize the ferroelectricity for both probing and switching the local ferroelectric polarization at nanoscale [32]. Figure 4.5 shows amplitude and phase patterns written on the GFO1, GFO3, and GFMO3 with the application of electric field via a conducting tip. A tip bias of +12 V was applied to pole the 6 μm $\times$ 6 μm square region, followed by another poling with a tip bias

of -12V in the central area of 4 μm x 4 μm. The total surface scan for GFO3 and GFMO3 was 10 μm for GFO1 and GFO3, and 8 um for GFMO3. The clear contrast area seen on applying different voltages indicates domain switching behavior due to ferroelectric nature of the films [33, 34]. GFMO3 shows higher roughness overall. This is due to a large grain size of it's ceramic. The growth parameter during film deposition also might affect the roughness of the film. This result suggests that polarization of GFO layer is switchable, confirming the ferroelectric nature of the heterostructure.

4.2.5 Ferroelectric properties

Ferroelectricity of thin film was tested with polarization vs electric field (P-E) hysteresis loop measurement. We conduct this experiment on GFO3 and GFMO3, (which has T_C > RT) along with principle compound GFO1. Figure 4.6 reveals the RT P-E loops observed on $Pt/Ga_{2-x}(Fe_{1-y}Mn_y)_xO_3$/SRO thin-film capacitor at frequency 10 kHz. In GFO1, we found remanent polarization of ~ 30 $\mu C/cm^2$ and coercive field (E_C) of 0.09 MV/cm. This value is slightly lower than earlier reported value [7] and is similar to [35]. On increasing Fe concentration, breakdown field is decreased. It is because, as Fe increases, leakage in the compound increases. As a result, P-E graph is deviated away from

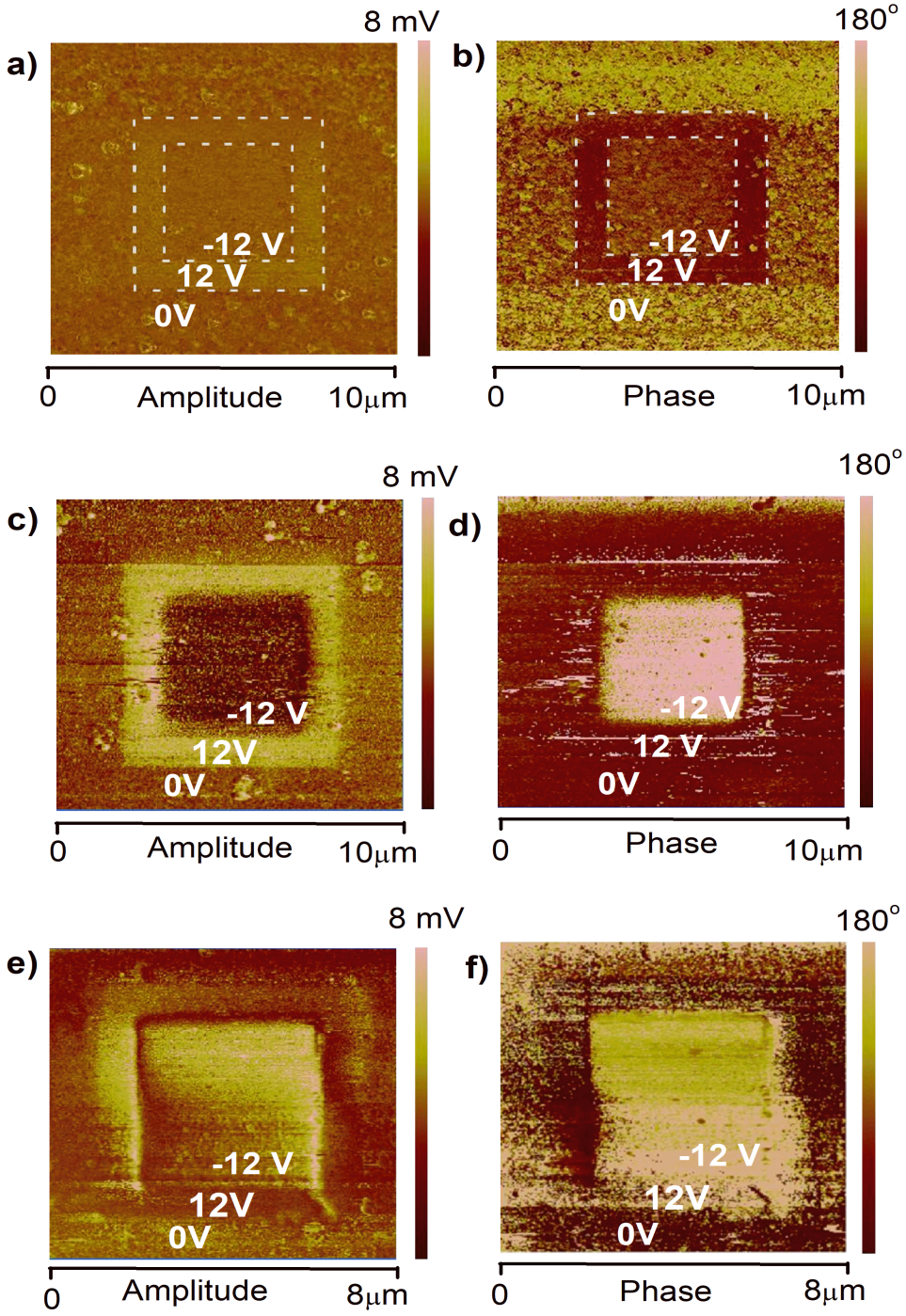

Figure 4.5: Piezoresponse force microscopy; a and b, c and d, e and f are amplitude and phase images of GFO1, GFO3 and GFMO3 respectively.

saturation, as seen in figure 4.6(b). The curve tends to saturate on Mn inclusive compound fig 4.6(c). However, none of curves aren't completely saturated. This unsaturated behavior of P-E loops observed is believed to be relatively due to the leaky nature of the current, which is typical for multiferroics [35, 36].

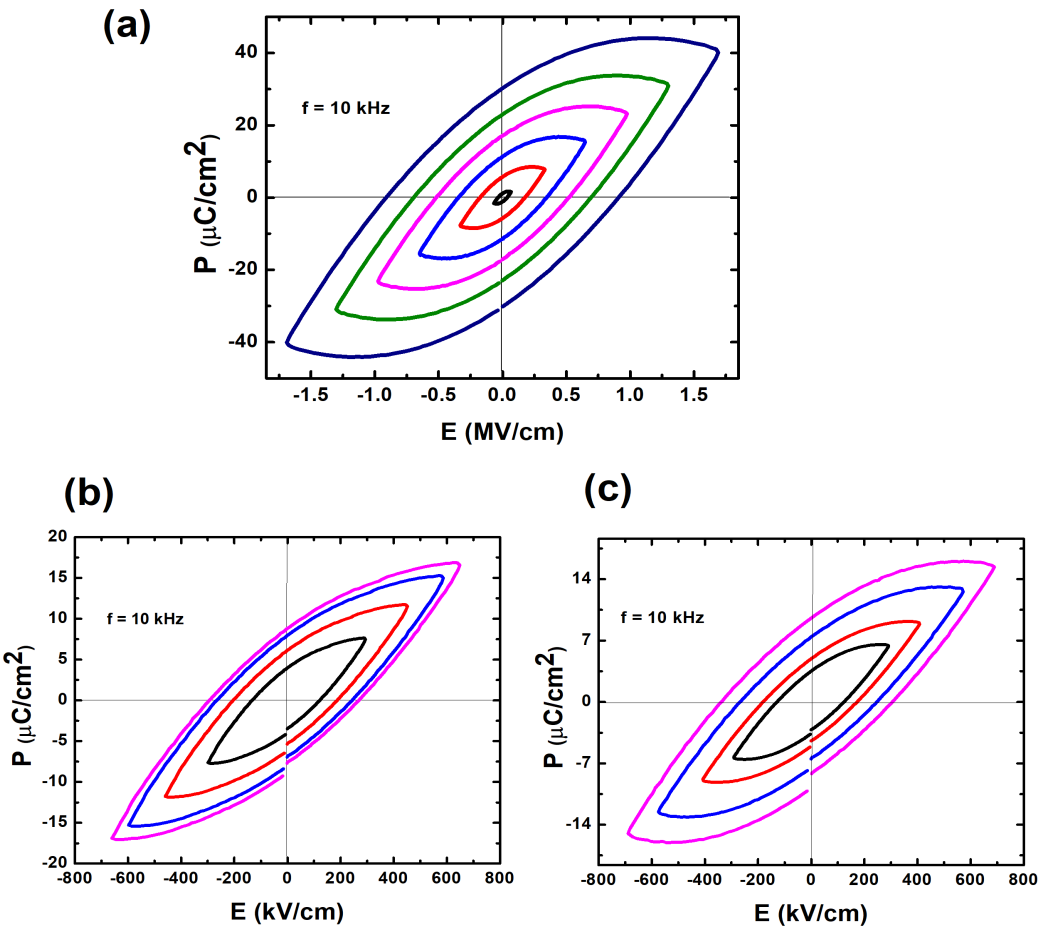

Figure 4.6: Polarization versus electric field plot of (a) GFO1, (b) GFO3 and (c) GFMO3 measured at RT.

4.2.6 Dielectric properties of $GaFeO_3$

For further understanding of electronic nature of the film, permittivity vs. temperature is carefully studied on $GaFeO_3$. Figure 4.7 shows the RT permittivity and dielectric loss w.r.t frequency. The permittivity (ϵ_r) decreases with an increase in frequency, indicating the presence of large dispersion due to Maxwell-Wagner type interfacial polarization. The rapid decrease in ϵ_r at a lower frequency than at higher frequency elucidate that the film is slightly leaky in nature that is supported by P-E loop as well. This is further clarified by dielectric loss graph showing the value of ~ 1.2 at 100 Hz which decreased to 0.2 at 1 MHz. The frequency and temperature variation of the dielectric constant of GFO thin film is shown in figure 4.7(b). With increase in temperature, ϵ_r increases in all frequency regime and reach the maximum permittivity (ϵ_m) and then decreases. The peak temperature (T_m) where permittivity is maximum, is shifted from 471 K to 563 K over the frequency range of 100 Hz to 1 MHz. This indicates the compound is deviated from normal ferroelectric. Such type of diffused and frequency dispersive maxima of temperature-dependent permittivity indicates the presence of relaxation type behavior in a material called as relaxor [37][32]. In a dielectric material, thermal motion regulates the dielectric relaxation process and the temperature dependence of relaxation time (τ)

follows the Arrhenius law. However, relaxation time usually follows Vogel-Fulcher (V-F) relation more precisely than Arrhenius law in case of relaxor like behavior. Hence, to analyze the relaxation characteristics of the film, the maximum dielectric constant is plotted with (V-F) model [38] given by

$$f = f_o exp \frac{-E_a}{k_B(T_m - T_f)} \tag{4.2}$$

that describes the relation similar to that recognized for glasses [39]. Here, f and f_0 is the measured frequency and the attempt frequency which is related to the cut-off frequency of the distribution of relaxation times. E_a, k_B, T_m and T_f are activation energy, Boltzmann constant, and peak temperature and freezing temperature, respectively. Below freezing temperature, the dynamic reorientation of the dipolar cluster polarization is not thermally activated. On fitting the experimental values to the above equation, as shown in Figure 4.7(c), we obtain the values as $f_0 = 4.13 \times 10^{13}$ Hz, $T_f = 274$ K, $E_a = 0.39$ eV. This activation energy, E_a, is a measure of the energy barrier that separates metastable states in the system [21]. The E_a value obtained is analogous to the earlier reported GFO films [40]. The diffuseness of phase transition on relaxor can be described by a modified Curie-Weiss law with the

relation,

$$\frac{1}{E_r} - \frac{1}{E_m} = \frac{(T - T_m)^\gamma}{C'} \tag{4.3}$$

γ is diffuseness coefficient that shows the character of the phase transition and limits between $1 \leq \gamma \leq 2$. γ approximate to 1 for normal ferroelectrics and 2 for pure relaxor.C' is a constant quantity. Figure 4.7(d) shows the plots of $\ln(\epsilon_m/\epsilon_r - 1)$ vs ln (T-T_m) at 10 kHz and 1MHz. The value of γ is found to be 1.95 and 1.96 for 10 kHZ and 1 MHz respectively. This values of γ clarifies that the compound exhibits diffuse phase transition with disordered crystals which occurred due to the existence of different states of polarization and hence different relaxation times in different regions [37, 41]. The diffuseness appears mainly because of compositional fluctuations and/or due to structural disorder in the lattice [37]. This could be correlated with the prevailing disorder between Fe/Ga cations in GFO due to their isovalent and close ionic radii [42]. In Figure 4.7(b), after peak temperature, it is noticed that the curve tends to deviate from their regular smooth pathway on decreasing temperature. This tendency of forming secondary peaks are seen in all frequency. These incomplete peaks are observed in all curves and are shifted to higher temperature with increasing frequency. Here we write the first dielectric relaxation as R-1 (peak at temperature region) and second dielectric relaxation as R-2 (peak at higher temper-

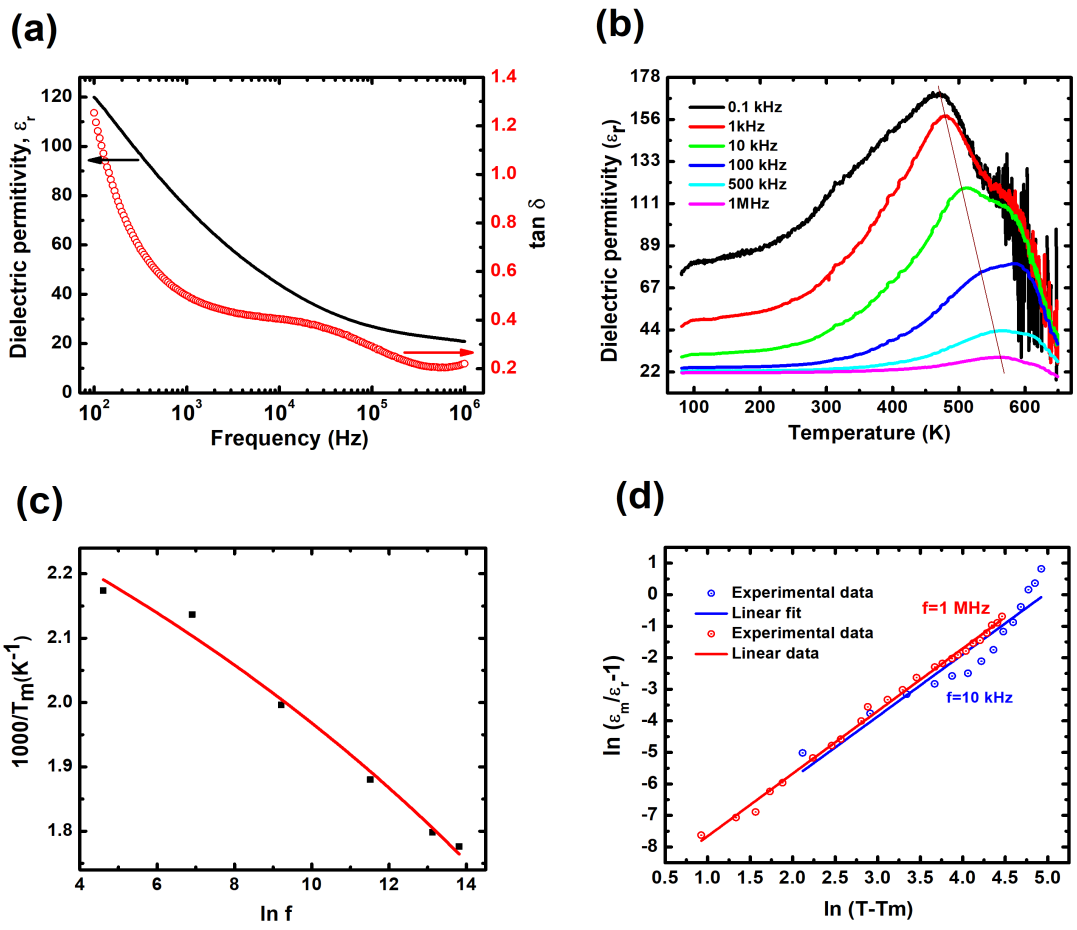

Figure 4.7: (a) Room temperature dielectric permittivity (ϵ_r) and tanδ w.r.t frequency, (b) Permittivity at various temperature and frequencies, solid brown line indicating the shifted peak temperature from lower frequency to higher frequency (c) Voger-Fulcher fit of frequency dispersion of the dielectric maximum, 1000/T_m versus lnf, (d) Modified Curie-Weiss law for GFO thin film, ln(ϵ_m/ϵ_r-1) vs ln (T-T_m).

ature region). The dielectric anomaly in R-1 indicates the transition from ferroelectric to relaxor ferroelectrics state (F-R), hence the Vogel-Fulcher relation was studied on this region. This behavior agrees with previous studies on relaxor type materials [43]. The polar nanoregions (PNRs) begin to establish at this region R-1 where the ferroelectric

long range order is destroyed, giving rise to a secondary peak (R-2) with wide dispersion of dielectric permittivity with frequencies. Hence, there occured the incomplete formation of secondary diffused phase transitions with different relaxation times [44]. This might be due to thermally excited charge carriers at high temperature end [45].

4.2.7 Photo-detector properties on GFO1

Photo-detectors are useful sensing devices with a wide range of applications including space communications, UV detection, and chemical and biological sensing [46]. In order to investigate the photo-response, we measured the current-voltage (I-V) curve of the GaFeO3 (GFO1) system under dark condition and under light illumination of 1 sun (AM 1.5G) over a voltage range of -10 V to 10 V. Under the solar illumination, the photocurrent of the device is determined to be $1.955\text{x}10^{-3}$ A while the dark current was $1.023\text{x}10^{-3}$ A at 5V, shown in figure 4.8. The substantial non-linear dependence of current as a function of voltage indicates a good double-schottky contact behavior between platinum electrode and the GFO thin film, which agrees well with the theoretical band structure calculation [47]. The higher electrical conductivity observed with light intensity can be explained in terms of the excess of charge carriers generated by photoexcitation by photon

energies above and close to E_g of the dielectric. The electrons being excited from the valence band to conduction band are transferred to the adjacent interfaces by the electrodes. To investigate the device's reliability, the time dependent photoresponse and recovery time was demonstrated by switching light ON and OFF for each 50 seconds at bias of 0V, -5V and 5V as shown in figure 4.8(b-d). It can be seen that the I-t curve changes as the solar light turned ON and OFF. We haven't achieved a large switching ratio, however, the device shows the photoresponse properties. The quality might be increased by fabricating the defect free systems both in films and electrodes. The reliability of the device is checked by studying current vs time graphs. Identical currents rises and the recoveries observation over the course of cycles indicate good reliability. On applying electric field, the excitons split into electrons and holes at the interface region of GFO/SRO and then the electrons at conduction band of the GFO is transferred to SRO. The low electrical resistivity of SRO (2.0 x 10^{-4} ohm cm at 300 K) [48] facilitates to reduce the resistance of the heterojunction structure, which enhances the electron-hole separation and improves the carrier transport in the heterojunction. When light is OFF the excess electrons from the SRO transfer into the film where they recombine with the holes increasing the resistance [49], as shown in figure 4.8(c). Similar trend

is observed for opposite polarization confirming the photoresponse of the Pt/GFO/SRO heterostructure.

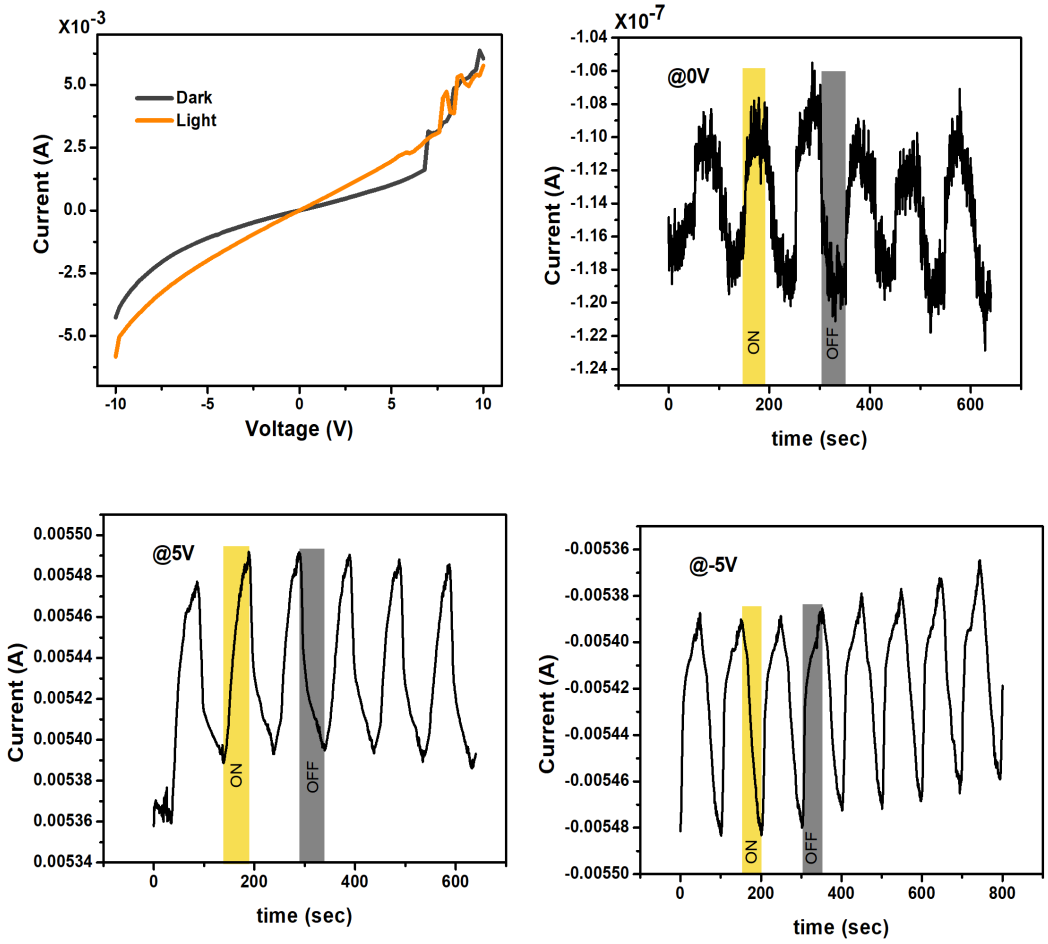

Figure 4.8: Photodresponse of GFO. (a) I-V graph obtained at dark and under illumination of white light of 1 sun (AM 1.5G), (b) , (c), and (d) are the I-t curves measured at 0V, 5V and -5V, showing switching of current on light ON and OFF condition confirming photoresponse in the film.

4.3 Optical Properties of $Ga_{2-x}(Fe_{1-y}Mn_y)_xO_3$ grown on fused silica

To study the optical characteristics of the films, $Ga_{2-x}(Fe_{1-y}Mn_y)_xO_3$ thin films are grown in fused silica. The parameters used were same as above mentioned. The optical properties of the samples are characterized using a UV visible spectrometer. Figure 4.9 shows the transmittance of thin films in the wavelength range 300 - 800 nm deposited on fused silica. The films are highly transparent with transmittance of ∼85% in the range 600-800 nm in all films revealing the excellence optical transparency. The absorption coefficients (α) can be calculated using the equation

$$\alpha = \frac{1}{d} ln \frac{1}{T} \tag{4.4}$$

where d is the thickness of the film and T is its transmittance respectively. In general, α is related to the photon energy derived from Tauc relation $\alpha h\nu = A(h\nu\text{-}E_g)^n$ where h is the planck contant; ν is the photon frequency; A is a constant corresponding to electron-hole mobility; E_g is the band gap, and n is a ratio which characterizes the type of optical transition in the material (n=2, 1/2, 2/3, or 1/3 corresponding to allowed direct, allowed indirect, forbidden direct and forbidden indirect) respectively. Direct and indirect band gap (E_g) of the sys-

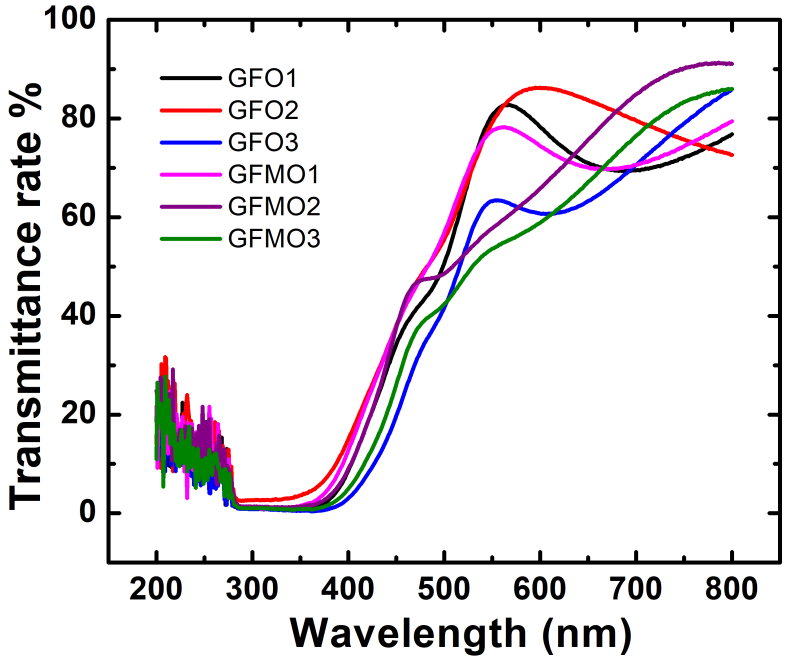

Figure 4.9: Transmittance rate of $Ga_{2-x}(Fe_{1-y}Mn_y)_xO_3$ thin films deposited in fused silica

tem is analyzed by studying the optical characteristics of thin films with $\alpha h\nu^2$ and $\alpha h\nu^{(1/2)}$ against $h\nu$ respectively. Figure 4.10 depicts the direct band gap characteristics of the films. The E_g values were found by extrapolating the linear region in the absorption edge region to zero at x-axis. On increasing Fe contents, a red shift in the band gap is observed. However, with Mn co-doping significant bandgap shift isn't observed with respect to their parent compounds, i.e. E_g value of GFMOn is similar to E_g value of GFOn.

The reduction in bandgap with Fe concentration could be due to complex interplay between excess Fe^{3+} electronic levels mediated by

oxygen through super-exchange interaction. Basically, the ferrimagnetically [50] coupled Fe^{3+} induce a spin disorder on oxygen which can enhance the broadening of oxygen p-orbitals and valence band edges of Fe^{3+} revealing the small band-gap [51, 52]. It can be explained in terms of the energy level shift of Valence band maxima (VBM) and conduction band Minima (CBM). The VBM shifts due to the hybridization of d-orbitals of Fe with p-orbitals of oxygen in the valance band [53]. S. George *et al* [54] reported that the increase in Fe content in TiO_2 lowers the band gap energy due to creation of trap levels between conduction and valence bands of TiO_2. On adding Mn, no significant change in bandgap is observed.

Additionally, we also observed the indirect band gap of the films, shown in figure 4.11. Normally, indirect bandgap appears due to creation of defect levels and oxygen vacancies. Indirect band gap usually originates due to intrinsic oxygen vacancies/defect which might be created due to metastable states of Ga^{2+}/Ga^{3+} in our case. The indirect band gap observed was 2.4 eV for undoped GFO which decreased to 2.15 eV with high Fe concentration. These observations of reduction in E_g with Fe addition and also observation of indirect band gap shows the potential application of the material in optical devices.

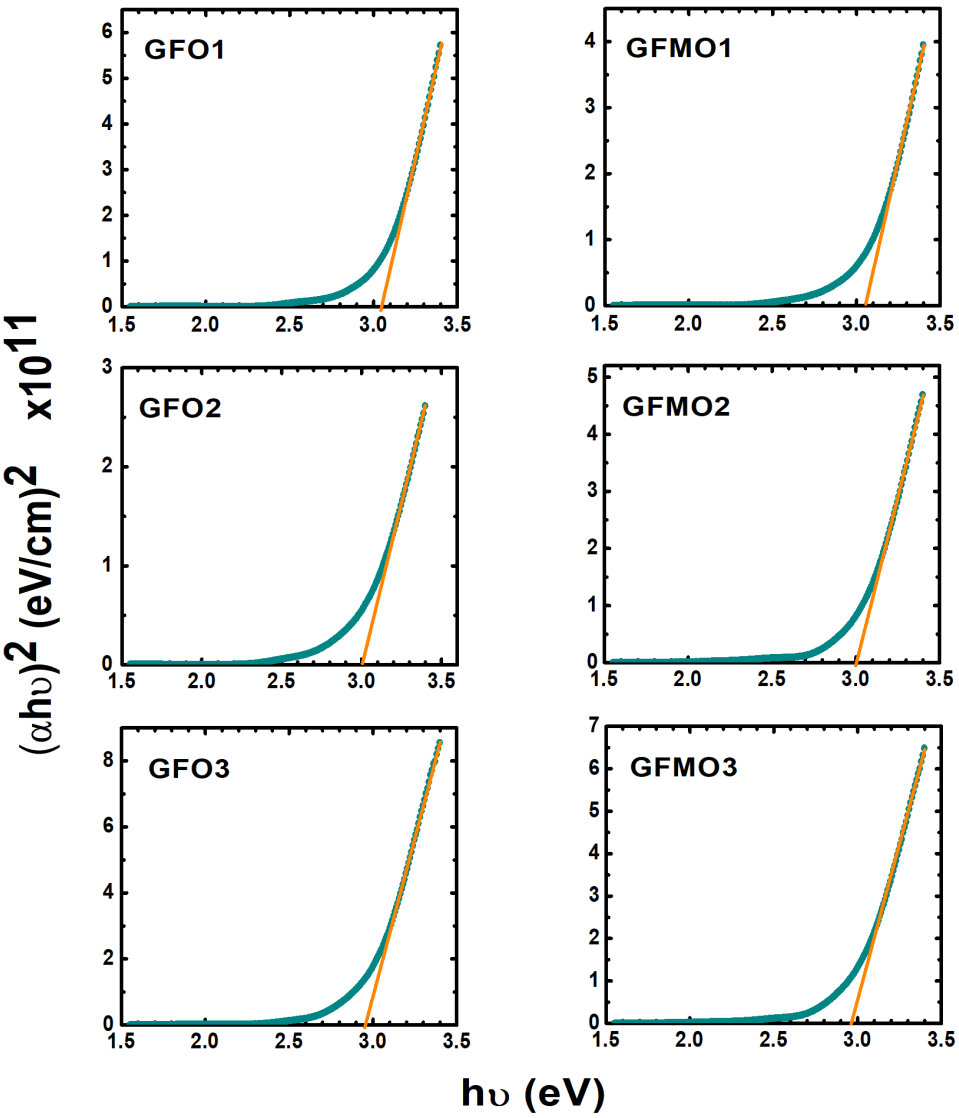

Figure 4.10: Direct band gap of GFO shows red shift on increasing Fe concentration and Mn co-doped samples

Bibliography

[1] AR West. 'solid state chemistry'john willey & sons, 2003.

[2] MC Rao and MS Shekhawat. A brief survey on basic properties of thin films for device application. In *International Journal of Modern Physics: Conference Series*, volume 22, pages 576–582. World Scientific, 2013.

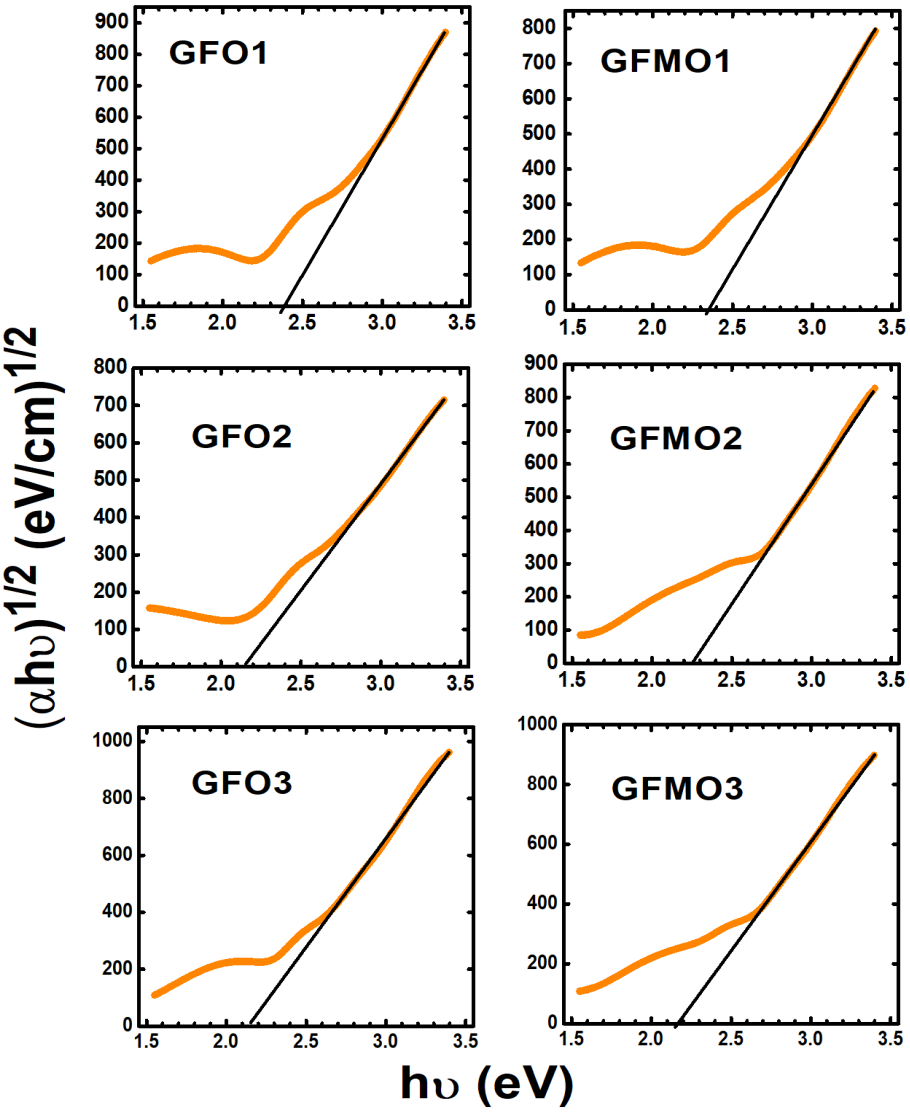

Figure 4.11: Indirect bandgap

[3] S. K. Mishra, R. Mittal, Ripandeep Singh, M. Zbiri, T. Hansen, and H. Schober. Phase stability of multiferroic GaFeO3 up to 1368 K from in situ neutron diffraction. *Journal of Applied Physics*, 113(17):1–6, 2013.

[4] T Arima, D Higashiyama, Y Kaneko, JP He, T Goto, S Miyasaka, T Kimura, K Oikawa, T Kamiyama, R Kumai, et al. Structural and magnetoelectric properties of ga 2- x fe x o 3 single crystals grown by a floating-zone method. *Physical Review B*, 70(6):064426,

2004.

[5] Daniel Stoeffler. First principles study of the electric polarization and of its switching in the multiferroic GaFeO 3 system. *Journal of Physics Condensed Matter*, 24(18):185502, 2012.

[6] Amritendu Roy, Somdutta Mukherjee, Rajeev Gupta, Sushil Auluck, Rajendra Prasad, and Ashish Garg. Electronic structure, Born effective charges and spontaneous polarization in magnetoelectric gallium ferrite. *Journal of Physics Condensed Matter*, 23(32):325902, 2011.

[7] Seungwoo Song, Hyun Myung Jang, Nam Suk Lee, Jong Y. Son, Rajeev Gupta, Ashish Garg, Jirawit Ratanapreechachai, and James F. Scott. Ferroelectric polarization switching with a remarkably high activation energy in orthorhombic GaFeO3 thin films. *NPG Asia Materials*, 8(2):e242–9, 2016.

[8] P. Ravindran, R. Vidya, A. Kjekshus, H. Fjellvåg, and O. Eriksson. Theoretical investigation of magnetoelectric behavior in BiFe O3. *Physical Review B - Condensed Matter and Materials Physics*, 74(22):224412, 2006.

[9] A. M. Kalashnikova, R. V. Pisarev, L. N. Bezmaternykh, V. L. Temerov, A. Kirilyuk, and Th Rasing. Optical and magneto-optical studies of a multiferroic GaFeO3 with a high curie temperature. *JETP Letters*, 81(9):452–457, 2005.

[10] Gavin Lawes. Commentary: Optical properties of magnetoelectric multiferroics. *Journal of Nanophotonics*, 2(1):020306, 2008.

[11] M. Fiebig, Th Lottermoser, D. Fröhlich, A. V. Goltsev, and R. V. Pisarev. Observation of coupled magnetic and electric domains. *Nature*, 419(6909):818–820, 2002.

[12] CC Homes, SV Dordevic, M Strongin, DA Bonn, Ruixing Liang, WN Hardy, Seiki Komiya, Yoichi Ando, G Yu, N Kaneko, et al. A universal scaling relation in high-temperature superconductors. *Nature*, 430(6999):539–541, 2004.

[13] Sheng Ju and Guang-Yu Guo. Colossal nonlinear optical magnetoelectric effects in multiferroic bi 2 fe cr o 6. *Applied Physics Letters*, 92(20):202504, 2008.

[14] Kei Sawada and Naoto Nagaosa. Optical magnetoelectric effect in multiferroic materials: Evidence for a lorentz force acting on a ray of light. *Physical review letters*, 95(23):237402, 2005.

[15] M. Kubota, T. Arima, Y. Kaneko, J. P. He, X. Z. Yu, and Y. Tokura. X-ray directional dichroism of a polar ferrimagnet. *Physical Review Letters*, 92(13):2–5, 2004.

[16] Y. Ogawa, Y. Kaneko, J. P. He, X. Z. Yu, T. Arima, and Y. Tokura. Magnetization-Induced Second Harmonic Generation in a Polar Ferromagnet. *Physical Review Letters*, 92(4):4, 2004.

[17] Darshan C. Kundaliya, S. B. Ogale, S. Dhar, K. F. McDonald, E. Knoesel, T. Osedach, S. E. Lofland, S. R. Shinde, and T. Venkatesan. Large second-harmonic kerr rotation in GaFeO3 thin films on YSZ buffered silicon. *Journal of Magnetism and Magnetic Materials*, 299(2):307–311, 2006.

[18] Gertjan Koster, Lior Klein, Wolter Siemons, Guus Rijnders, J. Steven Dodge, Chang Beom Eom, Dave H.A. Blank, and Malcolm R. Beasley. Structure, physical properties, and applications of SrRuO 3 thin films. *Reviews of Modern Physics*, 84(1):253–298, 2012.

[19] Sita Dugu, Karuna Kara Mishra, Dhiren K. Pradhan, Shalini Kumari, and Ram S. Katiyar. Coupled phonons and magnetic orderings in GaFeO3 : Raman and magnetization studies. *Journal of Applied Physics*, 125(6):064101, 2019.

[20] Manfred Fiebig. Revival of the magnetoelectric effect. *Journal of physics D: applied physics*, 38(8):R123, 2005.

[21] Ce-Wen Nan, MI Bichurin, Shuxiang Dong, D Viehland, and G Srinivasan. Multiferroic magnetoelectric composites: Histori-

cal perspective, status, and future directions. *Journal of applied physics*, 103(3):1, 2008.

[22] Yao Wang, Jiamian Hu, Yuanhua Lin, and Ce-Wen Nan. Multiferroic magnetoelectric composite nanostructures. *NPG Asia Materials*, 2(2):61–68, 2010.

[23] Bipul Deka, S. Ravi, A. Perumal, and D. Pamu. Effect of Mn doping on magnetic and dielectric properties of YFeO3. *Ceramics International*, 43(1):1323–1334, 2017.

[24] C. Cannas, A. Musinu, Giorgio Piccaluga, D. Fiorani, D. Peddis, H. K. Rasmussen, and S. Mørup. Magnetic properties of cobalt ferrite-silica nanocomposites prepared by a sol-gel autocombustion technique. *Journal of Chemical Physics*, 125(16), 2006.

[25] J. I. Gittleman, B. Abeles, and S. Bozowski. Superparamagnetism and relaxation effects in granular Ni-SiO2 and Ni-Al2O3 films. *Physical Review B*, 9(9):3891–3897, 1974.

[26] E. M.M. Ibrahim, Silke Hampel, A. U.B. Wolter, M. Kath, A. A. El-Gendy, R. Klingeler, Christine Täschner, Vyacheslav O. Khavrus, Thomas Gemming, Albrecht Leonhardt, and Bernd Büchner. Superparamagnetic FeCo and FeNi nanocomposites dispersed in submicrometer-sized C spheres. *Journal of Physical Chemistry C*, 116(42):22509–22517, 2012.

[27] J. Smit. Past, Present, and Future of Ferrites. *Advances in Ceramics*, 15:1–4, 1985.

[28] Darrell G. Schlom, Long Qing Chen, Craig J. Fennie, Venkatraman Gopalan, David A. Muller, Xiaoqing Pan, Ramamoorthy Ramesh, and Reinhard Uecker. Elastic strain engineering of ferroic oxides. *MRS Bulletin*, 39(2):118–130, 2014.

[29] M. Louis Néel. Propriétés magnétiques des ferrites ; ferrimagnétisme et antiferromagnétisme. *Annales de Physique*, 12(3):137–198, 1948.

[30] Xabier Lasheras, Maite Insausti, Jesús Martínez de la Fuente, Izaskun Gil de Muro, Idoia Castellanos-Rubio, Lourdes Marcano, Maria Luisa Fernández-Gubieda, Aida Serrano, Rosa Martín-Rodríguez, Eneko Garaio, Jose Angel García, and Luis Lezama. Mn-Doping level dependence on the magnetic response of Mn x Fe 3x O 4 ferrite nanoparticles . *Dalton Transactions*, 48(30):11480–11491, 2019.

[31] Jeong Hyun Shim, Soonchil Lee, and B. I. Min. Abnormal spin structure of manganese ferrite investigated by Fe57 NMR. *Physical Review B - Condensed Matter and Materials Physics*, 75(13):2–6, 2007.

[32] E Strelcov, Y Kim, JC Yang, YH Chu, P Yu, X Lu, S Jesse, and SV Kalinin. Role of measurement voltage on hysteresis loop shape in piezoresponse force microscopy. *Applied Physics Letters*, 101(19):192902, 2012.

[33] Ferroelastic switching for nanoscale non-volatile magnetoelectric devices. *Nature Materials*, 9(4):309–314, 2010.

[34] Rajesh K. Katiyar, Pankaj Misra, Frank Mendoza, Gerardo Morell, and Ram S. Katiyar. Switchable photovoltaic effect in bilayer graphene/BiFeO3/Pt heterostructures. *Applied Physics Letters*, 105(14):1–5, 2014.

[35] Meng Wang, Ting Wang, Shenhua Song, Muchakayala Ravi, Renchen Liu, and Shishan Ji. Enhanced multiferroic properties of YMnO3 ceramics fabricated by spark plasma sintering along with low-temperature solid-state reaction. *Materials*, 10(5):1–10, 2017.

[36] B. Dhanalakshmi, Pratap Kollu, B. Chandra Sekhar, B. Parvatheeswara Rao, and P. S.V.Subba Rao. Enhanced magnetic and magnetoelectric properties of Mn doped multiferroic ceramics. *Ceramics International*, 43(12):9272–9275, 2017.

[37] PK Bajpai, Mukul Pastor, and KN Singh. Diffuse phase transition and electrical conductivity of pb (ca 1/3 nb 2/3) o 3. *Journal of electronic materials*, 43(5):1403–1410, 2014.

[38] H Vogel. The temperature dependence law of viscousity of fluids. *Phys. Z.*, 22:645–646, 1921.

[39] Gordon S. Fulcher. Analysis of Recent Measurements of the Viscosity of Glasses. *Journal of the American Ceramic Society*, 75(5):1043–1055, 1992.

[40] Vijay Singh, Aatish Daryapurkar, Shailendra S. Rajput, Somdutta Mukherjee, Ashish Garg, and Rajeev Gupta. Effect of annealing atmosphere on leakage and dielectric characteristics of multiferroic gallium ferrite. *Journal of the American Ceramic Society*, 100(11):5226–5238, 2017.

[41] I. Rivera, Ashok Kumar, N. Ortega, R. S. Katiyar, and Sergey Lushnikov. Divide line between relaxor, diffused ferroelectric, ferroelectric and dielectric. *Solid State Communications*, 149(3-4):172–176, 2009.

[42] Rana Saha, Ajmala Shireen, Sharmila N. Shirodkar, Umesh V. Waghmare, A. Sundaresan, and C. N.R. Rao. Multiferroic and magnetoelectric nature of GaFeO3, AlFeO3and related oxides. *Solid State Communications*, 152(21):1964–1968, 2012.

[43] Roy Roukos, Nissrine Zaiter, and Denis Chaumont. Relaxor behaviour and phase transition of perovskite ferroelectrics-type complex oxides (1–x) na 0.5 bi 0.5 tio 3–xcatio 3 system. *Journal of Advanced Ceramics*, 7(2):124–142, 2018.

[44] D Wang, AA Bokov, Z-G Ye, J Hlinka, and L Bellaiche. Subterahertz dielectric relaxation in lead-free ba (zr, ti) o 3 relaxor ferroelectrics. *Nature communications*, 7(1):1–7, 2016.

[45] Shalini Kumari, Nora Ortega, Dhiren K Pradhan, Ashok Kumar, James Floyd Scott, and Ram S Katiyar. Effect of thickness on dielectric, ferroelectric, and optical properties of ni substi-

tuted pb (zr0. 2ti0. 8) o3 thin films. *Journal of Applied Physics*, 118(18):184103, 2015.

[46] Chung Hua Chao, Mao Yi Chen, Chii Ruey Lin, Yueh Chung Yu, Yeong Der Yao, and Da Hua Wei. Postannealing effect at various gas ambients on Ohmic contacts of Pt/ZnO nanobilayers toward ultraviolet photodetectors. *International Journal of Photoenergy*, 2013, 2013.

[47] A. Lajn, H. v. Wenckstern, Z. Zhang, C. Czekalla, G. Biehne, J. Lenzner, H. Hochmuth, M. Lorenz, M. Grundmann, S. Wickert, C. Vogt, and R. Denecke. Properties of reactively sputtered Ag, Au, Pd, and Pt Schottky contacts on n-type ZnO. *Journal of Vacuum Science & Technology B: Microelectronics and Nanometer Structures*, 27(3):1769, 2009.

[48] Yan Sun, Ni Zhong, Yuan Yuan Zhang, Rui Juan Qi, Rong Huang, Xiao Dong Tang, Ping Xiong Yang, Ping Hua Xiang, and Chun Gang Duan. Structure and electrical properties of epitaxial SrRuO3 thin films controlled by oxygen partial pressure. *Journal of Applied Physics*, 120(23), 2016.

[49] István Robel, Bruce A. Bunker, and Prashant V. Kamat. Single-walled carbon nanotube-CdS nanocomposites as light-harvesting assemblies: Photoinduced charge-transfer interactions. *Advanced Materials*, 17(20):2458–2463, 2005.

[50] K. Miura and K. Terakura. Electronic and magnetic properties of La 2 FeCrO 6 : Superexchange interaction for a d 5 -d 3 system. *Physical Review B - Condensed Matter and Materials Physics*, 63(10):7, 2001.

[51] T. Arima, Y. Tokura, and J. B. Torrance. Variation of optical gaps in perovskite-type 3d transition-metal oxides. *Physical Review B*, 48(23):17006–17009, 1993.

[52] Optical absorption and band gap reduction in (Fe1- XCr x)2O3 solid solutions: A first-principles study. *Journal of Physical Chemistry C*, 117(48):25504–25512, 2013.

[53] Ganesh Kotnana and S. Narayana Jammalamadaka. Band gap tuning and orbital mediated electron–phonon coupling in HoFe 1x Cr x O 3 (0 x 1) . *Journal of Applied Physics*, 118(12):124101, 2015.

[54] Saji George, Suman Pokhrel, Zhaoxia Ji, Bryana L. Henderson, Tian Xia, Linjiang Li, Jeffrey I. Zink, André E. Nel, and Lutz Mädler. Role of Fe doping in tuning the band gap of TiO 2 for the photo-oxidation-induced cytotoxicity paradigm. *Journal of the American Chemical Society*, 133(29):11270–11278, 2011.

Chapter 5

Study of T-RRAM on graphene electroded Aluminium oxide thin films

5.1 Introduction

Resistive switching is a basic physical phenomenon in which resistivity of materials can be electrically modulated between nonvolatile high and low conducting logic states. The potential incorporation of resistive random access memory (RRAM) in the realm of next generation highly scaled electronic and opto-electronic circuits and neuromorphic computing is envisaged owing to its high operation speed ($\sim$ 100 ps), high-density storage, low power consumption, excellent endurance (10^{12} cycles), low cost, and simple cell architecture [1, 2, 3, 4, 5, 6, 7, 8, 9]. Recently, extensive interest has risen in visible transparent electronic circuit applications in consumer electronics, defense, space, civilian, and transport sectors such as integrated solar panel, touch panel, and

wearable displays [10] and large-area sensors [11] . Transparency of the display, logic, and memory units of the integrated circuit is essential to establish the above goal. High optical transparency and high electronic conductions are two mutually exclusive properties. Although researchers have demonstrated see-through transistors [12, 13] high transparency with efficient charge trapping is still a challenging task in mainstream floating gate thin film storage memories in addition to their physical scaling limitation. This issue can be overcome by RRAM that works on a non-charge-based mechanism [14] as long as both resistance-active (oxide) material and electrodes possess more than 80% transparency throughout the visible spectrum [15, 16, 17]. Over the past few years, considerable effort has been made to address this existing challenge by developing a variety of new material combinations that include oxides, organics, two-dimensional conductors, and nanostructures in vertical and planar sandwiched architectures and device processing techniques [15, 18, 19, 20, 21, 22].

With the motivation to design and evaluate transparent, lightweight, and scalable devices, we have studied the switching behavior of a transparent resistive random-access memory (TRRAM) fabricated on a glass platform with semiconductor process friendly Al_2O_3 as a functional oxide layer, intensively researched graphene as a top electrode, and

conventional n-type (partly due to oxygen vacancies) ITO as bottom electrodes for non-volatile memory applications. Binary oxides such as HfO_2 [23], TiO_2 [24], NiO [25], ZrO_2 [26], Nb_2O_5 [26], and Al_2O_3 [27] have been extensively studied for the fabrication of RRAM due to their simple conformation, good compatibility with CMOS back end of line technology, and low-cost of fabrication. Al_2O_3 has drawn the particular attention of scientific community because of its moderately high permittivity of $\sim 8 - 10$, wide optical bandgap of ~ 9 eV with transparency down to deep UV (beneficial for the initial high resistance state), large breakdown electric field of $\sim 5 - 30$ MV/cm, good thermal stability of as high as 1000°C, and low cost [11]. Based on these properties, Al_2O_3 has found potential applications like high-k gate insulator in thin film transistors [28], tunnel-control oxides in flash memory [29], resistance switching layer in RRAM [30], dielectric layer in metal/insulator/metal (MIM) capacitors [31], surface modification at the cathode in Li-ion batteries that improves the cycle stability of the cell [32], and gas diffusion barrier in organic electronic devices [33], to name a few. Graphene, a two-dimensional crystal made up of just hexagonal covalent bonded carbon atoms, possesses unique electronic properties such as high charge carrier mobility ($\sim 10^4$ cm^2/V s), electrical (~ 2000 S/cm) and thermal (~ 5000 W/mK) conductivities, me-

chanical strength ($\sim$ 40 N/m), and flexibility [34, 35, 36]. It is a promising candidate material for transparent conductor applications due to its low sheet resistance ($\sim$ 30 $\Omega/\square$) and low light absorbance (only $\sim$ 2.3 %) [37, 38] and has the potential to replace the commercially available transparent conducting electrode, ITO, in near future. Being a good transparent conductor as well as oxygen passivation layer, graphene has shown to be an effective electrode material for various devices. For example, Yang *et al.* [10] have shown that insertion of graphene layer above the oxide layer helps in reducing resistance variation of high resistance states. Lee *et al.* [39] reported that graphene electrodes improved the performance of pentacene organic FET significantly such as minimized channel resistance, high mobility, and reduced effective barrier height compared to traditional Au electrodes. In this study, in order to figure out the efficiency of graphene as the top electrode in the device, we have compared its performance with an identical device but with conventional platinum as a top electrode.

5.2 Experimental Details

Commercial low cost 180 nm thick ITO coated glass was used as a substrate for Al_2O_3 thin film deposition. About 15 nm thick amorphous Al_2O_3 layers were deposited on these substrates by plasma-enhanced

atomic layer deposition (PE-ALD) in a Picosun R200 system at an optimized growth rate of 1.1 Å/cycle. Trimethyl aluminum (TMA) was used as a precursor of aluminum, and oxygen plasma acted as an oxidizing agent. The substrate temperature was maintained at 200 °C, a low device processing temperature. The thickness of the deposited film was measured using a JA Woollam spectroscopic ellipsometer. X-ray photoelectron spectroscopy (XPS) was performed on the Al_2O_3 layer with a monochromatized Al K_α X-ray source operating at a base pressure of 4.9 X 10^9 Torr. Monolayer graphene (G) used in the device as the top electrode was grown on copper in a hot filament chemical vapor deposition (HFCVD) reactor at a substrate temperature of 1000 °C and a filament temperature of 1600 °C by flowing 1 sccm of methane for 80 min in a hydrogen atmosphere of 35 Torr. The graphene layer was then transferred from copper to Glass-ITO/Al_2O_3 by a standard poly methyl methacrylate (PMMA) assisted wet transfer method. About 500 nm thick layer of PMMA (MicroChem 950 A9) was spin-coated on the copper/graphene sample and, subsequently, baked on a hot plate at a temperature of 150 °C for 10 min. The copper substrate was then etched out by 20 % ammonium persulfate solution. The obtained G/PMMA sample was rinsed several times in de-ionized water and placed onto the ITO/Al_2O_3 sample that was placed overnight on

a hot plate set at 45 °C. Finally, the top PMMA layer was removed by selectively dissolving it in hot acetone to obtain a layer of graphene on ITO/Al_2O_3. Then after, to obtain a desired shape of graphene top electrode, at first, we evaporated $\sim$ 200 nm thick square gold layer on the 2D material through a metal shadow mask. The device was then subjected to oxygen plasma etching at a power of 80 W under a pressure of 200 mTorr to remove the graphene which was uncovered by gold. The gold layer covering the non-reacted graphene was removed by a reclamation process to obtain patterned graphene top electrodes. For this purpose, the sample was kept in a solution of 4 gm of KI, 1 gm of I_2, and 40 ml of de-ionized water for 10 h and then dried by N_2. The gold removal can be explained by the following series of reactions [40]. $I_2 + KI \rightarrow K^+ + I_3^-$, iodine reacts with potassium iodide to form potassium ion and tri-iodide anion. These products can react with gold to form potassium auric iodide, $3K^+ + 3I_3^- + 2Au \rightarrow 2KAuI_4 + K^+ + I_3^-$. Hence the gold completely reacts with potassium and iodine ion leaving the ITO/Al_2O_3/G sample gold free. The device fabrication process is schematically shown in Fig. 5.1(a).

The surface topography of the graphene electrodes and active oxide layer was analyzed in vacuum using a scanning electron microscope operating at 70x magnification. Phase purity of processed graphene

was further confirmed by Raman spectroscopy. The laser line at 514.5 nm from a coherent argon ion laser (Innova 70-C) was focused on the sample. A liquid nitrogen-cooled CCD device collected the Raman scattered signal through a 50x objective. The transmittance spectra of the device were recorded by a ratio recording, computer controlled UV-visible spectrometer (Shimadzu UV-2450) in the spectral range of 280–800 nm. I-V measurements were done at room temperature using a Keithley electrometer (model #2401) with the top electrode DC biased and the bottom electrode grounded. For comparative study, $\sim$ 50 nm thick and $\sim$ 90 μm broad square platinum dots were deposited on an identical ITO/Al_2O_3 sample by dc-magnetron sputtering at a power density of 1 W/cm^2 using a metal shadow mask to form the ITO/Al_2O_3/Pt capacitor structure (control device) as shown in Fig. 5.1(b).

5.3 Results and discussion

Figure 5.2(a) shows the SEM image of well-defined graphene top electrodes having an area of $\sim$80 x 80 μm^2. The Raman spectra showed in Fig. 5.2(b) provided an intensity ratio of the two prominent peaks; G-band (1580 cm^{-1}) originated from the in-plane vibration of sp2 carbon atoms and 2D-band (2689 cm^{-1}) due to the two-phonon double

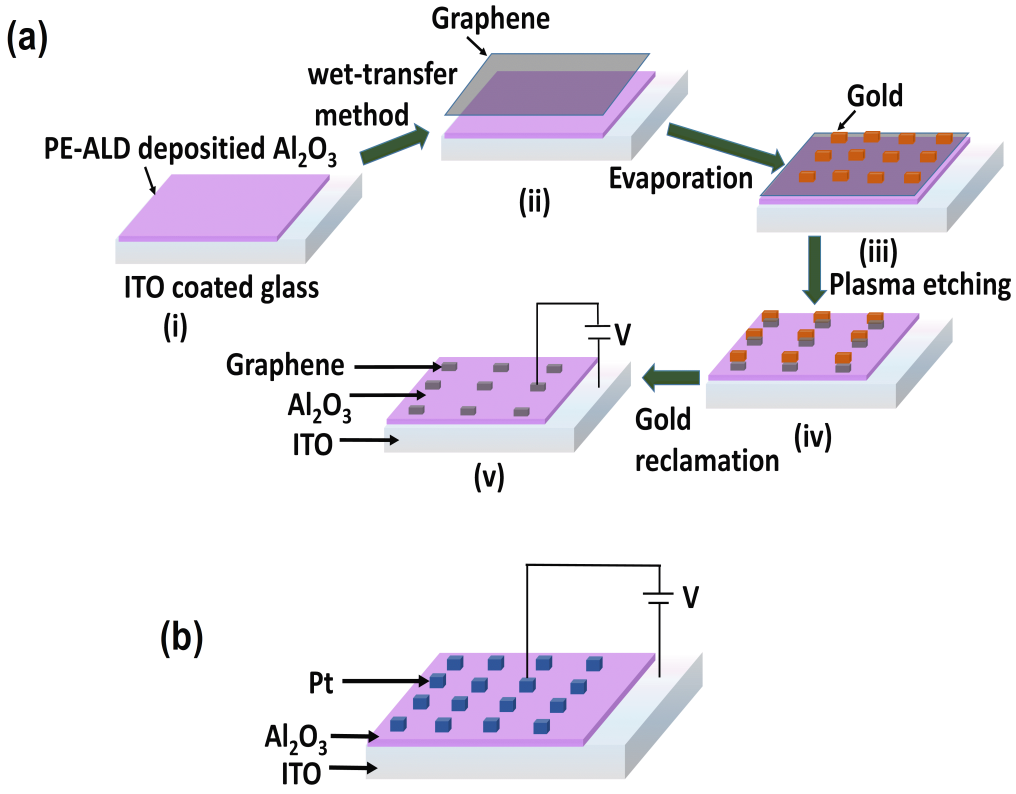

Figure 5.1: (a) Fabrication process of the ITO/Al_2O_3/G device, (b) Schematic of ITO/Al_2O_3/Pt capacitor.

resonance as 0.5. This figure along with a full-width at half maximum (FWHM) of $\sim$ 12 cm^{-1} for G-band and $\sim$ 32 cm^{-1} for 2D-band confirmed the monolayer nature of graphene. Figure 5.2(c) shows that the fabricated device is highly transparent in the visible region (370-700 nm) with an optical transparency of $>$ 82%. It is apparent that the transparency of the device is not significantly affected by the process of graphene electrode formation. Optical transmittance of ITO/Al_2O_3 structure is reduced slightly (only by 1.2 %) because of low optical absorbance in graphene [37]. Note that here graphene square dots serving

as top electrodes occupy less area resulting in less transmittance reduction as compared to reported 2 % reduction for the graphene layer [41].

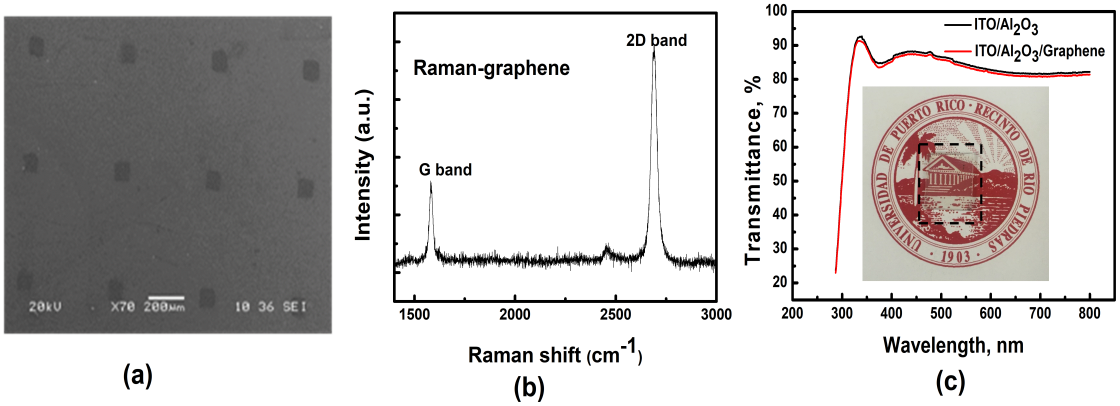

Figure 5.2: (a) SEM image of graphene square dots on the Al_2O_3 layer. (b) Raman spectra of graphene on Al_2O_3 showing G- and 2D-bands. (c) Optical transmission spectra of ITO/Al_2O_3 and ITO/Al_2O_3/G samples and the inset shows the ITO/Al_2O_3/G sample placed on the university logo.

Figure 5.3 shows the resistive switching characteristics of the TR-RAM devices with graphene and Pt as top or SET electrodes. Electroforming is the primary step and is an essential phenomenon in resistive switching to commence switching in the active material. This process is usually carried out by applying a high voltage or current compliance to the as-prepared switching device [5, 42] that in turn leads to the controlled decrease in resistance. In this study, electroforming was observed at 4.8 V and 6.8 V for ITO/Al_2O_3/G and ITO/Al_2O_3/Pt devices, respectively, which was revealed by a sudden increase in current flow and are shown as insets (b) and (c) in Fig. 5.3. To avoid any electric

breakdown due to high current flow, compliance current I_{cc} was set at 1 mA in both cases. In the case of ITO/Al_2O_3/G, the device turned to low resistance state (LRS), also called ON-state with a resistance of $\sim$ 330 Ω (read at 0.1 V) after electroforming. On applying a negative bias voltage, the current suddenly decreased from $\sim$ 1.55 mA to $\sim$ 2.1 μA at $\sim$ - 0.65 V, turning the device from LRS to HRS (High Resistance State) also called OFF-state, and the process is called the "RESET" process. Subsequently, applying the positive voltage bias from 0 V onwards, a rapid increase in current was observed at $\sim$ 0.8 V, switching the device back to LRS again, called as "SET" process. Hence, the device is found to switch with alternate polarity, hence called bipolar switching. In the case of the ITO/Al_2O_3/Pt device, SET and RESET voltages were observed at 2.6 V and - 2.4 V (a drop in RESET or operation current from $\sim$ 18.9 mA to $\sim$ 89 μA), respectively, which is higher than the corresponding figures obtained for ITO/Al_2O_3/G.

Endurance and retention properties were measured for a better evaluation of the reliability and functional characteristics of the devices. Resistance at the ON-state is denoted by R_{ON} measured under an Icc of 1 mA and that at the OFF state is denoted by R_{OFF} (both read at + 0.1 V). The endurance test of the ITO/Al_2O_3/G transparent device depicted in Fig. 5.4(a) demonstrates no signs of memory state deterio-

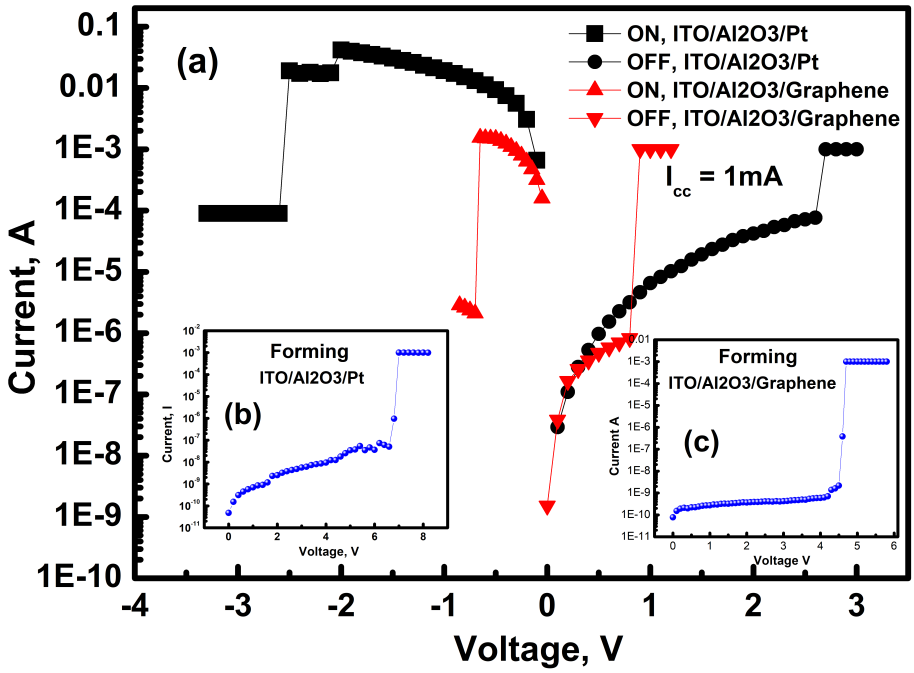

Figure 5.3: (a) Resistive switching characteristics and the forming process of (b) ITO/Al_2O_3/Pt and (c) ITO/Al_2O_3/G devices.

ration. For retention tests, the resistance at the ON state was read out for 10^4 s at + 0.1 V, subsequently, the device was switched to the OFF state, and the resistance was recited for 10^4 s. The ratio of R_{OFF}/R_{ON} was observed to be $\sim$ 5x10^3. Replotting the I-V curve in log-log scale as shown in Fig. 5.4(c), the conduction mechanism in the ON state of the ITO/Al_2O_3/G device was concluded to be of Ohmic nature as the slope of the plot was determined to be $\sim$ 1. This can be due to the formation of conductive filaments in the device during the SET process. In the OFF state, the I-V plot showed a linear behavior at low voltages

(0 to + 0.4 V). However, at high voltages, the device showed a non-linear behavior dominated by the electrode/interface-limited Schottky charge transport which can be elucidated via the room temperature linear current density (J) vs $E^{1/2}$ plot shown in the inset of Fig. 5.4(d). The Ohmic behavior at a lower voltage regime might be due to the remnant minor concentration of tiny conductive filaments even after rupture of majority of filaments during the SET process.

Endurance and retention tests conducted on the ITO/Al_2O_3/Pt device are shown in Figs. 5.5(a) and 4(b), respectively. The obtained R_{OFF}/R_{ON} ratio was $\sim 10^4$ and is in fairly good agreement with the study by Wu *et al.* [43]. Both ON and OFF states were observed to be stable, and no significant degradation was seen. The switching ratio of approximately 10^4 in the retention of bistable resistive states may be prolonged to more than 10 years [43]. The ON state leakage curve replotted in logarithmic scale [Fig. 5.5(c)] can be approximated by a straight line with a slope of ~ 1, confirming Ohmic conduction. I-V characteristics for the OFF state showed a nonlinear behavior. The conduction mechanism can be identified as bulk limited Pool-Frenkel emission [43, 44] as the ln J/E versus $E^{1/2}$ plot shows a linear relationship as demonstrated in Fig. 5.5(d). The difference between metal work-function and Fermi level of the wide bandgap semiconductor (in-

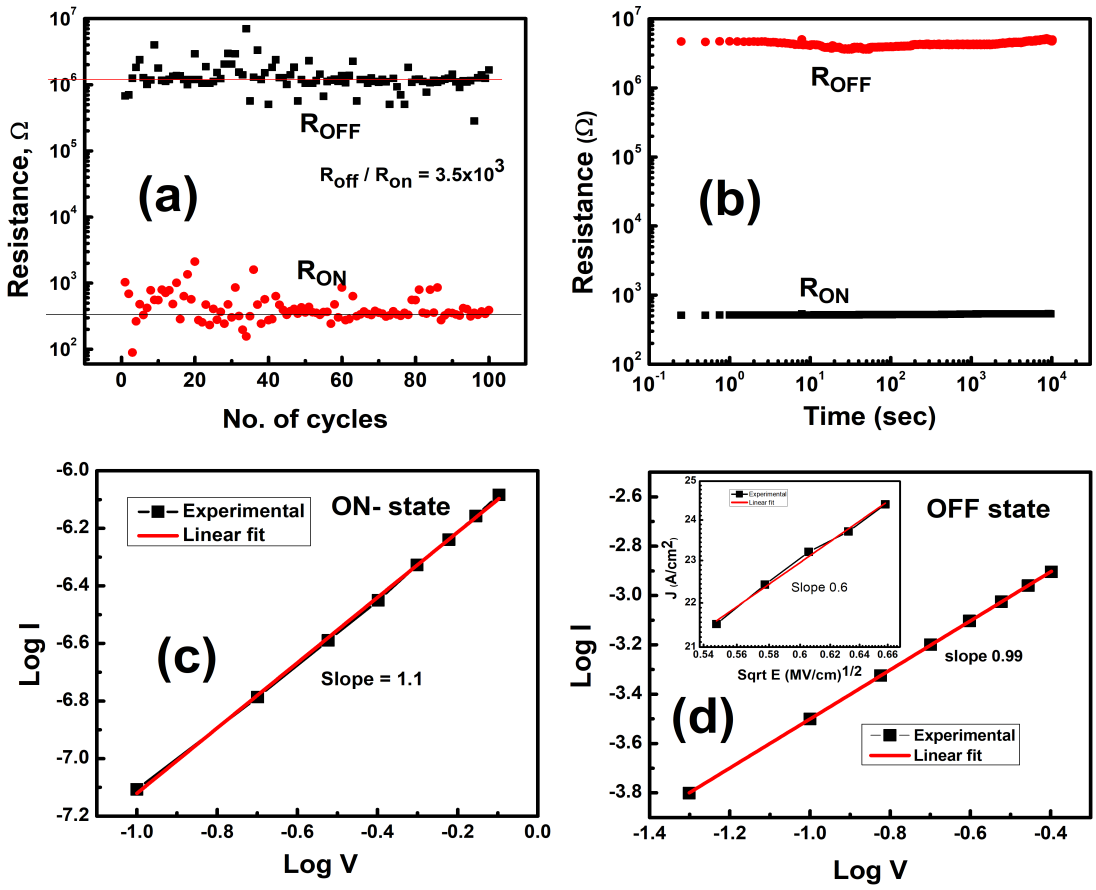

Figure 5.4: (a) Endurance characteristics of the ITO/Al_2O_3/G device over 100 cycles. (b) Retention behavior of the ITO/Al_2O_3/G device over 10^4 seconds. Log-log I-V characteristics of the ITO/Al_2O_3/G device at (c) ON state and (d) OFF state. The inset of (d) shows the linear relation between J and sqrt E implying the Schottky conduction mechanism.

sulator) determines the type of contact [45] during the formation of the metal-insulator interface and explains the asymmetry observed in the I-V data (Fig. 5.3). The work-function of graphene ($\sim$ 4.9 eV) and platinum ($\sim$ 5.2 eV) is higher than that of ITO ($\sim$ 4.7 eV). This higher work-function can be attributed to the formation of the Schottky bar-

rier at the G or Pt/insulator active interface with an expected shorter barrier height for G.

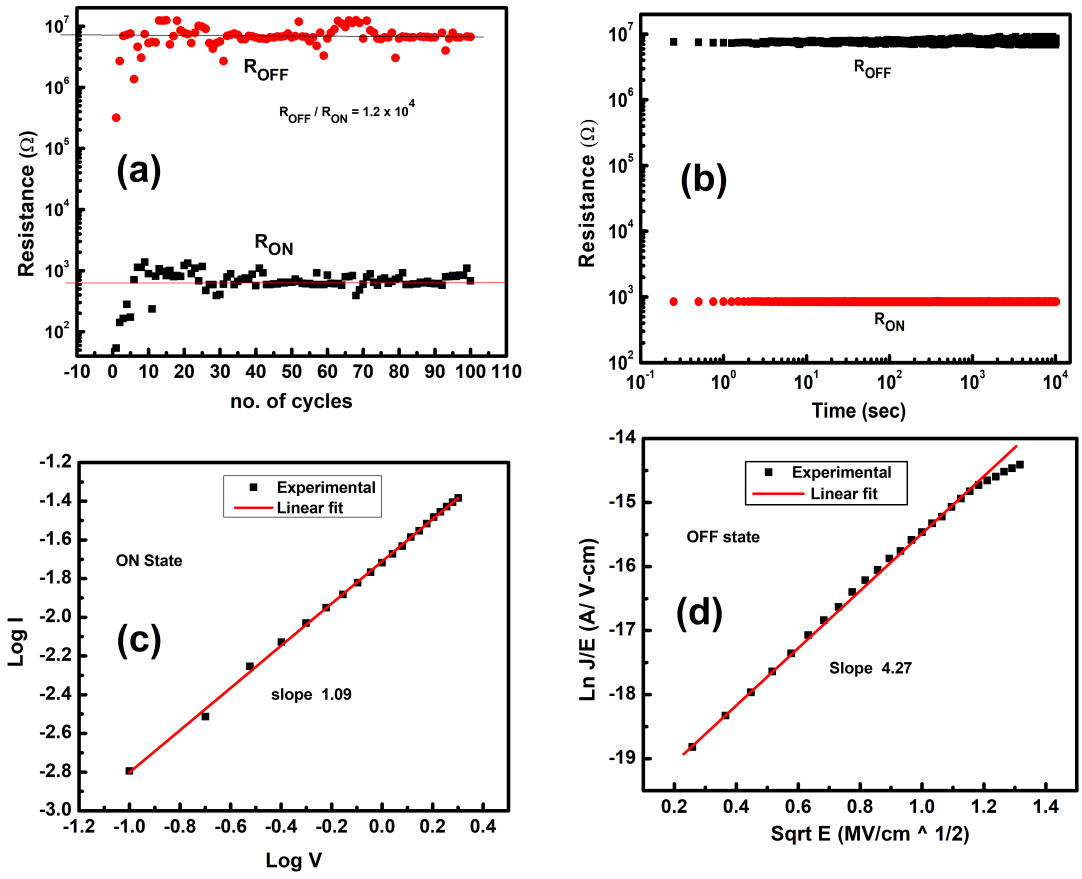

Figure 5.5: (a) Endurance characteristics of the ITO/Al_2O_3/Pt device over 100 cycles. (b) Its retention behavior over 104 seconds. (c) Log-log I-V characteristics of the ITO/Al_2O_3/Pt device at the ON state. (d) ln J/E vs Sqrt E relation at the OFF state of the device.

The observed significant difference in SET and RESET voltages is usually the result of the electrode-oxide interaction [41, 45]. Graphene shows a low sheet resistance (in-plane) and much lower contact resistance with an insulator than other conventional electrodes like Pt.

G/Al_2O_3 is a Schottky contact [41] that helps us to improve the electric field intensity in the switching layer and hence a faster conductive filament growth. Also, nonpolar graphene exhibits a weak interaction with other materials resulting in an out-of-plane (6 k$\Omega/\square$) leading to a high series resistance and a low RESET current in the device. Owing to its higher work function than G, Pt is expected to have a higher Schottky barrier height with Al_2O_3 which in turn results in a larger voltage drop prior to the filament formation. The filament formation is associated with the Joule heating generated during the Forming/SET/RESET processes [46]. The inert and atomically thin graphene has a much lower out-of-plane thermal conductivity ($\sim$ 6 $Wm^{-1}K^{-1}$) than its in-plane counterpart (2000-4000 $Wm^{-1}K^{-1}$) [47] and can act as an interfacial thermal resistance that can considerably reduce the heat dissipated making the programming processes more energy-efficient [48]. It can be noted that the programming power given by the product of RESET voltage and the peak in RESET current was $\sim$ 1 mW for the graphene electroded device which is only $\sim$ 2% of that consumed by the Pt electroded device. This indicates the possibility of reducing the programming power further by lowering the SET current compliance in scaled devices without compromising the stability in switching. Additionally, it has been proved that graphene can remove an undesired

surface effect better that increases switching yield of the RRAM device [11, 41].

Though not well understood, various models have been proposed to illustrate the mechanism of resistive switching, such as trap charging and discharging [49], formation and rupture of conduction filaments [50], and modulation of Schottky barrier [51]. Several studies on metal-oxide based RRAM have shown that the generation and recombination of oxygen vacancies are responsible for switching [22, 52, 53, 54]. In most dielectric layers, oxygen vacancy is the common defect which is responsible for switching. From an analysis of XPS survey spectrum shown in Fig. 5.6(a), the elemental ratio of Al:O:C (here C represents carbon in graphene electrode) was determined to be 0.265:0.257:0.477. An asymmetric O 1s core level spectrum [Fig. 5.6(b)] obtained was Gaussian deconvoluted into two peaks after Shirley background correction. The binding energy of 530.4 eV (FWHM $\sim$ 2.23 eV) could be attributed to the oxygen that was bound to Al in the Al_2O_3 lattice, while that at 531.47 eV (FWHM $\sim$ 2.29 eV) belongs to the oxygen deficiencies (oxygen vacancies), a common defect found in the dielectric layer. Hence, we assume that oxygen vacancies play a key role in switching mechanism as explained below. Figure 5.6(c) shows the schematic of the switching process mechanism that undergoes at OFF

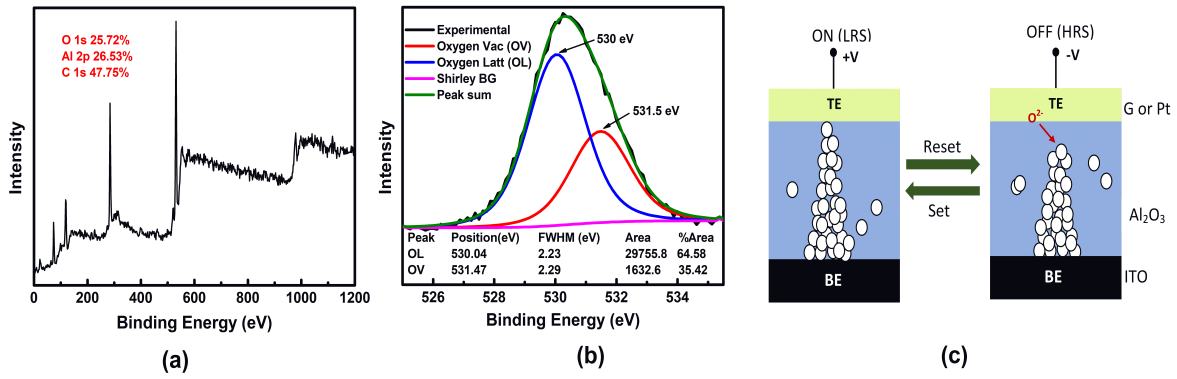

Figure 5.6: (a) XPS survey spectra. (b) O 1s core level spectra of the Al_2O_3 film on the ITO substrate. (c) Schematic illustration of the RS mechanism based on the I-V characteristics.

and ON states. During the SET process, under positive bias, oxygen anions were extracted from the lattice, accumulating oxygen vacancies in the disordered Al_2O_3 layer starting from the ITO/Al_2O_3 interface resulting in a considerable reduction of the Schottky barrier height at the G or Pt/Al_2O_3 interface. The Kroger-Vink notation given below expresses the formation of the oxygen vacancies [55, 56]

$$O_o \rightarrow V_o^{2+} + 2e^- + \frac{1}{2}O_2 \tag{5.1}$$

where O_o represents an oxygen ion in a regular site and V_o^{2+} is an oxygen vacancy with a double positive charge in the regular lattice site. Negatively charged non-lattice oxygen anions ($O^{2-} \rightarrow \frac{1}{2}O_2 + 2e^-$ thus formed are dragged toward the top electrode [57] leaving behind a more oxygen deficient Al_2O_{3-n} active layer. This process leads to the

formation of a conical shaped filament made up of oxygen vacancies in the oxide layer as shown in Fig. 5.6(c) which acts as the low resistance path for the current flow. Hence current flows steadily through the filament resulting in a low resistance state in the Al_2O_{3-n} layer. The interface between the electrode and the oxide performs a vital role in the switching process [57]. Under the application of a negative bias voltage, non-lattice oxygen anions start to migrate from the interface, injecting into the lattice. While recombining oxygen ions with vacancies, the oxidation reaction occurs that results in a more insulating Al_2O_3 state. During this process, the conductive filaments in the Al_2O_{3-n} layer split causing a sudden drop in current. Thereafter the device gets switched to HRS, called RESET.

Bibliography

[1] YY Chen, L Goux, L Pantisano, Johan Swerts, C Adelmann, S Mertens, VV Afanasiev, XP Wang, B Govoreanu, R Degraeve, et al. Scaled x-bar tin/hfo2/tin rram cells processed with optimized plasma enhanced atomic layer deposition (peald) for tin electrode. *Microelectronic engineering*, 112:92–96, 2013.

[2] Sung Hyun Jo, Ting Chang, Idongesit Ebong, Bhavitavya B. Bhadviya, Pinaki Mazumder, and Wei Lu. Nanoscale memristor device as synapse in neuromorphic systems. *Nano Letters*, 10(4):1297–1301, 2010.

[3] J Joshua Yang, Dmitri B Strukov, and Duncan R Stewart. Memristive devices for computing. *Nature nanotechnology*, 8(1):13–24, 2013.

[4] Antonio C Torrezan, John Paul Strachan, Gilberto Medeiros-Ribeiro, and R Stanley Williams. Sub-nanosecond switching of a tantalum oxide memristor. *Nanotechnology*, 22(48):485203, 2011.

[5] Deok-Hwang Kwon, Kyung Min Kim, Jae Hyuck Jang, Jong Myeong Jeon, Min Hwan Lee, Gun Hwan Kim, Xiang-Shu Li, Gyeong-Su Park, Bora Lee, Seungwu Han, Miyoung Kim, and Cheol Seong Hwang. Atomic structure of conducting nanofilaments in TiO2 resistive switching memory. *Nature Nanotechnology*, 5(2):148–153, 2010.

[6] E. Y. Tsymbal and A Gruverman. Material witness: Nano contraception. *Nature Mater.*, 12:602, 2013.

[7] G. I. Meijer. Who Wins Nonvolatile Memory Race? *Science*, 319:1625, 2008.

[8] Seunghyun Lee, Joon Sohn, Zizhen Jiang, Hong-Yu Chen, and H.-S. Philip Wong. Metal oxide-resistive memory using graphene-edge electrodes. *Nature Communications*, 6:8407, 2015.

[9] Pirovano A and Schuegraf K. Integrated Circuits: Memory grows up. *Nature Nanotechnology*, 5:177–178, 2010.

[10] Po Kang Yang, Wen Yuan Chang, Po Yuan Teng, Shuo Fang Jeng, Su Jien Lin, Po Wen Chiu, and Jr Hau He. Fully transparent resistive memory employing graphene electrodes for eliminating undesired surface effects. *Proceedings of the IEEE*, 101(7):1732–1739, 2013.

[11] Seung-Won Yeom, Sang-Chul Shin, Tan-Young Kim, Hyeon Jun Ha, Yun-Hi Lee, Jae Won Shim, and Byeong-Kwon Ju. Transparent resistive switching memory using aluminum oxide on a flexible substrate. *Nanotechnology*, 27(7):07LT01, 2016.

[12] Arun Suresh, Steven Novak, Patrick Wellenius, Veena Misra, and John F. Muth. Transparent indium gallium zinc oxide transistor based floating gate memory with platinum nanoparticles in the gate dielectric. *Applied Physics Letters*, 94(12), 2009.

[13] Hisato Yabuta, Masafumi Sano, Katsumi Abe, Toshiaki Aiba, Tohru Den, Hideya Kumomi, Kenji Nomura, Toshio Kamiya, and Hideo Hosono. High-mobility thin-film transistor with amorphous InGaZnO4 channel fabricated by room temperature rf-magnetron sputtering. *Applied Physics Letters*, 89(11):10–13, 2006.

[14] Rainer Waser and Masakazu Aono. Nanoionics-based resistive switching memories. *Nature materials*, 6(11):833–40, 2007.

[15] Jun Yao, Jian Lin, Yanhua Dai, Gedeng Ruan, Zheng Yan, Lei Li, Lin Zhong, Douglas Natelson, and James M. Tour. Highly transparent nonvolatile resistive memory devices from silicon oxide and graphene. *Nature Communications*, 3:1101, 2012.

[16] Akihito Sawa. Resistive switching in transition metal oxides. *Materials Today*, 11(6):28–36, 2008.

[17] D. Acharyya, A. Hazra, and P. Bhattacharyya. A journey towards reliability improvement of TiO2 based Resistive Random Access Memory: A review. *Microelectronics Reliability*, 54(3):541–560, 2014.

[18] Jung Won Seo, Jae Woo Park, Keong Su Lim, Ji Hwan Yang, and Sang Jung Kang. Transparent resistive random access memory and its characteristics for nonvolatile resistive switching. *Applied Physics Letters*, 93(22):2–5, 2008.

[19] Jie Shang, Gang Liu, Huali Yang, Xiaojian Zhu, Xinxin Chen, Hongwei Tan, Benlin Hu, Liang Pan, Wuhong Xue, and Run-Wei Li. Thermally stable transparent resistive random access memory based on all-oxide heterostructures. *Advanced Functional Materials*, 24(15):2171–2179, 2014.

[20] Jung Won Seo, Jae-Woo Park, Keong Su Lim, Sang Jung Kang, Yun Ho Hong, Ji Hwan Yang, Liang Fang, Gun Yong Sung, and Han-Ki Kim. Transparent flexible resistive random access memory fabricated at room temperature. *Applied Physics Letters*, 95(13):133508, 2009.

[21] Jungmoo Lee and Ohyun Kim. Nonvolatile Resistive Memory Device Based on Poly(3,4-ethylenedioxythiophene):Poly(styrene sulfonate) Thin Film for Transparent and Flexible Applications. *Japanese Journal of Applied Physics*, 50(6):06GF01, 2011.

[22] Rainer Waser, Regina Dittmann, Ceorgi Staikov, and Kristof Szot. Redox-based resistive switching memories nanoionic mechanisms, prospects, and challenges. *Advanced Materials*, 21(25-26):2632–2663, 2009.

[23] Seunghyup Lee, Wan-Gee Kim, Shi-Woo Rhee, and Kijung Yong. Resistance Switching Behaviors of Hafnium Oxide Films Grown by MOCVD for Nonvolatile Memory Applications. *Journal of The Electrochemical Society*, 155(2):H92, 2008.

[24] B. J. Choi, D. S. Jeong, S. K. Kim, C. Rohde, S. Choi, J. H. Oh, H. J. Kim, C. S. Hwang, K. Szot, R. Waser, B. Reichenberg, and S. Tiedke. Resistive switching mechanism of TiO 2 thin films grown by atomic-layer deposition. *Journal of Applied Physics*, 98(3):1–10, 2005.

[25] S. Seo, M. J. Lee, D. H. Seo, E. J. Jeoung, D. S. Suh, Y. S. Joung, I. K. Yoo, I. R. Hwang, S. H. Kim, I. S. Byun, J. S. Kim, J. S. Choi, and B. H. Park. Reproducible resistance switching in polycrystalline NiO films. *Applied Physics Letters*, 85(23):5655–5657, 2004.

[26] Chih-Yang Lin, Chung-Yi Wu, Chen-Yu Wu, Tseung-Yuen Tseng, and Chenming Hu. Modified resistive switching behavior of ZrO2 memory films based on the interface layer formed by using Ti top electrode. *Journal of Applied Physics*, 102(2007):094101, 2007.

[27] Chih-Yang Lin, Chen-Yu Wu, Chung-Yi Wu, Chenming Hu, and Tseung-Yuen Tseng. Bistable Resistive Switching in Al[sub 2]O[sub 3] Memory Thin Films. *Journal of The Electrochemical Society*, 154(9):G189, 2007.

[28] Seyoung Kim, Junghyo Nah, Insun Jo, Davood Shahrjerdi, Luigi Colombo, Zhen Yao, Emanuel Tutuc, and Sanjay K Banerjee. Realization of a high mobility dual-gated graphene field-effect transistor with al 2 o 3 dielectric. *Applied Physics Letters*, 94(6):062107, 2009.

[29] Sung Min Kim, Emil B. Song, Sejoon Lee, Jinfeng Zhu, David H. Seo, Matthew Mecklenburg, Sunae Seo, and Kang L. Wang. Transparent and flexible graphene charge-trap memory. *ACS Nano*, 6(9):7879–7884, 2012.

[30] Myeongcheol Kim and Kyung Cheol Choi. Transparent and flexible resistive random access memory based on al 2 o 3 film with multilayer electrodes. *IEEE Transactions on Electron Devices*, 64(8):3508–3510, 2017.

[31] S. B. Chen, C. H. Lai, A. Chin, J. C. Hsieh, and J. Liu. High-density MIM capacitors using Al2O3 and AlTiOx dielectrics. *IEEE Xplore Digital Library*, 23:185, 2002.

[32] Lijun Liu, Zhaoxiang Wang, Hong Li, Liquan Chen, and Xuejie Huang. Al2O3-coated LiCoO2 as cathode material foe lithium ion batteries. *Solid State Ionics*, 152:341–346, 2002.

[33] P. F. Carcia, R. S. McLean, M. H. Reilly, M. D. Groner, and S. M. George. Ca test of Al 2O 3 gas diffusion barriers grown by atomic layer deposition on polymers. *Applied Physics Letters*, 89(3):8–11, 2006.

[34] K. S. Novoselov, A. K. Geim, S. V. Morozov, D. Jiang, Y. Zhang, S. V. Dubonos, I. V. Grigorieva, and A. A. Firsov. Electric Field Effect in Atomically Thin Carbon Films. *Science*, 306:666, 2004.

[35] A. K. Geim. Graphene : Status and Prospects. *Science*, 324(2009):1530–1534, 2009.

[36] Gunho Jo, Minhyeok Choe, Sangchul Lee, Woojin Park, Yung Ho Kahng, and Takhee Lee. The application of graphene as electrodes

in electrical and optical devices. *Nanotechnology*, 23(11):112001, 2012.

[37] R. R Nair, P Blake, A. N Grigorenko, K. S Novoselov, T. J Booth, T Stauber, N. M. R Peres, and A. K Geim. Fine Structure Constant Defines Visual Transparency of Graphene. *Science*, 320(5881):1308, 2008.

[38] Jonathan K. Wassei and Richard B. Kaner. Graphene, a promising transparent conductor. *Materials Today*, 13(3):52–59, 2010.

[39] Wi Hyoung Lee, Jaesung Park, Sung Hyun Sim, Sae Byeok Jo, Kwang S Kim, Byung Hee Hong, and Kilwon Cho. Transparent flexible organic transistors based on monolayer graphene electrodes on plastic. *Advanced materials*, 23(15):1752–1756, 2011.

[40] RP Homick and H Sloan. Gold reclamation process. *US Pat*, 3(957):505, 1976.

[41] Xue Feng Wang, Hai Ming Zhao, Yi Yang, and Tian Ling Ren. Graphene resistive random memory - The promising memory device in next generation. *Chinese Physics B*, 26(3):1–14, 2017.

[42] Daniele Ielmini. Resistive switching memories based on metal oxides: mechanisms, reliability and scaling. *Semiconductor Science and Technology*, 31(6):063002, 2016.

[43] Shuxiang Wu, Xinman Chen, Lizhu Ren, Wei Hu, Fengmei Yu, Kungan Yang, Mei Yang, Yunjia Wang, Meng Meng, Wenqi Zhou, Dinghua Bao, and Shuwei Li. Write-once-read-many-times characteristics of Pt/Al2O3/ITO memory devices. *Journal of Applied Physics*, 116(7):074515, 2014.

[44] Kwan Chi Kao. *Dielelctric phenomena in Solids*. Elsevier Academic Press, 2004.

[45] S. Seo, M. J. Lee, D. C. Kim, S. E. Ahn, B. H. Park, Y. S. Kim, I. K. Yoo, I. S. Byun, I. R. Hwang, S. H. Kim, J. S. Kim, J. S. Choi, J. H. Lee, S. H. Jeon, S. H. Hong, and B. H. Park. Electrode

dependence of resistance switching in polycrystalline NiO films. *Applied Physics Letters*, 87(26):1–3, 2005.

[46] He Tian, Hong-Yu Chen, Bin Gao, Shimeng Yu, Jiale Liang, Yi Yang, Dan Xie, Jinfeng Kang, Tian-Ling Ren, Yuegang Zhang, et al. Monitoring oxygen movement by raman spectroscopy of resistive random access memory with a graphene-inserted electrode. *Nano letters*, 13(2):651–657, 2013.

[47] Eric Pop, Vikas Varshney, and Ajit K Roy. Thermal properties of graphene: Fundamentals and applications. *arXiv preprint arXiv:1301.6181*, 2013.

[48] Chiyui Ahn, Scott W Fong, Yongsung Kim, Seunghyun Lee, Aditya Sood, Christopher M Neumann, Mehdi Asheghi, Kenneth E Goodson, Eric Pop, and H-S Philip Wong. Energy-efficient phase-change memory with graphene as a thermal barrier. *Nano letters*, 15(10):6809–6814, 2015.

[49] Qi Liu, Weihua Guan, Shibing Long, Rui Jia, Ming Liu, and Junning Chen. Resistive switching memory effect of Zr O2 films with Zr+ implanted. *Applied Physics A*, 92(1):90–93, 2008.

[50] Kyung Min Kim, Byung Joon Choi, Yong Cheol Shin, Seol Choi, and Cheol Seong Hwang. Anode-interface localized filamentary mechanism in resistive switching of Ti O2 thin films. *Applied Physics Letters*, 91(1):2005–2008, 2007.

[51] A. Sawa, T. Fujii, M. Kawasaki, and Y. Tokura. Hysteretic current-voltage characteristics and resistance switching at a rectifying Ti/Pr0.7Ca0.3MnO3 interface. *Applied Physics Letters*, 85(18):4073–4075, 2004.

[52] Myung Ju Kim, Dong Su Jeon, Ju Hyun Park, and Tae Geun Kim. Bipolar resistive switching characteristics in tantalum nitride-based resistive random access memory devices. *Applied Physics Letters*, 106(20):3–7, 2015.

[53] R. Mundle, Hampton Terry, M. Bahoura, and A. K. Pradhan. Ozone-assisted atomic layer deposited ZnO thin films for multifunctional device applications. *Journal of Physics D: Applied Physics*, 46(47), 2013.

[54] Kyung Min Kim, Doo Seok Jeong, and Cheol Seong Hwang. Nanofilamentary resistive switching in binary oxide system; A review on the present status and outlook. *Nanotechnology*, 22(25), 2011.

[55] H Schmalzried. Fa kröger: The chemistry of imperfect crystals, north-holland publishing company-amsterdam 1964. 1039 seiten. preis: hfl. 110,-. *Berichte der Bunsengesellschaft für physikalische Chemie*, 68(6):608–608, 1964.

[56] Doo Seok Jeong, Herbert Schroeder, and Rainer Waser. Mechanism for bipolar switching in a Pt/ TiO2 /Pt resistive switching cell. *Physical Review B - Condensed Matter and Materials Physics*, 79(19):1–10, 2009.

[57] Yuanmin Du, Amit Kumar, Hui Pan, Kaiyang Zeng, Shijie Wang, Ping Yang, and Andrew Thye Shen Wee. The resistive switching in TiO ₂ films studied by conductive atomic force microscopy and Kelvin probe force microscopy. *AIP Advances*, 3(8):082107, 2013.

Chapter 6

Conclusion and Future Plans

6.1 Conclusion

We have fabricated ceramics of $Ga_{2-x}(Fe_{1-y}Mn_y)_xO_3$, $0 \leq y \leq 0.02$ and $1 \leq x \leq 1.4$ by solid-state reaction route. The phase and structure was confirmed by X-ray Differaction, Reitveld and Raman spectroscopy. XRD and Raman result preliminarily show that doping of Fe and Mn in the above range does not change the structural phase. Single phase of polycrystalline samples, stabilizing in orthorhombic (C_{2v}^9) was achieved. Temperature-dependent magnetization study reveals that the transition temperature raises to above room temperature for higher Fe concentration. Among all these samples, GFMO3 is observed to possess the highest magnetization value at all temperature range with a transition temperature at 345 K. The magnetic control of electric characters, i.e. capacitance, tangent loss, impedance, and phase confirms the existence of magnetoelectric coupling in the sample. Doping of

manganese showed a greater influence to reduce the leakage current in GFOn compounds. The coupled phonon and magnetic ordering in $GaFeO_3$ (GFO1) were studied using magnetization and Raman spectroscopic investigations. Temperature dependent Raman spectroscopic studies in the temperature range of 82 - 580 K indicates the absence of any structural phase transition. Several modes located at 153, 176, 240, 700, and 756 cm^{-1} are found to have magnetoelastic coupling contributions below the T_C. The spin-phonon coupling strength is found to be larger for internal mode located at 700 and 756 cm^{-1} i.e. $\lambda \sim$ 2.14 and 2.92, respectively. Translational modes at 153 and 175 cm-1 and the librational rigid mode at 240 cm^{-1} are found to have nearly same coupling strength with $\lambda \sim 0.88$.

Highly oriented $Ga_{2-x}(Fe_{1-y}Mn_y)_xO_3$, $0 \leq y \leq 0.02$ and $1 \leq x \leq 1.4$ were depositied on SRO buffered STO (111) substrate. A systematic study on the fabrication, temperature-dependent magnetic, and electric behavior of the films were studied. Temperature-dependent magnetization studies at ZFC and FC condition shows large bifurcation with irreversible nature. Significant contrast within the upward and downward polarization in the PFM images of phase and amplitude confirms the piezoelectric nature of the compound. Study on temperature-dependent permittivity for GFO1 at various frequency satisfy the Vogel-

Fulcher curve fit following modified Curie-Weiss law. The value of is obtained as 1.95, showing the relaxor nature of the film. Photodetector behavior in GFO compound is revealed for the first time. Under the solar illumination, the photocurrent of the device is determined to be 1.955x10^{-3}A, while under the dark, current was 1.023x10^{-3}A at 5V. The value obtained is quiet low, however this is the pioneer in the field of GFO. Both direct gap (3.0 - 3.2 eV) and indirect band gaps (2.1 - 2.4 eV) were obtained on the GFO thin films deposited on fused silica.

This investigation suggests that by tuning Fe contents and Mn-doping in GFO, RT multiferroicity can be revealed with larger magnetization value, which make these materials promising for device applications.

In case of RRAM, we fabricated a graphene integrated see-through ITO/Al_2 O_3/G TRRAM device using a hybrid process and investigated its anticlockwise bipolar resistive switching characteristics. We found that the ON/OFF resistance ratio in the ITO/Al_2O_3/G device was slightly reduced compared to that in the ITO/Al_2O_3/Pt device, but the SET/RESET voltages significantly decreased, and the RESET current was noticeably reduced which are important features for memory operations. The observed resistive switching mechanism is understood to be due to the formation and rupture of conductive filaments formed

out of oxygen vacancies. Excellent endurance and retention characteristics and good contrast in the ON/OFF resistance ratio make the fabricated transparent device a potential candidate for TRRAM.

6.2 Future Plan

I envision my future research investigating on 2D magnetism. I want to investigate this field because of the novel physics within and promising applications for nanoelectronics. My focus will be to design 2D multiferroics with intrinsic magnetoelectric coupling and help to control magnetism by electric field. Currently, graphene magnet is rising topic in the field of 2D magnetism. Some transition-metal dichalcogenides (TMDs) such as MnX (X = S, Se), CrS_2, $Cr_{1/3}RaS_2$ and transition metal trichalcogenides with chemical formula ABX_3 like $CrXTe_3$, (X= Si, Ge, Sn) nanosheets have also shown ferromagnetic (FM) properties. Another representative branch of 2D FM material is transition-metal halides (THMs). This class of magnetic materials will open a new route to understanding the physics of new magnetic states and superconductivity. There has been the number of studies reporting the observation of ferromagnetism, however no consensus has been reached on the source of the detected signals. The method of electronic engineering is always theoretically proposed. The anticipated FM phases has not yet

been observed experimentally.

I am interested in two-dimensional (2D) layered materials, because of its clean surfaces and large dielectric constants, that can provide a novel avenue for realizing nanosize ferroics. The complex coupling can give rise to multiple functionalities; the cross control between the order parameters provides enormous and promising opportunities for electronics devices like energy harvesting, memories, sensors, and actuators.